Doctoral Thesis

NANOCHANNEL-ASSISTED ACTIVE CONTROL OF MASS TRANSPORT IN POLYDIMETHYLSILOXANE-BASED MICRO-/NANOFLUIDIC SYSTEMS

Dogyeong Ha

Department of Mechanical Engineering

Graduate School of UNIST

2020

NANOCHANNEL-ASSISTED ACTIVE CONTROL OF MASS TRANSPORT IN POLYDIMETHYLSILOXANE-BASED MICRO-/NANOFLUIDIC SYSTEMS

Dogyeong Ha

Department of Mechanical Engineering

Graduate School of UNIST

ULSAN NATIONAL INSTITUTE OF
SCIENCE AND TECHNOLOGY

NANOCHANNEL-ASSISTED ACTIVE CONTROL OF MASS TRANSPORT IN POLYDIMETHYLSILOXANE-BASED MICRO-/NANOFLUIDIC SYSTEMS

A dissertation
submitted to the Graduate School of UNIST
in partial fulfillment of the
requirements for the degree of
Doctor of Philosophy

Dogyeong Ha

11. 4. 2019
Approved by

Advisor
Taesung Kim

ULSAN NATIONAL INSTITUTE OF
SCIENCE AND TECHNOLOGY

NANOCHANNEL-ASSISTED ACTIVE CONTROL OF MASS TRANSPORT IN POLYDIMETHYLSILOXANE-BASED MICRO-/NANOFLUIDIC SYSTEMS

Dogyeong Ha

This certifies that the thesis/dissertation of Dogyeong Ha is approved.

11. 4. 2019

signature

Advisor: Taesung Kim

signature

Heungjoo Shin

signature

Hoon Eui Jeong

signature

Jungyul Park

signature

Jungchul Lee

Abstract

Nanofluidic devices have been extensively studied due to a fascinating nature of their small size which facilitates biosensing, bio-chemical separations, seawater desalination, nanofluidic transistors, protein, and preconcentration for a Lab-on-a-Chip (LOC). Such applications could be achieved by a control of electrokinetic transport in a nanochannel produced by sophisticated nanofabrication technique. However, it has been a challenge from a fabrication to the control of electrokinetic phenomena in nanochannel because of the cost, time, incompatibility, and addressability issues. Therefore, an innovative method is required to achieve simple fabrication and versatile operations of micro/nanofluidic device with limited resources. This dissertation proposes a new method for nanochannel-assisted active manipulation of mass transport by switching physicochemical environment. In the early chapters of this dissertation, unconventional fabrication methods for hybrid-scale micro-/nanofluidic devices is described by using both crack-photolithography and polydimethylsiloxane (PDMS) based soft lithography. The late chapters introduce the mechanism of the mass transport in micro/nanofluidic device using solutes gradient and humidity for manipulation of colloidal motion and molecule valves, respectively. These studies can be introduced as follows.

First, crack-photolithography is employed to facilitate large-scale reproducible channel fabrication through a single molding process and thus enable the fabrication of hybrid-scale micro-/nanofluidic devices at a wafer level with advantages seen in the throughput, cost-effectiveness, reliability, and reproducibility. In addition, modified soft lithography process is developed to fabricate stable nanochannel which is free from the collapse and the crumbling.

Second, crack-assisted nanochannel is introduced to manipulate physicochemical environment of neighboring microchamber. Diffusion-controlled ion transport produces solutes gradient inducing spontaneous electric field which affects the motion of colloidal particles. Since the single nanochannel allows the production of concentration gradient in a long-term and stable manner, least source is required to maintain the spontaneous electric field without any external power source, which is appropriate for a portable and self-containable LOC. As a practical application, integrated micro/nanofluidic device facilitates concentration, on-demand extraction, and separation of the colloidal particles.

Third, gas permeable PDMS nanochannel with high hydraulic resistance is employed to develop humidity-based gating nanochannel. The rate of mass transport can be manipulated by humidity due to the evaporation of water and the adsorption of solutes to the wall of channel. To demonstrate functionality of humidity for liquid gating or capacitor of molecules, the effect of humidity on mass transport was investigated. This new concept of manipulation of nanofluidic transport made it possible to successfully perform individual mass transport control in a nanochannel array, which is difficult with conventional technique using electricity. It further facilitated on-demand addressable bio/chemical assay using humidity-based molecule valves and pumps.

The role of nanochannel as a passage for mass transfer is essential to allow stable and precise control of transport of ions and molecules in the microchannel. It provides wide range of applications using a diffusion-based control of microfluidic environment to induce not only solute gradient for production of electric field but also liquid gating for a valve at molecular level. Thus, achievements of this dissertation contribute to raise the insight about nanochannel-assisted system for simple and precise control of mass transport in hybrid-scale micro-/nanofluidic devices, which is facilitated by the help of the cracking-assisted micro-/nanofabrication technologies.

Table of Contents

List of Figure

List of Tables

Nomenclature

AFM: atomic force microscopy

AHL: acryl-homoserine lactone

AR: aspect ratio

CCD: charge-coupled device

C. elegans: *Caenorhabditis elegans*

C-MEMS: carbon-microelectromechanical systems

CP: chemiphoresis

DNA: deoxyribonucleic acid

DO: diffusioosmosis

DP: diffusiophoresis

EBL: e-beam lithography

E. coli: *Escherichia coli*

EDL: electrical double layer

EOF: electroosmotic flow

EP: electrophoresis

FI: fluorescence intensities

FIB: focused ion beam

FITC: fluorescein isothiocyanate

GFP: green fluorescent protein

h-PDMS: hard polydimethylsiloxane

ICP: ion concentration polarization

LOC: lab-on-a-chip

LB: luria broth

μTAS: micro-total-analysis

MNDP: micro/nanofluidic diffusiophoresis platform

M9: minimal broth

NEP: nanoelectroporation

NIL: nanoimprint lithography

NSE: *Navier-Stokes* equation

UV: ultraviolet

UVO: ultraviolet ozone

PAG: photo-acid generators
PBS: phosphate buffered saline
PEB: post-exposure baking
PET: polyethylene terephthalate
PDF: pressure-driven flow
PDMS: polydimethylsiloxane
PMMA: polymethylmethacrylate
PUA: polyurethane acrylate
RH: relative humidity
SEM: scanning electron microscopy
x-PDMS: extra hard polydimethylsiloxane
$\mathbf{u}$: fluid velocity vector
$\mathbf{g}$: external source
$\mathbf{J}$: diffusive flux of species
D: diffusion coefficient of species
C: concentration of species
v: kinematic viscosity
w: specific thermodynamic work
Re: *Reynolds* number
Pe: *Péclet* number
l_c: characteristic length
ρ: density
η: dynamic viscosity
γ: surface tension
θ: contact angle
ρ_e: charge density
$\mathbf{E}_x$: electric field
ψ: wall potential
ε: permittivity of the medium
ζ_p: particle zeta potential
ζ_w: wall zeta potential
β: diffusivity difference factor

k_B: Boltzmann constant

a: radius of species

z: valence of ionic species

e: elementary charge

ϕ: electric potential

κ^{-1}: electrical double layer thickness

Γ_w: diffusioosmotic mobility

Γ_p: diffusiophoretic mobility

Chapter 1. Introduction

1.1 Development of micro/nanofluidic devices for lab-on-a-chip

Biochemical research has been widely done in large-scale environments using flasks or test tubes accompanying intensive labor, time, and reagent-consuming. In order to improve throughput and reduce sample volumes, 96-well microtiter plates have been introduced and contributed to increase the throughput [1]. However, the sample volume in each well was still as much as hundreds of microliters so that a demand for miniaturized system has been increased continuously. To satisfy this demand, microfluidic systems have provided advantageous environments for miniaturized biochemical analysis such as small sample requirement, short reaction time, and low cost [2]. Especially, lab-on-a-chip (LOC), a miniaturized analysis system in the form a single chip has been rigorously developed because of its potential in DNA sequencing [3], biochemical detection [4], or cell to cell communication [5]. Although this microfluidic system have satisfied the demand for miniaturized tool, they had a difficulty to conduct more accurate biochemical assay at a single molecule level because of limitation of resolution. Therefore, nanofluidics have been emerged as a breakthrough because of their superior characteristics such as small scale environment that is comparable to the size of individual molecule [6]. Based on these characteristics, nanofluidics have been widely studied for electrical double layer (EDL) overlap [7], nanoelectroporation (NEP) [8], ion concentration polarization (ICP) [9], and ion rectification [10]. However, existing micro/nanofluidc devices are not still easily accessible to many people due to the complexity of the fabrication method and the limitations of the electrokinetic-dependent driving force, which is represented by an external power source. More recently, an array of nanofluidic networks that are integrated with microfluidic systems are demonstrated to facilitate deliberate mass transfer into the microfluidic chip, *e.g.* the treatment of microorganism with quantitative stimuli at molecular level [11]. This is the hybrid-scale LOC devices, which are integrated micro/nanofluidic array. Increasing simply the number of nanochannel array, hybrid-scale LOC devices facilitates not only versatile nanofluidic applications in a high-throughput manner, but also control of microfluidic channel environment based on diffusive transport.

The following sections introduce the conventional and uncvonventional fabrication methods to produce micro/nanofluidic devices (Chapter. 1.2) and theory governing mass transport (Chapter. 1.3) and application (Chapter. 1.4) of micro/nanofluidic devices. The final section introduces motivation and overview of each chapters in this dissertation (Chapter. 1.5).

1.2 Conventional and unconventional fabrication technologies for micro/nanofluidic devices

Overview. As shown in Fig. 1-1, a development of fabrication technique has led to the evolution of state-of-an-art LOC devices [12]. Various conventional micro/nanofabrication technologies such as standard photolithography, direct writing tool (e-beam and focused-ion-beam milling), interferometric lithography, and nanoimprint lithography (NIL) have been well developed and widely used for fabricating hybrid-scale LOC devices. However, these conventional fabrication technologies appear to be sometimes inefficient for hybrid-scale LOC fabrication in terms of throughput because there exists an engineering trade-off between high-throughput and high-resolution [13, 14]. Recently, an alternative way to compensate for or substitute for the conventional technologies have emerged. For example, deformation of elastomeric materials are employed to develop nanopatterns on previously produced microchannels. Also, novel unconventional techniques that enable monolithic mold fabrication, and thus complex integrated micro-/nanofluidic networks in a single soft-lithography process have been developed. In this section, current hybrid-scale fabrication technologies are reviewed in terms of pros and cons of each method.

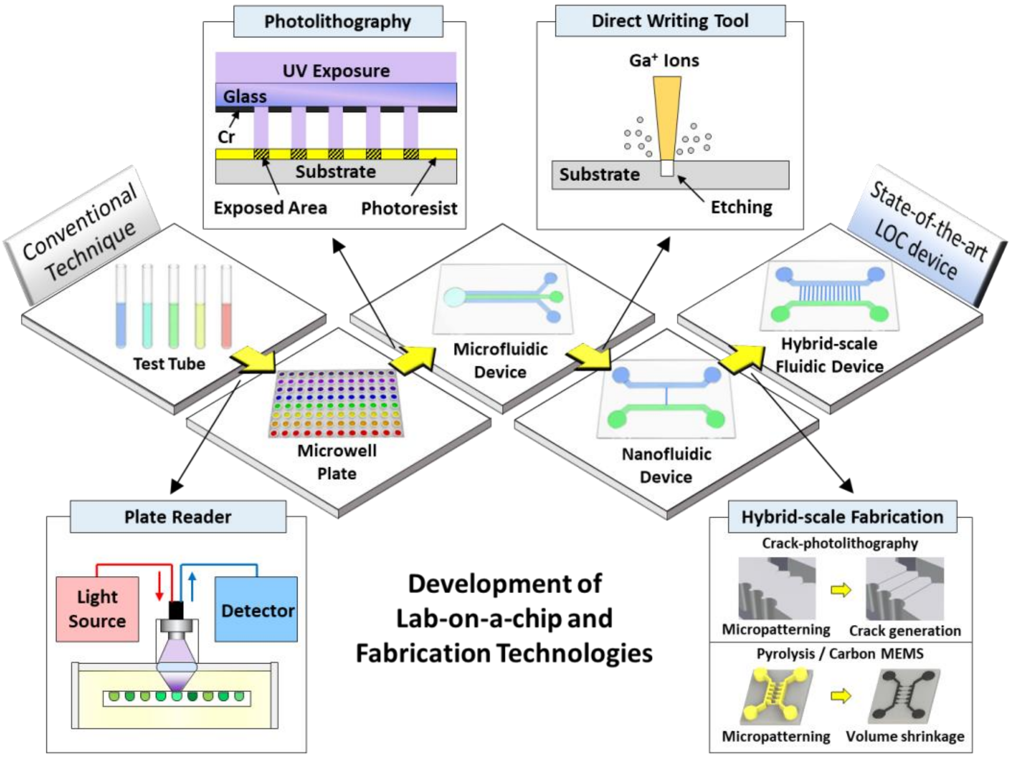

Figure 1-1. Schematic illustration showing the necessity of hybrid-scale LOC devices. Conventional and/or unconventional micro-/nanofabrication techniques are widely employed to not only increase throughput but also enhance resolution of the state-of-an-art hybrid-scale LOC devices [12].

Top-down photolithography-based micromachining. Photolithography is the most common patterning method using UV-exposure on photosensitive polymer or photoresist. With selective UV-exposure through a photomask containing transparent areas with a design that users intend to transfer, the solubility of photoresist layer coated on the substrate is changed locally. Thus, after selective photoresist etching process called development, patterns of the photomask are transferred to the photoresist at a wafer level. As shown in Fig 1-2, these patterned photoresist structures work as etch mask for subsequent substrate etching process and the etched patterns work as micro/nanochannels. By controlling etching rate in a very careful manner, the depth of etched substrate can be controlled at sub-micrometer scale. Depending on the etching conditions, various substrate materials such as silicon [15], glass [16], polycarbonate [17], and PMMA [18] can be used as channel materials. After removing residual photoresist etch masks, micro/nano fluidic channel networks are completed by bonding a planar plate to the etched substrate.

Despite the advantages such as simple and batch procedures, the fabrication of nanochannels, either height or width of which is less than 100 nm, is limited because of the limited lateral resolution of conventional photolithography. And thus, the nanofluidic devices fabricated using photolithography-based etching process are in the form of a shallow nanoslit; only height of which can reach nanoscales.

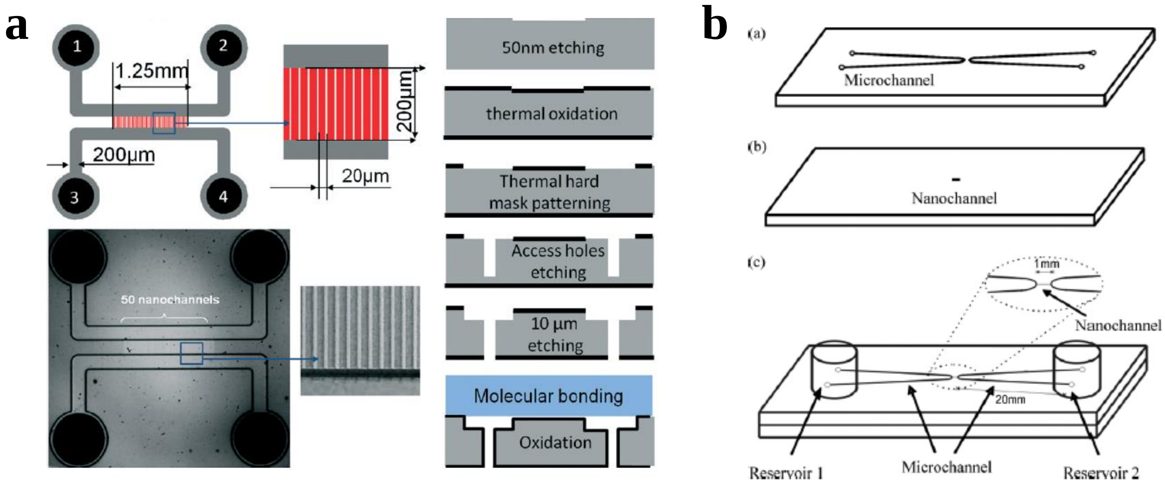

Figure 1-2. Nanochannel fabrication *via* top-down photolithography-based micromachining. (a) Scheme and microscopic images show fabrication process of 1D silicon nanochannel. (b) Scheme shows concept of fabrication of 1D glass nanochannel. Figure (a) and (b) were adapted from Aizel *et al*. [15], and He *et al*. [16], respectively.

Direct writing tools. The aforementioned limitation in spatial resolution of photolithography can be overcome by using nanofabrication technologies, especially direct writing methods including e-beam lithography (EBL) [19-21] and focused ion beam (FIB) milling as shown in Fig 1-3 [22, 23]. By scanning focused nanoscale electron/ion beam laterally, user-defined 2D designs can be drawn on the substrate. Due to the small beam size, the minimum feature size can be reduced down to 20~50 nm.

EBL uses highly concentrated electron beam (e-beam) as a writing tool like a pen. Therefore, the scanned area by the beam is quite localized due to the small beam size. E-beam resists are categorized into positive and negative resist depending on solubility change after e-beam exposure. The positive resist becomes soluble in the developer; this type of resist is appropriate for etch mask in forming engraved trenches or channels. In contrast, the negative resist withstands development and upholds the e-beam-exposed structures; thus this type of resist is commonly used for patterning convex narrow and long structures that are used as nanochannel molds in subsequent soft-lithography [20] or nanoimprint processes [21].

FIB also employs highly intensive focused beam enabling direct writing. In contrary to EBL, FIB can remove surface material because of high bombardment energy and thus ion-beam scanned regions are directly engraved into micro/nanochannels [22] without additional etching processes. Generally, FIB is not efficient method for the channel patterning on the substrate in terms of cost-effectiveness because of its serial and time-consuming characteristics. This limitation in mass production can be overcome by replicating polymer molds or replicas using the FIB-milled concave channel master and the replicated convex molds are used as new molds or stamps in subsequent soft-lithography or nanoimprint processes, respectively [23]. By replicating multiple replicas from a single FIB-milled master, throughput can be even more enhanced.

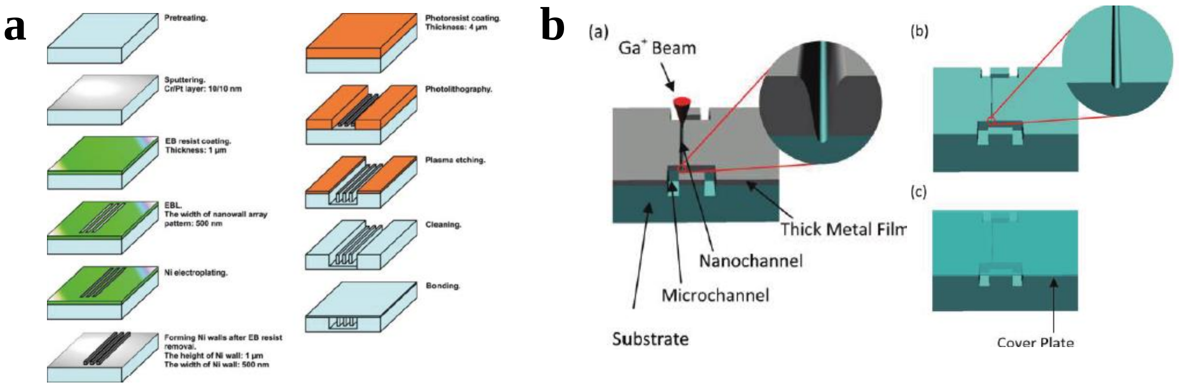

Figure 1-3. Nanochannel fabrication *via* electron beam lithography (EBL) and focused ion beam (FIB). (a) Schematic images show EBL-based nanochannel fabrication method. (b) Schematic images show FIB-based nanochannel fabrication method using the thick metal film. Figure (a) and (b) were adapted from Aizel *et al*. [15], and He *et al*. [16], respectively.

The high spatial resolution of the direct writing nanofabrication technologies enables the fabrication of nanochannels with tens of nanometer scale in either width or height. Nevertheless, these methods are mainly used for nanochannels or nano-sized mold fabrication at localized positions with quite small areas on the substrate because of their time-consuming serial characteristics and expensive equipment. Therefore, for the fabrication of hybrid-scale LOC devices, additional microchannel fabrication techniques have to be added prior or subsequent to the direct writing processes. This multi-step hybrid fabrication approach increases process complexity and requires delicate alignment, which may deteriorate throughput.

Nanoimprinting. Nanoimprint is a replicating method that can fabricate micro-/nanofluidic devices in a high-throughput manner. As shown in Fig 1-4, nanoimprint is classified into two types depending on polymer types; thermal and UV nanoimprint methods. In thermal nanoimprint [24], solid state thermoplastic polymer becomes quasi-liquid state *via* heating and deformed in the shape of a mold under compression, and finally re-solidified *via* cooling. In UV nanoimprint [25], liquid state UV-curable polymer is crosslinked and solidified by UV exposure through a transparent mold. For both the nanoimprint types, a mold with pre-engraved patterns is pressed down on the quasi-liquid or the liquid state polymer layer and then, the concave parts or cavities of the mold are filled with the polymer and solidified completing replication. For the precise mold pattern transfer, polymers have to fully fill the cavities and be clearly detached from the mold without pattern damages, so that anti-adhesion layers are coated on the mold surface before imprinting. The high-throughput production of hybrid-scale LOC devices can be fulfilled as long as the hybrid-scale mold is fabricated in a convex form. Because of the direct pattern transfer capability of nanoimprint, effective hybrid-scale LOC devices can be fabricated at a wafer level and the pattern transfer can be repeated using a single mold; these ensure high throughput. Besides, various types of polymers and nanoimprint methods can be used depending on the working conditions of the fluidic devices.

However, the fabrication of nanoscale convex parts of such mold is limited because of complex, expensive, and time-consuming processes. Furthermore, it has limitations in mold damages, pattern distortion and difficult alignment process. Also, in case of thermal nanoimprint, mismatch of thermal expansion of mold and polymer at their interfaces can interrupt clear detaching and cause distortion of transferred patterns.

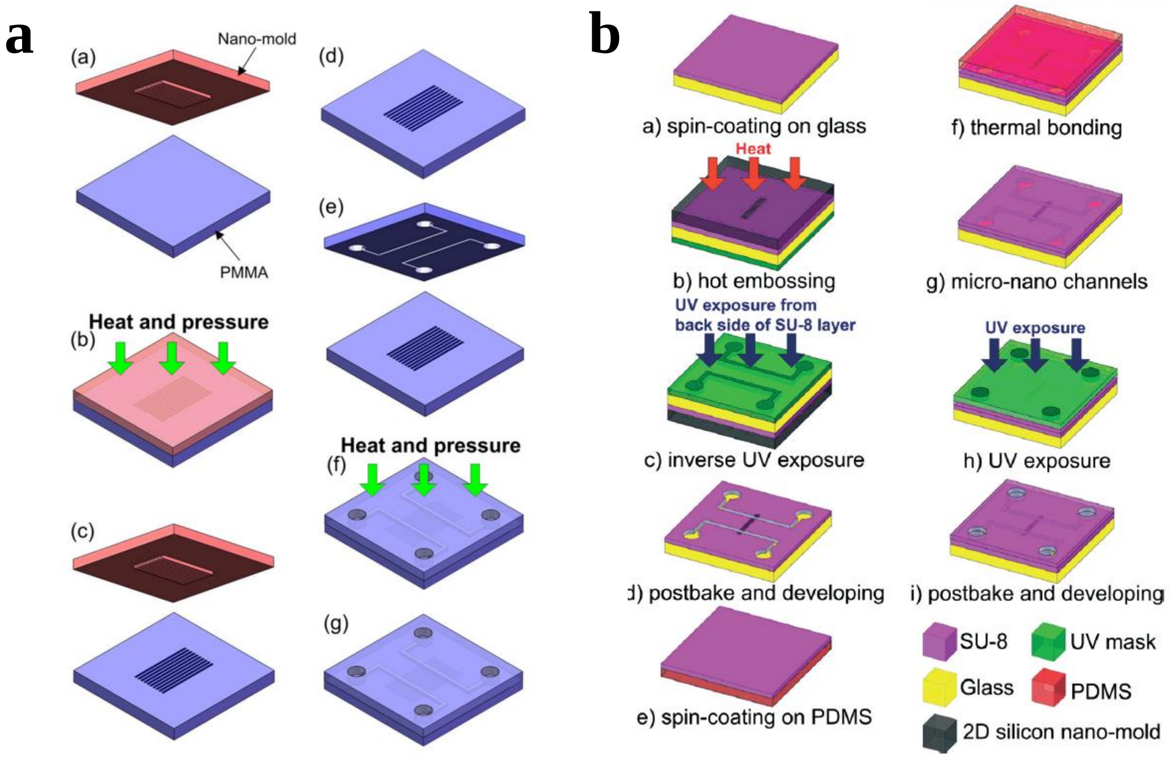

Figure 1-4. Nanochannel fabrication *via* Nanoimprint. (a) Schematic images show fabrication process of thermal nanoimprint method. (b) Schematic images show fabrication process of UV-assisted nanoimprint. Figure (a) and (b) were adapted from Yin *et al*. [24, 25].

Interference lithography. Using interference of light without a photomask, interference lithography can pattern photoresist into periodical nanopatterns such as lines and circles of which sizes are smaller than the wavelength of incident light; thus diffraction limit of conventional photolithography and low throughput of direct writing tools can be overcome [26, 27]. As shown in Fig. 1-5, a single coherent laser source is divided into two laser beams by a beam splitter in the interference lithography. One of the split beams irradiates the photoresist directly, and the other beam irradiates the same position of direct irradiation through a feedback control system to relieve a phase error. Since the distance between the substrate and beam splitter is long, phase error due to vibrations, defects of optical elements, air current fluctuation affects the fringe pattern. The feedback control system to compensate for this phase error consists of photodiodes to detect the movement of fringe patterns and piezoelectric actuators attached to a mirror to control the direction of the reflected beam. When the photodiodes detect the phase error signal, this signal is transferred to piezoelectric actuators that leads compensation for the position of the mirror. Thus the feedback control system facilitates that two incident beams are recombined symmetrically resulting in interference of light on the substrate. By increasing the number of incident beams and configuring the beam combinations, the pattern shapes in interference lithography can be diversified from simple line patterns to various kinds of circular pattern arrays such as hexagonals and squares using 3-beam and 4-beam interferences, respectively. In addition, the period of nanopatterns is controllable depending on the incident angle and wavelength of the beam.

In the point of fabricating nanofluidic systems, interference lithography is able to fabricate nanopatterns with high throughput and high resolution up to tens of nanometer scale. As a maskless lithography with simple optical elements, interference lithography is cost-effective compared to conventional photolithography [27]. However, in spite of the referred advantages, this technique can create only limited kinds of pattern shapes such as periodical 1D lines or 2D circles; thus its applications are limited to micro-/nanofluidic systems accommodating simple periodical channel networks. In addition, additional microchannel fabrication steps should be implemented to make hybrid-scale LOC devices.

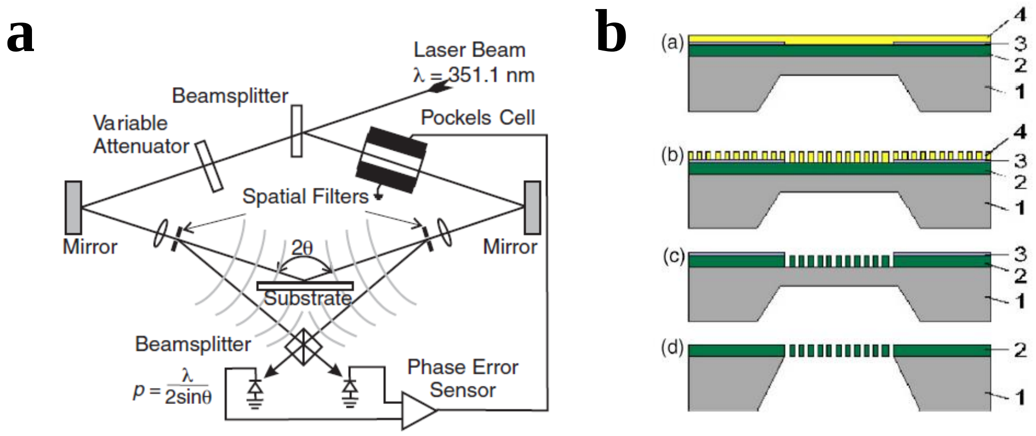

Figure 1-5. Nanochannel fabrication *via* interference lithography. (a) Schematic image shows fabrication set-up of interference lithography. (b) Schematic images show mask-less fabrication process of interference lithography. Figure (a) and (b) were adapted from Xia *et al.* [26], and Van *et al.* [27], respectively.

Elastomeric material deformation-based micro-/nanofabrication. Many researchers have developed unconventional fabrication techniques by utilizing the mechanical deformation of elastomeric materials. As shown in Fig 1-6, the deformation of elastomeric materials can be categorized into wrinkling [28-30], cracking [31-33], and structure/channel collapsing [34, 35], which have been widely used to fabricate hybrid-scale structures/channels in time-efficient and cost-effective manners. For a certain case, elastomeric microfluidic devices completely fabricated are subject to unwanted deformation, which is typically considered to avoid. However, deformation-based fabrication methods recently draw more attention because they enable nanoscale patterning through an elaborate control of the applied stresses to material. Specifically, the methods are allowed to additionally produce nanopatterns to the previously fabricated micropatterns or microchannels, thereby forming a micro-/nanofluidic channel network in series. In addition, since the methods can be conducted outside cleanroom facility, it is very cost-effective and user-convenient to fabricate hybrid-scale LOC devices.

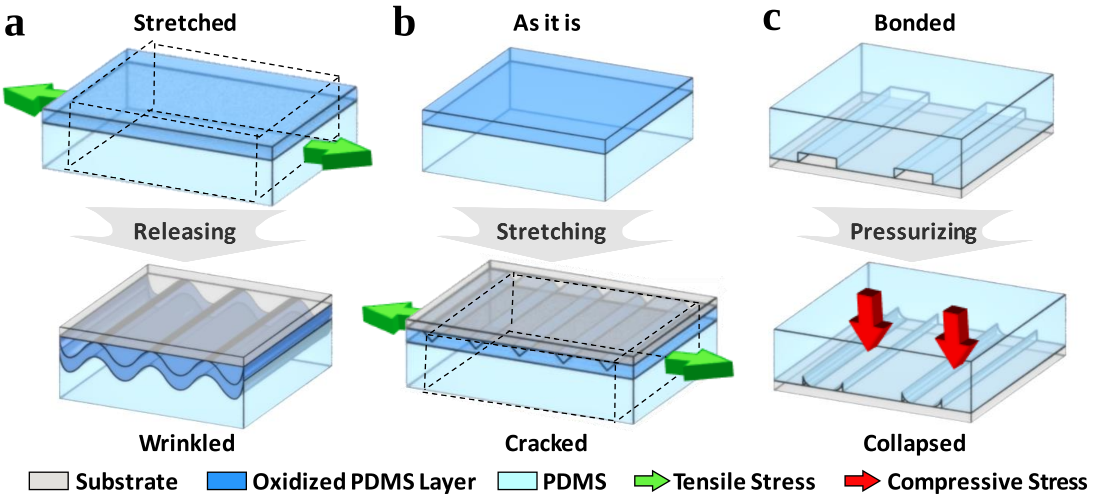

Figure 1-6. Schematic figures of principles of elastomeric material deformation-based nanofabrication methods. (a) Wrinkle-based nanochannels were fabricated and integrated with microchannels to form a hybrid-scale LOC device. When elongated device was released to original shape, oxidized PDMS surface was wrinkled due to the mismatch of elastic strain between surface and substrate. (b) Nanochannels were fabricated at the interface of two layers via cracking, which was typically caused by the combination of different material properties and applied tensile stresses. (c) Forced collapse of PDMS microchannels resulted in triangular shape nanochannels. Figure 1-6 was adapted from Ha *et al.* [12].

Wrinkling was forced to occur by applying ultraviolet ozone (UVO) or oxygen plasma to various materials [36]. The UVO treatment made the top surface of a pre-elongated PDMS slab hardened, converting into a silica-like oxide layer. When the strain was released, the supporting layer could fully recover its original strain-free condition whereas the top PDMS layer could not. For this reason, the mismatch of elastic strain between the stiff top surface and the soft supporting layer caused wrinkles, releasing the applied stresses *via* material deformation. A PDMS slab with wrinkle patterns can be bonded to another oxidized PDMS slab with microchannels, resulting in an integrated nanochannel array [29]. As an alternative way, wrinkling can induce foldings by continuously applying excessive strain to the film. The folding-based tunable nanochannels is demonstrated for trapping and releasing of Au nanoparticles [30]. Like winkling, folding has also been proven to be useful and practical for fabricating hybrid-scale LOC devices in an unconventional and unprecedented manner. Wrinkling- and folding-based nanofabrication techniques allow for the production of tunable nanochannels in either open- or closed-channel formats. Furthermore, these fabrication techniques provide several advantages such as economic, facility-free, and easy-to-learn processing. However, it is also noted that the fabrication process is sequential, and the repeatability and reproducibility are relatively low compared to those of conventional techniques.

Cracking is the fracturing of a material and is a phenomenon that is often observed, which is caused by tensile stesss. The cracking mechanism is similar to that of wrinkling but shows one distinct difference in that cracking is generated by applying a tensile stress to the material while winkling is caused by the elastic strain mismatch between the top layer and the underlying bottom layer. In principle, cracking occurs when the applied tensile stress is greater than the material resistance against fracture; this material property is called fracture toughness [31]. This cracking mechanism has been applied to elastomeric materials to generate nanoscale patterns by applying a tensile stress to an oxygen-plasma-treated PDMS slab with a microfluidic channel network [32]. Because cracks are generated in the direction orthogonal to the applied tensile stress, a crack-based nanochannel array was formed and integrated into the microchannels, resulting in a hybrid-scale LOC device. Compared to the wrinkle-based nanofabrication technique, the crack-based nanofabrication technique easily produced nanopatterns and controlled the number of cracks using notch patterns and a mechanical stretcher to produce and concentrate the tensile stress. However, crack-based nanofabrication methods still rely on serial fabrication processes (i.e., microfabrication and then nanofabrication or vice versa). In addition, the strengths of the tensile stresses are not uniform, but depend on the local positions of the notched microstructures. This results in non-uniform dimensions for the nanocracks over a large area.

Elastomeric materials have a relatively low elastic modulus, which makes the geometry of a microchannel made of an elastomeric material susceptible to deformation and deflection [37]. In particular, where the cross-section of a microchannel has a low aspect ratio, the ceiling of the microchannel sometimes sags and then sticks to the bottom substrate. This is called “roof-collapsing.” Researchers need to take this phenomena into consideration when they design and fabricate microchannels using soft-lithography. However, this roof-collapsing was conversely used as a nanofabrication method because it was possible to control and estimate the geometry and size of the resulting channels after roof-collapsing. Typically, the top-middle part of a microchannel bonds to the bottom substrate with conformal contact, leaving the two corners open [34]. For example, in case of a microchannel, it was several sub-microns in depth and tens of microns in width. Two triangular nanochannels with depths of several tens of nanometers and sub-micron widths were also created at the side walls. Similarly, a bunch of collapse-based nanochannel array was introduced for a role of nanoporous polymeric membrane [35]. Roof-collapsing-based nanofabrication is the simplest method among the nanofabrication methods, relying on the deformation of the elastomeric materials. Because nanochannels are always produced along the corners of a microchannel, hybrid-scale LOC devices can be fabricated without an additional alignment process. However, the geometry and dimensions of the nanochannels are relatively uncontrollable compared to wrinkling- or cracking-based methods because the nanochannels are produced by a manual and irreversible bonding process. Thus, the same weakness in reproducibility exists as with other unconventional nanofabrication methods.

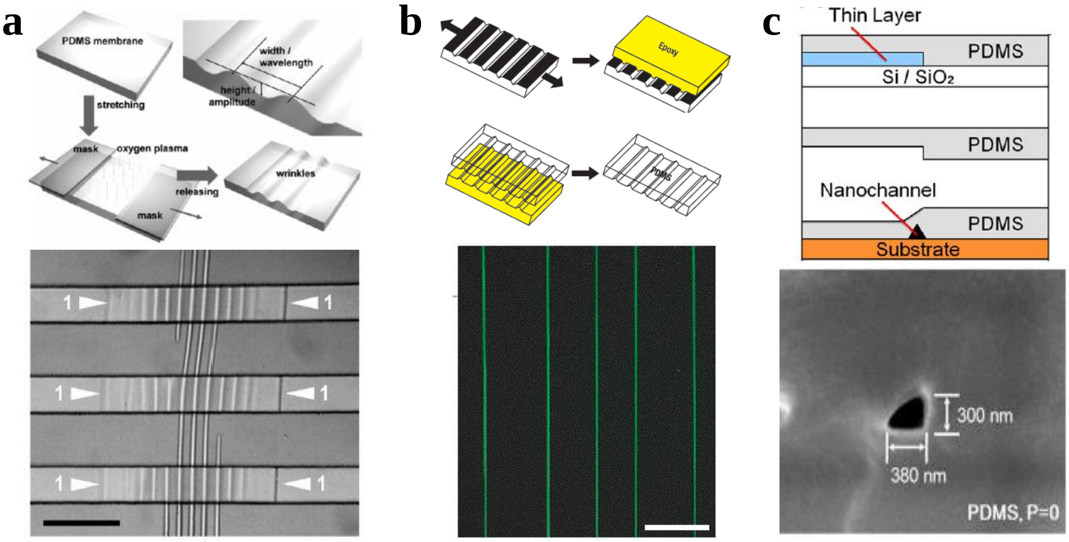

Figure 1-7. Elastomeric material deformation-based nanofabrication methods. (a) Integrated micro/nanofluidic device is produced by wrinkle-based nanofabrication method. (b) Oxidized PDMS surface is employed to produce epoxy mold for fabrication of crack-induced nanochannel array. (c) Low aspect ratio of PDMS microchannels were simply collapsed by normally applied pressure, which produces triangular nanochannel. Figure (a) was adapted from Chung *et al*. [29]. Figure (b) was adapted from Huh *et al*. [32]. Figure (c) was adapted from Park *et al*. [34].

Hybrid-scale mold fabrication and soft-lithography. As described previously, hybrid-scale fluidic channel networks can be simply fabricated by the deformation of the elastomeric materials; this facilitates the reduction of cost and production time, which is necessary and very useful in the repetitive experiments using disposable LOC devices. However, the relatively low reproducibility of elastomeric materials deformation-based techniques still needs to be overcome to extend their applications. In addition, it is difficult to apply these techniques to a large scale device because the stress to induce deformation is not consistently applied to the large area of a substrate. Soft-lithography and nanoimprint can overcome the limitation of elastomeric materials deformation-based techniques. These techniques can pattern hybrid-scale LOC devices with high-resolution and high-reproducibility at a wafer level as long as a mold incorporates nano- and micro-sized patterns altogether. Therefore, the facile and reproducible fabrication techniques for hybrid-scale master molds need to be developed for cost-effective fabrication of hybrid-scale LOC devices. In particular, the hybrid-scale mold in a monolithic form is beneficial for robust pattern transfer. More recently, various unconventional mold fabrication techniques using cracking [38], and pyrolysis [39] have been developed for the simple fabrication of master molds with hybrid-scale patterns or fluidic channels. These techniques can fabricate the master mold with a number of uniform nanopatterns that are connected with micropatterns.

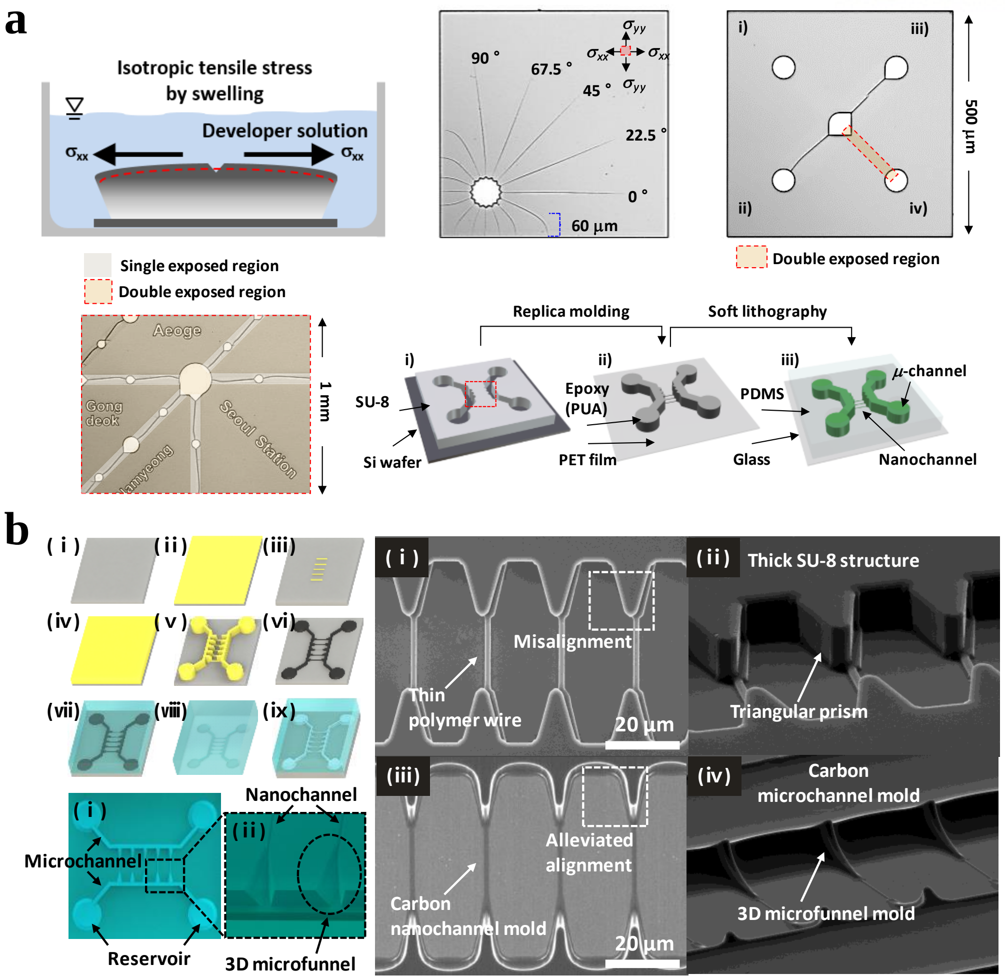

Figure 1-8. Hybrid-scale mold fabrication using crack-photolithography and pyrolysis. (a) Crack-photolithography-based fabrication method for monolithic mold. The swelling of the patterned photoresist caused isotropic tensile stress, enabling the production of cracks at the stress-concentrating structures during the development process. (b) Pyrolysis-based C-MEMS fabrication method for monolithic mold and. Thermal decomposition facilitates volume reduction of pre-patterned polymer structure which can be used for complex and high-aspect-ratio of mold. Figure (a) was adapted from Kim *et al.*,[38] Figure (b) was adapted from Lee *et al.*[39]

The crack-photolithography method uses cracking phenomena on the top surface of a photoresist (SU-8) during standard photolithography [38]. The technique is very simple and requires no additional nanofabrication equipment. During the mask design step, triangular microstructures are added to a typical microfluidic channel network wherever nanocracks are necessary. In the same manner, round microstructures are added wherever the nanocracks should stop. Subsequently, the mask design is transferred to a thin SU-8 film on a Si wafer, which in turn is developed using a developer solution to produce micropatterns. Crack patterns are simultaneously created during the development process because a tensile stress caused by the swelling of the viscoelastic, supporting bottom layer of the SU-8 pattern is applied to the thin, elastic top layer of the SU-8 pattern [40]. Using this mechanism, it was possible to produce crack-photolithography-based nanochannels in parallel with microchannel structures in a high-throughput manner over a large area. For example, 1000 pairs of microchambers were connected through the crack-photolithography-based nanochannels.

The pre-patterned polymer structures are then converted into glassy carbon structures with a large volume reduction via pyrolysis. The volume reduction in pyrolysis occurs in an isometric manner, which enables the simple fabrication of complex and high-aspect-ratio convex carbon micro-/nanostructures. In addition, the pyrolyzed carbon material itself is a good candidate for a mold material because of its superior properties, which include a low surface energy, chemical stability, high hardness, wear resistance, and gas impermeability. A pyrolyzed monolithic multi-scale convex carbon mold is introduced to fabricate a hybrid-scale LOC device [39]. As shown in Fig 1-8(b), they utilized the volume reduction process that occurs in the pyrolysis process to produce nanoscale convex carbon structures. A maximum volume reduction of 90% occurred during the pyrolysis. Thus, convex carbon molds with nanochannel structures (width ~ 720 nm, height ~ 32 nm) were fabricated at a wafer level by pyrolyzing microscale structures made of the SU-8 precursor (width ~ 1.1 μm, height ~ 210 nm). Notably, the structures were patterned using conventional photolithography and pyrolyzed without any complex and expensive nanofabrication process.

1.3 Theoretical background of mass transport in micro/nanofluidic devices

Convective transport. The simplest way to transport molecules in micro/nanofluidic device is to move the fluid itself in which the molecules is present. As shown in Fig 1-9, there are several methods to drive the fluid in the channel [41]. However, shear-driven flow is not usual approach for micro/nanofluidic devices so that pressure-driven flow (PDF), capillary flow, and electroosmotic flow (EOF) are introduced in this section. First of all, those flow mechanism can be derived from the momentum equation. Because most samples in micro/nanofluidic applications exist in water, incompressible *Navier-Stokes* equation (NSE) can be introduced to describe the hydrodynamic convection, which is shown as follows:

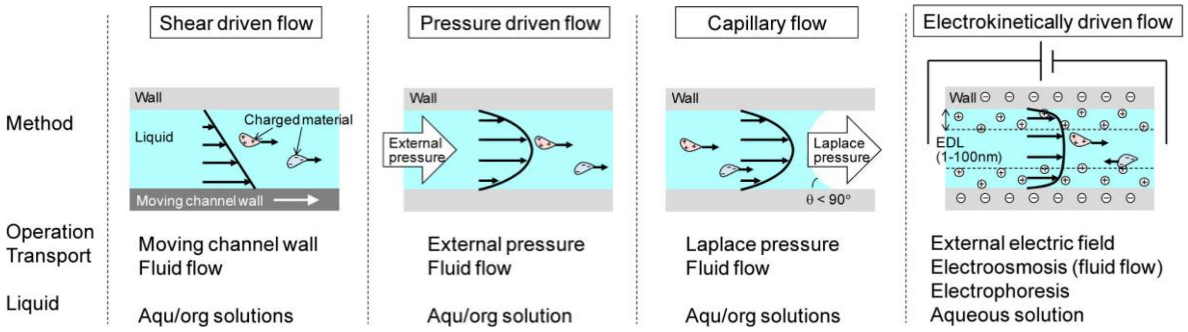

Figure 1-9. Summary of transport control of hydrodynamic convection. Figure was adapted from Mawatari *et al*.[41]

$$\frac{\partial \mathbf{u}}{\partial t}+(\mathbf{u}\cdot\nabla)\mathbf{u}-\nu\nabla^2\mathbf{u}=-\nabla w+\mathbf{g} \tag{1}$$

where **u** is a fluid velocity vector, ν is kinematic viscosity, w is the specific thermodynamic work representing internal source, **g** is external source such as external electric fields, respectively. Since the micro/nanofluidic device deal with *Stokes* flow due to the small characteristic length (l_c ~ 10^{-6} m) resulting in low *Reynolds* number (Re = $\mathbf{u}\ l_c\ \nu^{-1}$), inertial terms represented in second term in the NSE is negligible. If there is no external forces and the internal source is the thermodynamic pressure ($w = p\ \rho^{-1}$, ρ is the uniform density), the fully developed hydrodynamic convection in steady state can be expressed as follows:

$$\eta\nabla^2\mathbf{u}-\nabla p=0 \tag{2}$$

where η is the dynamic viscosity. Since the fluid velocity is determined by a pressure gradient, it is important to choose the optimized pressure source for flow control. Although commercial syringe pump or hydrostatic force are commonly used for microfluidic devices, these methods do not give enough pressure in the regime of nanofluidics due to the high hydraulic resistance.

As an alternative way, capillary flow can be used to drive the fluid in nanochannel. On the contrary to the PDF, capillary flow getting stronger as the characteristic length reduces, because this is surface tension-driven flow. In the channel, the surface tension of the interface between gas and liquid produces pressure difference, which is described by the *Laplace* pressure shown as follows:

$$\Delta p=\frac{4\gamma\cos\theta}{d} \tag{3}$$

where γ is the surface tension, θ is the contact angle, and d is the characteristic length of the channel, respectively. Although the capillary flow is the simplest way to transport fluid in the micro/nanofluidic devices, this is limited to one-time use for loading a fluid on wetting surface. Thus, this is not appropriate for dynamic transport control of fluid.

In order to achieve dynamic transport control of fluid in the channel, the EOF is commonly used under the external electric fields. The driving force is caused by the drag of ions adsorbed to the wall. The surface with a certain charge (e.g., negative charge density for PDMS or glass) draws the ions due to the electrostatic interaction, which produces electrical double layer (EDL) [42]. In the EDL, net charge of ions forms zeta potential. When the electric field is applied across the channel, the counter ions moves to the electrode inducing fluid flow called electroosmotic flow (EOF). Recall that NSE includes external sources such as the external electric field so that the EOF can be derived from the balance between viscous force and coulomb force shown as follows:

$$\eta\nabla^2\mathbf{u}=-\rho_e\mathbf{E}_x \tag{4}$$

$$\nabla^2 \psi = \frac{\rho_e}{\varepsilon} \tag{5}$$

where ρ_e is the electric charge density, $\mathbf{E}_x$ is the electric field, ψ is the potential of the wall, and ε is the permittivity of the medium, respectively. Since the difference in potential between bulk fluid and the no-slip plane is the zeta potential, the EOF is expressed by *Helmholtz-Smoluchowski* equation:

$$\mathbf{u} = \frac{\varepsilon \zeta}{\eta} \mathbf{E}_x \tag{6}$$

where ζ is the zeta potential of the wall. Since the external electric fields is simple to control the direction and velocity of fluid flow, most of researchers deal with electrokinetically driven flow for dynamic transport control of fluid in nanochannel. However, the integration of external electric instrument leads to increase in size and cost. In addition, electrochemical reaction at the electrode produces toxic ions that can give adverse effect to the biological samples such as protein and cells.

Diffusive transport. The diffusion is a random molecular motion to satisfy thermodynamically stable condition in the medium which is dynamic equilibrium. In general, diffusion is not preferred method for mass transport due to the relatively low velocity compared to that of the hydrodynamic convection. However, the diffusion is the only way to transport molecules in convective transport limited space. This is driven by kinetic energy of random motion by a gradient in chemical potential between high concentration species and low concentration species. The *Fick*'s law of diffusion describes the negative gradient of concentrations as shown follows:

$$\mathbf{J} = -D \nabla C \tag{7}$$

where, **J** is the diffusive flux of species, D is the diffusion coefficient of species, and C is concentration of species, respectively. According to the *Stokes-Einstein* relation in the limit of low *Reynolds* number, the diffusion coefficient of colloidal particles D_p is proportional to the squared velocity depending on the viscosity, temperature of the fluid and size of species as shown follows:

$$D_p = \frac{k_B T}{6\pi\eta a} \tag{8}$$

where, k_B is Boltzmann's constant, T is the absolute temperature, a is the radius of the species, respectively. Diffusive dominant environment can be predicted by the *Péclet* number ($\mathrm{Pe} = \mathbf{u}\, l_c\, D^{-1}$), which is defined as the ratio of the rate of fluid advection to that of diffusion. Since Pe is the decreased as the size of the species or fluid velocity reduce, diffusive transnport is important when the small species such as biomolecules and ions ($D \approx 10^{-11}$~10^{-9}) pass through the fluidic channel with high hydraulic resistance.

Conservation of a charged species. Since most of the materials in nature have a finite charge, the transport by electrostatic forces must be considered in addition to the aforementioned transport mechanism. The *Nernst-Planck* equation describes well the conservation of the charged species driven by a balance of diffusion, convection, and electromigration which are linearly superposed.

$$\frac{\partial C}{\partial t} = -\nabla \cdot \left[D\nabla C - \frac{Dze}{k_B T} C(\nabla \phi) \right] - \mathbf{u} \cdot \nabla C \tag{9}$$

$$\frac{\partial C}{\partial t} = -\nabla \cdot \mathbf{J} \tag{10}$$

where, z is the valence of ionic species, e is the elementary charge, ϕ is the electric potential, respectively. Since the external electric field is applied, the convection is composed of the PDF and the EOF. In addition, the electric field is much controllable compared to the PDF or the concentration gradient across the channel, so that the electromigration under the inevitable EOF is often used to transport ionic species in nanochannel.

1.4 Application of nanochannel-assisted microfluidic device

DNA stretching and analysis. Hybrid-scale LOC devices demonstrated their unique application in DNA stretching, which appears to be one of the first practical applications. A randomly coiled DNA molecule passes through a nanochannel where it is stretched and linearized because of the nanoscale, confined channel geometry that is near the diameter of the DNA. For this reason, coiled DNA molecules are forced to be stretched, thereby reaching their full contour length. As coiled DNA molecules are linearly stretched, it becomes easy to read or map their DNA sequences. For example, Park *et al*. demonstrated that DNA molecules in a solution individually penetrate through a nanochannel approximately 90–200 nm in width [34]. The DNA molecules were originally coiled but they were stretched 25–40% in length when flowing through the nanochannel using electrophoretic migration. Huh et al. demonstrated that elastomeric nanochannels fabricated by using the crack method can stretch single DNA molecules up to 30% of their full length, as shown in Fig 1-10(a) [32]. In addition, Kim et al. reported that single DNA molecules dissolved in a low concentration λ-DNA solution (1 pg/μl) were captured in nanochannels and linearized, as shown in Fig 1-10(b) [43]. They adjusted the width of the nanochannels by manipulating the stretchability of the channels that were fabricated by using the unconventional fracture method. Although DNA stretching was possible with the help of nanochannels, a microchannel network was indispensable for guiding dispersed DNA molecules from a reservoir to the entrance of the nanochannels. From this point of view, we note that hybrid-scale LOC devices are essentially needed and the unconventional nanofabrication techniques show high potential for facilitating the fabrication of such LOC devices.

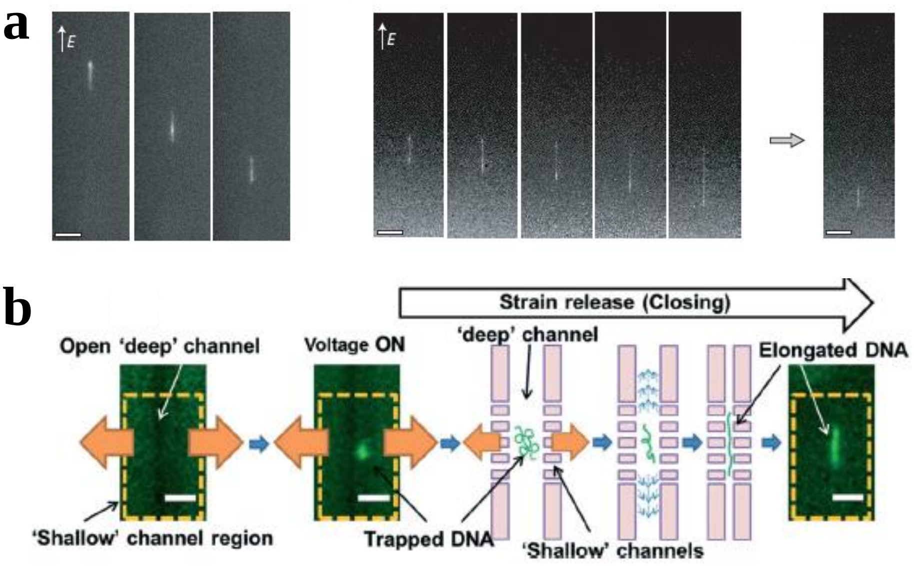

Figure 1-10. DNA stretching applications using hybrid-scale LOC devices fabricated by unconventional micro-/nanofabrication techniques. (a) Elastomeric crack-based nanochannels were fabricated and then applied to DNA stretching. (b) DNA concentration, trapping, and linearization using the hydrodynamic squeezing flow as the elongation of nanochannel is released. Figure (a) was adapted from Huh *et al.* [32], Figure (b) was adapted from Kim *et al.* [43]

Nanoelectroporation. Nanostructures and nanochannels are very useful for nanoscale electroporation, which is an essential and useful biological process. Electroporation is used for the transfection and delivery of small molecules, drugs, or DNA into cells through cellular membranes in conjunction with an electrical field. Recently, nanoelectroporation (NEP) has emerged as an improved electroporation method by accommodating nanochannels to allow electroporation at the single cell level. NEP devices consist of two adjacent microstructures and one connecting nanochannel. Gao et al. employed a nanowire-assisted fabrication method to fabricate two microstructures and one connecting nanostructure, as shown in Fig 1-11(a) [44]. One microstructure was used for a single cell residence while the other was used for loading materials to deliver. Using the LOC device, they showed precise gene transfection via a microchannel-nanochannel-microchannel array. They demonstrated that the array allows for higher effectiveness and more uniform plasmid delivery into mouse embryonic fibroblast cells. Owing to the connecting nanochannel, it was possible to not only control the precise dosage but also reduce cell damage and deformation since the nanochannel works as a passage channel to deliver materials into the cells. The same group also reported single cell analysis based on NEP with the molecular beacon technique using the same LOC device used in their previous report, as shown in Fig 1-11(b) [8]. Typically, it has been a hurdle to place a single cell in designated microstructures in many NEP devices.

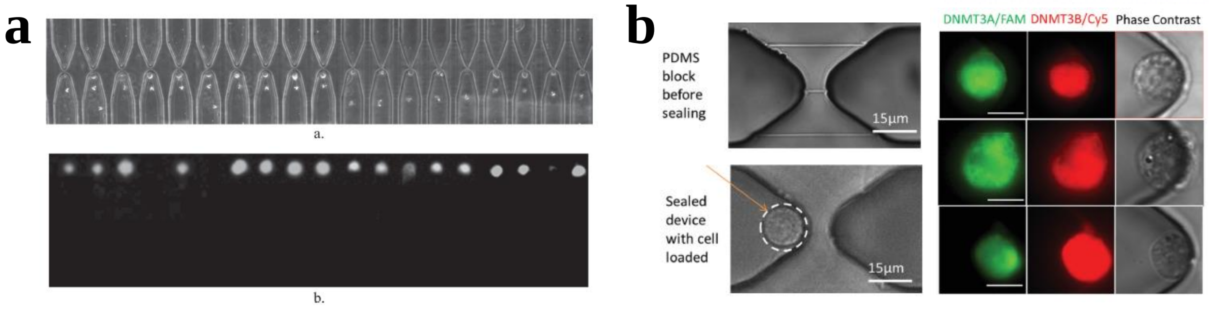

Figure 1-11. A nanowire-assisted nanochannel fabrication method was used to connect two neighboring microstructures for cell trapping and loading transfection materials. (a) Loaded cell express fluorescence signal after nanoelectroporation. (b) NEP applications for three individual wild-type Kasumi-1 cells. Figure (a) was adapted from Gao *et al.* [44], Figure (b) was adapted from Zhao *et al.* [8].

Nanoscale electrokinetics. Micro- and nanofabrication provide an unprecedented means to intensively explore on electrokinetics on a chip. Many electrokinetic LOC devices were developed using conventional fabrication techniques such as bulk etching, photolithography with subsequent etching, FIB for protein concentration [45], a nanofluidic diode [10], and DNA transport [22], respectively. Generally, such LOC devices require nanochannels or nanoslits to ensure the electrical double layers merge. As a result, ions are selectively allowed to penetrate through nanogaps, thereby causing an ion enrichment and depletion effect. As previously mentioned, a microchannel network is necessary to load and guide ionic solutions to the ends of the nanogaps. Therefore, a novel fabrication technique for a hybrid-scale LOC device can be beneficial for ease of study and further application of the electrokinetic phenomena for various applications. There have been several electrokinetic LOC devices developed by using unconventional fabrication techniques including the PDMS nanochannel collapse technique [9], and wrinkle [29], as shown in Fig 1-12. We note again that the nanofabrication techniques can rapidly and repeatedly provide a robust micro-/nanofluidic platform to investigate and apply electrokinetic phenomena on a chip.

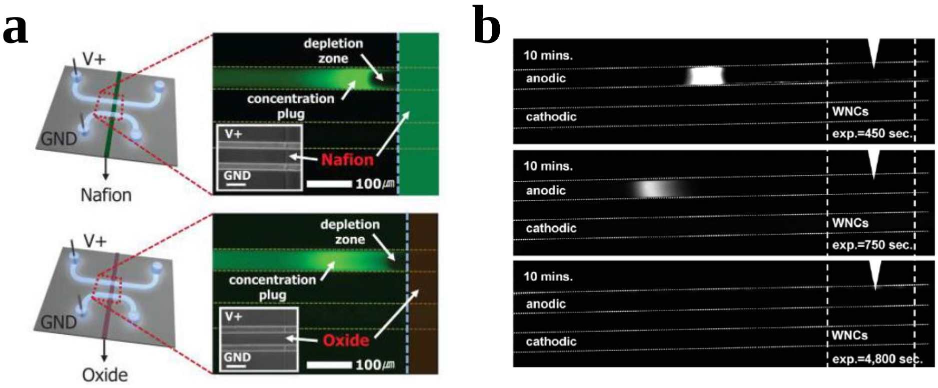

Figure 1-12. Nanochannel-assisted electrokinetic applications for preconcentration of ions and proteins. (a) PDMS microchannels were intentionally collapsed to produce nanochannels along the two edges of a thin membranes and then used for generating ion concentration and depletion zones. (b) Wrinkle-based nanochannel array was used for protein preconcentration. Figure (a) was adapted from Kim *et al.* [9], Figure (b) was adapted from Chung *et al.* [29].

Membrane-free diffusion-based LOC. Nanochannel arrays can replace porous membranes in LOC devices because they allow diffusive transport of small molecules while suppressing convective flow. For instance, Wang et al. reported a hybrid-scale LOC device replicated from a wrinkle-based mold and performed a chemotaxis assay with *Caenorhabditis elegans* (*C. elegans*), as shown in Fig 1-13(a) [46]. Since a nanochannel array integrated with a microfluidic device facilitates the generation of a concentration gradient, C. elegans chemotaxis was easily observed within minutes. Using the device, they demonstrated that nanochannel arrays can replace porous membranes when conducting versatile diffusion-based experiments. Monolithic molds with a nanochannel array and a microchannel network were adopted for producing membrane-free and diffusion-based LOC devices via soft-lithography. The LOC devices were fabricated in a batch process manner, showing a significant potential for high-throughput production. For example, Kim et al. introduced a hybrid-scale LOC device fabricated using a crack-photolithography-assisted mold and soft-lithography for analysis of the cellular responses, as shown in Fig 1-13(b) [11]. They controlled the rate of diffusion of small molecules by manipulating the number of nanochannels between two microchambers. And then, they further demonstrated that the device can quantify the cellular responses of the synthetic bacterial cells to inducer molecules, thereby indicating significant potential for cell-to-cell communication assays on a chip.

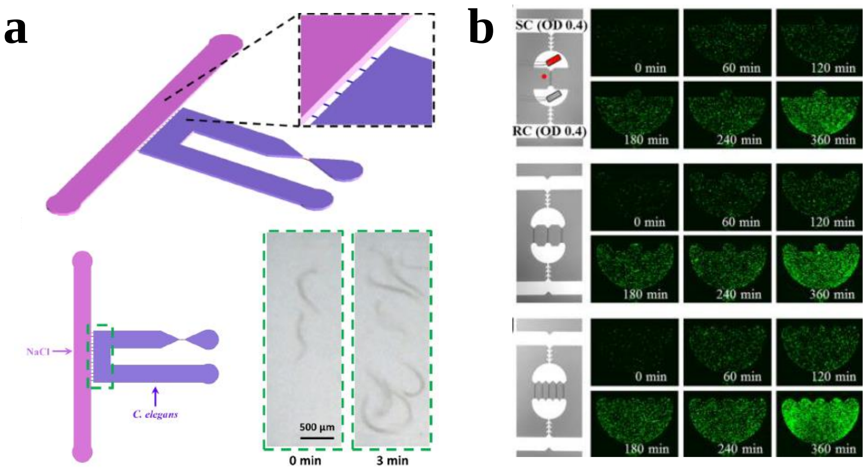

Figure 1-13. Applications of membrane-free diffusion-based LOC. (a) *C. elegans* chemotaxis experiment is conducted by producing a tunable concentration gradient of NaCl through nanochannel array. (b) Cell-to-cell communication experiment is conducted by inducing genetic circuit of *E.coli* with signaling molecules diffused through the crack-photlithography-based nanochannel array. Figure (a) was adapted from Wang *et al.* [46], Figure (b) was adapted from Kim et al. [11].

Various membranes have been integrated into LOC devices to control diffusive transport rates of small molecules. This membrane integration assisted in the advance of LOC technologies as well as the expansion of LOC applications into a variety of research fields. However, as previously discussed, membrane-integrated LOC devices require somewhat uncontrollable fabrication processes, thereby resulting in low reproducibility, reliability and throughput. Alternately, crack-assisted hybrid-scale molds and soft-lithography makes it possible to produce a microchannel network with a nanochannel array at the same time and on the same single layer. For this reason, we can conclude that nanochannel array-based LOC devices show advantages when compared to membrane-integrated LOC devices. In addition, it was demonstrated that a great number of nanochannels can be easily integrated with a highly complex microfluidic channel network containing numerous microchambers [38]. Therefore, unconventional fabrication techniques are considered superior to conventional fabrication techniques when developing diffusion-based microfluidic devices for high-throughput biological assays without membrane integration.

1.5 Overview of dissertation

Conventional nanofluidic studies have focused on electrokinetics-drvien mass transport studies using external electric fields, because they have the dominant mass transfer control capability in the nanochannel. However, utilization of the external electric fields consumes too much energy and causes an increase in size and cost to apply the miniaturized LOC. Thus, despite advantages of nanofluidics such as precise mass transport control, most of nanochannel-assisted microfluidic applications are limited to academic research area except studies dealing with DNA sequencing technique. In this context, this dissertation demonstrate diffusion-based mass transport control and application of it in micro/nanofluidic device, which is a precise and cost-effective way to bridge the gap between the academic laboratory and the commercial LOC using nanofluidics.

First of all, chapter 1 covers fundamentals in development of micro/nanofluidic devices, fabrication technique, theory to govern mass transport in the micro/nanofluidic device, and application for LOC.

*Note: This chapter is partially or totally adapted from Dogyeong Ha *et al.*, and Taesung Kim, "Unconventional micro-/nanofabrication technologies for hybrid-scale lab-on-a-chip", *Lab Chip*., 16(22), 4296-4312, Copyright © 2016 *Royal Society of Chemistry*, all right reserved.

Chapter 2 introduces a facile technique to fabricate nanochannel-integrated microfluidic device. Simple and inexpensive nanochannel fabrication technique is essential for the widely available LOC with nanofluidics. We demonstrated that a modified crack-photolithography and PDMS-based soft lithography facilitate the production of micro/nanofluidic device in a high-throughput manner with low cost and high reproducibility as well.

Chapter 3 describes diffusiophoresis, which is a novel and simple control of the motion of colloidal particles using the concentration gradient of solutes induced by diffusion of ions through the nanochannel. Because the difference in diffusion coefficient of cations and anions spontaneously produces an electric field, the colloidal particles with finite zeta potential can move in a designed direction when they are exposed to the solute gradient. Since the nanochannel simply produces solute gradient with the diffusion to the neighboring microchannels, the colloidal particles can be concentrated or extracted on-demand by controlling physicochemical environment without any external equipment or energy/power sources.

*Note: This chapter is partially or totally adapted from Dogyeong Ha *et al.*, " Dynamic transport control of colloidal particles by repeatable active switching of solute gradients", *ACS Nano*., 13(11), 12939-12948, Copyright © 2019 *American Chemical Society*, all right reserved.

Chapter 4 introduces practical applications of diffusiophoresis that can separate and fractionate a nanoparticle mixture by selectively extracting only one type of nanoparticles with respect to not only the size but also the zeta potential of it. In particular, we empirically validate for the first time the conventional theory of size-dependent diffusiophoresis for nanoparticles in this work.

*Note: This chapter is partially or totally adapted from Dogyeong Ha *et al.*, " Dynamic transport control of colloidal particles by repeatable active switching of solute gradients", *ACS Nano*., 13(11), 12939-12948, Copyright © 2019 *American Chemical Society*, all right reserved.

Chapter 5 demonstrates humidity-based gating of nanochannel for transport control of water and molecules. As introduced in Chapter 1.4, the nanofluidic channel has the feature of the ability to electrically prevent transport of molecules depending on the nature of the surface of nanochannel. This has a disadvantage that it is necessary to combine external electric fields according to the surface properties. In this chapter, we demonstrate a method for transport control of water by dehydration or rehydration of water molecules within the long nanochannel using the gas permeable nature of PDMS. Evaporation of water leaves molecules inside of the nanochannel due to a high hydraulic resistance of the long nanochannel, which can be used for not only nanofluidic valve but also capacitor of molecules. This technique can be extended to selectively and quickly respond to humidity-based nanofluidic gating using a control channel around a single nanochannel. This is the first demonstration of a LOC application that allows rapid control of water transport in nanochannel at the femtolitre-level without mechanical valve. Because the neighboring microchannel significantly affect the humidity level near the nanochannel, the single nanochannel gating is permitted by switching flow with dry or humid gas in the neighboring microchannel for the desired state.

Chapter 6 summarizes the contributions of this dissertation to the transport control of nanofluidics for the advanced LOC devices. In addition, we suggest the future perspective of the mass transfer control based on the diffusion method in nanofluidics for versatile micro/nanofluidic applications.

Chapter 2. Fabrication of Crack-Photolithography-based Polydimethylsiloxane Nanochannels

2.1 Introduction

Microfluidics has been remarkably developed due to the rapid design-to-prototyping techniques mainly enabled by standard photolithography and polydimethylsiloxane(PDMS)-based soft-lithography. In contrast, the development of nanofluidics, showing as promising potentials as microfluidics, seems to be relatively retarded, being attributed to the costly, time-inefficient, and low-throughput nanofabrication. To demonstrate simple fabrication of soft-lithography-based nanochannel, we previously developed “crack-photolithography” that fabricate hybrid-scale master mold with micro-/nanopatterns simultaneously in a single batch process, as shown in Fig. 2-1. We have also reported membrane-free and diffusion-controlled micro-/nanofluidic devices using crack-based nanochannel array in previous work. However, it was limited to very high dimension of crack pattern of which depth is larger than 300 nm. Also the study of diffusion-based mass transport through long nanochannel which is larger than 400 μm was not conducted. Since bio-applications in a high-throughput manner needs various length of nanochannels, the study of the diffusion-based mass transport through the long nanochannel is also necessary. Therefore, we develop new technique to establish the general conditions of diffusion-based mass transport for various either depth or length of PDMS-based nanochannels.

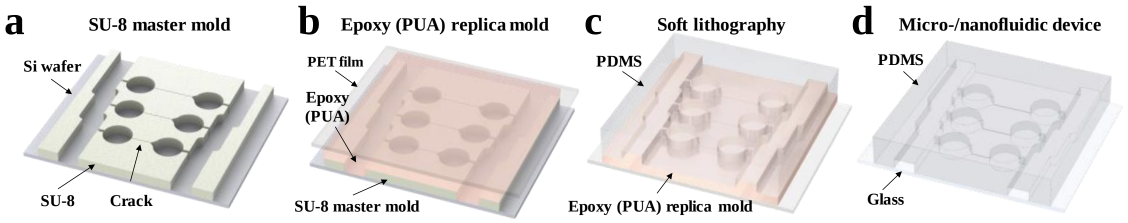

Figure 2-1. Fabrication process of crack-photolithography-based micro/nanofluidic device. (a) SU-8 master mold with negative crack nanopatterns is produced by crack-photolithography. (b) The SU-8 master mold is replicated by using polyurethane acrylate (PUA) and Polyethylene terephthalate (PET) film. (c) Nanochannel is produced by PDMS-based soft lithography from the PUA replica mold. (d) Oxygen plasma treated PDMS is attached to the glass substrate to form a hybrid scale micro/nanofluidic device.

In this chapter, modified crack-photolithography and enhanced soft lithography are introduced to fabricate hybrid-scale nanochannel-integrated microfluidic devices easily. First we modulated the fabrication parameters of crack-photolithography to increase aspect ratio (AR) of the nanopatterns to avoid roof-collapse of the nanochannel. Then, we introduced an extra hard PDMS (x-PDMS) layer as a supporting layer above the surface of regular PDMS to achieve both robustness and smooth demolding. A relatively low surface energy of normal PDMS helps easy demolding without any damage to the mold. At the same time, the nanochannel was not collapsed due to the inserted x-PDMS layer, which acts as a girder.

2.2 Standard process of crack-photoithography

Basically, crack-photolithography is largely divided into three parts; standard photolithography for generation of notch patterns, double exposure process for inhibition of unwanted cracking, and development process for propagation of cracks. Standard process of crack-photolithography is described in Fig. 2-2. i) SU-8 film is obtained on the 6-inch silicon wafer by spin coating. Because thinner films can be cross-linked more densely than thicker films under the same exposure energy, film thickness significantly affect the propagation velocity and aspect ratio of crack patterns, Thus, it is important to choose optimized fabrication condition for spin-coating speed and time. ii) The SU-8 film was then baked on a hot plate at 95 °C for 3 min to evaporate solvent. iii) The baked SU-8 film was exposed to ultraviolet (UV) light through the first photomask, which has micropatterns including crack initiation and termination patterns without any UV filters for generation of the gradient of crosslinking density from the surface to the bottom side of SU-8 film. iv) After the first post exposure bake (1^{st} PEB) on the hot plate at 95 °C for 3 min, v) the SU-8 films were developed for an additional 1 min to obtain micropatterns without agitation, which minimized unnecessary stress. vi) The SU-8 films were additionally exposed to UV radiation at 90 mJ/cm^2 under the second photomask for the complete suppression of unwanted cracking. vii) It was followed by the second post-exposure baking (2^{nd} PEB) under the same baking conditions. viii) Lastly, the second development process was employed for 30 min to generate crack nanopatterns only within the single-UV-exposed area.

Although crack patterns are significantly affected by film thickness and UV exposure energy, which has been already reported in our previous work [38], there are no studies about the effect of annealing condition on the crack dimension. In particular, this annealing condition affects the aspect ratio of crack patterns, which is important to avoid roof-collapse problem of PDMS nanochannel. Thus, we changed annealing condition to investigate optimal temperature and time for crack patterns with high aspect ratio.

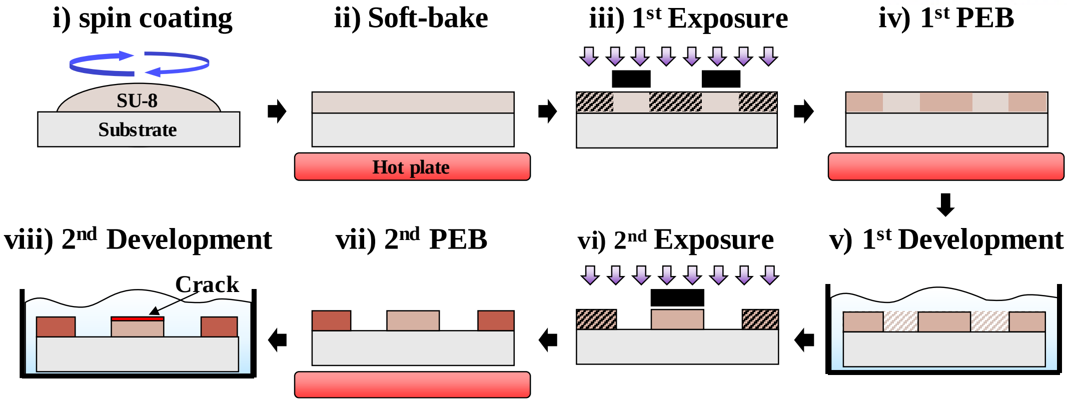

Figure 2-2. Fabrication process of standard crack-photolithography.

2.3 Experimental methods

Materials and reagents: A negative photoresist of SU-8 (SU-8 2010, MicroChem, Newton, MA) was mainly used, of which negative micro-/nanopatterns were replicated using a polyurethane acrylate (PUA, MINS-311RM) and polyethylene terephthalate (PET) film (all from Minuta Tech, Osan, Gyeonggi, Korea). The surface of the replicated positive PUA mold was silanized with Chlorotrimethylsilane (Sigma-Aldrich, Yongin, Gyeonggi, Korea). Soft lithography was performed by stacking triple layers of silicone-based materials including polydimethylsiloxane (PDMS, Sylgard 184 silicone elastomer kit, Dow Corning, Midland, MI, USA) and x-PDMS. The PDMS was prepared by mixing Sylgard 184 base and Sylgard 184 curing agent with mixing ratio 5:1. The x-PDMS consists of two parts: a mixture of vinyl functional part and cross-linker part. The main compound of the first vinyl functional part was prepared by mixing 10 g of linear vinyl siloxane (Cat. No. VDT-731) with 16 g of vinyl Q-siloxane (Cat. No. VQX-221) and evaporating the solvent in the air-purged oven at 65 °C for 2 days. And then, 1.8 g of the prepared mixture of siloxane was mixed with a 15 μL of platinum catalyst (Cat. No. SIT 7900.0) and 80 μL of moderator (Cat. No. SIP 6831.2LC). Lastly, the prepared vinyl functional part was mixed with 0.6 g of the second cross-linker (Cat. No. HMS-501). All chemicals used to prepare x-PDMS were purchased from JSI silicone (Seongnam, Korea). The transport of small molecules through nanochannel was characterized by quantifying the fluorescent intensities of 100 μM fluorescein isothiocyanate (FITC).

Experimental setup and data analysis: Optical and fluorescent images were obtained by using an inverted fluorescence microscope (Ti-U, Nikon, Japan) equipped with a CCD camera (ORCA R2, Hamamatsu Photonics, Japan). The fluorescence intensities of the images were quantitatively analyzed using Image J (1.45 s, National Institutes of Health, Bethesda, MD, USA). The normalized fluorescence intensities were drawn as graphs using OriginPro 2015 software (b9.2.272, OriginLab Corp., Northampton, MA, USA). The background signal of fluorescent intensity was subtracted for all quantitative analyses. Cross section images of nanochannels were acquired by scanning electron microscopy (SEM, SU-8220, Hitachi Ltd., Tokyo, Japan) by sputtering platinum on the cross section of the PDMS devices. The dimension of nanoscale cracks was imaged and quantified by using an atomic force microscopy (D3100, Veeco, USA). The data acquired from the temperature-humidity sensor was processed by using LabVIEW (National Instruments, USA).

Modified soft lithography for the fabrication of collapse-free PDMS nanochannel: The crack-photolithography was followed by soft-lithography to fabricate micro-/nanofluidic devices from the negative micro-/nanoscale patterns on SU-8 films using PUA and PET films. Replication process was performed in the custom-made nitrogen chamber to make oxygen-free environment. Since oxygen inhibits UV-based photocuring of the PUA, nitrogen chamber is necessary for accurate replication of the micro-/nanopatterns without considerable volume reduction. The surface of the replicated positive PUA mold was silanized to reduce surface energy for soft lithography. The process was performed by stacking PDMS and x-PDMS to prevent a roof-collapse problem and maintain clean surfaces at the same time. That is, the first layer of the micro-/nanofluidic device was produced by spin coating of PDMS at 3,000 rpm on the replicated PUA mold and curing in a hot oven at 65 °C for 20 min. And then, the prepared x-PDMS solutions was used to spin coating the PDMS-coated PUA mold at 500 rpm and followed by heating at 65 °C for 15 min in the oven again. Lastly, PDMS was poured onto the bi-layer PDMS and cured at 65 °C for 4 h.

2.4 Modulation of annealing condition of crack-photolithography

Fig. 2-3 shows the schematic of the effect of annealing condition of crack-photolithography on the dimension of crack patterns. The annealing temperatures for the soft-bake, 1st PEB, and 2nd PEB were modulated in the range of 75–125 °C to manipulate the geometrical dimensions of crack nanopatterns on SU-8 films. A field-effect scanning electron microscope (FE-SEM, S-4800, Hitachi, Japan) was used for observing the cross-sections and measuring the dimensions (width, depth, and aspect ratio) of the crack nanopatterns. The main components of SU-8 are monomers, organic solvents, and photo-acid generators (PAG). When the SU-8 films were exposed to UV-light through a photomask, the photo-acid is generated by PAG and cationic polymerization is initiated by the photo-acid diffusion through the SU-8 monomers, which leads to cross-linking [47, 48]. From our previous observations, it was found that the generation and prevention of crack patterns on SU-8 films can be controlled by cross-linking density [38]. In particular, the double exposure process was performed to prevent unwanted crack generation by increasing the cross-linking density at the double-exposed areas. In addition, it was reported that the crack density on SU-8 films increases upon decreasing the cross-linking density due to the increased absorption of solvent molecules [49, 50].

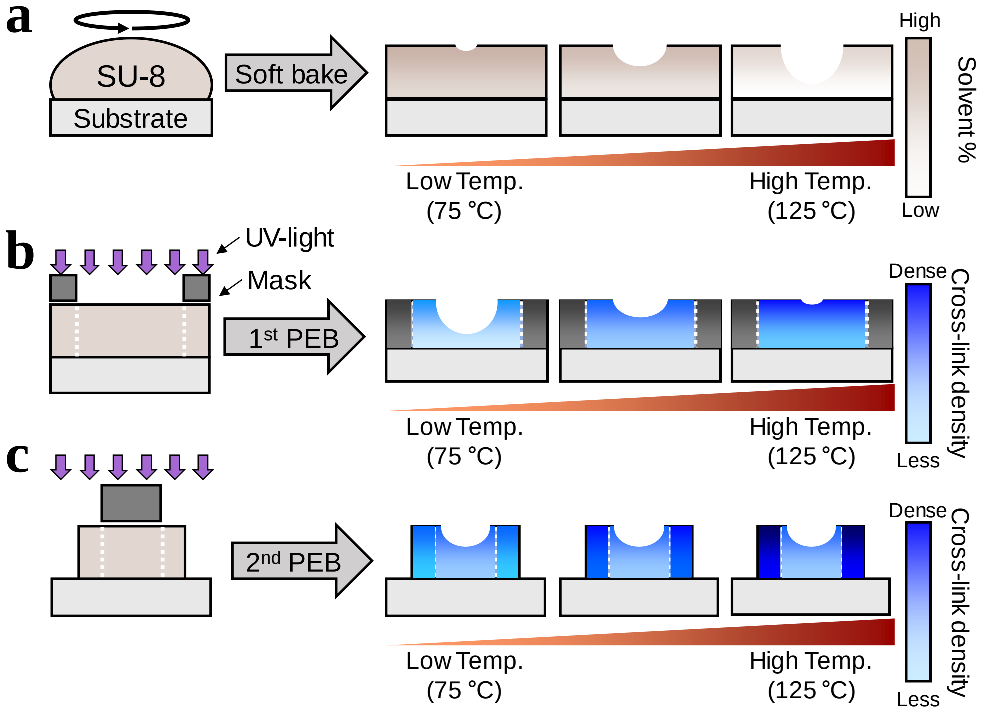

Figure 2-3. Schematic of the characterization for the geometrical dimension of crack nanopatterns on SU-8 films at six different annealing temperature in the 75–125 °C range, at 10 °C intervals. (a) Solvent concentration for the different soft-bake temperature. Cross-linking density for different annealing temperature of (b) 1st PEB and (c) 2nd PEB, respectively.

Fig. 2-4 represents the geometrical observation of crack nanopatterns at different annealing temperatures of the soft-bake, 1st PEB, and 2nd PEB, based on the cross-sectional FE-SEM images, as shown in Fig. 2-5. First, with increasing soft-bake temperature, the width and depth of crack nanopatterns increased and then leveled off around 95 °C, as illustrated in Fig. 2-4(a) and Fig. 2-4(a). However, the aspect ratios of the crack nanopatterns gradually decreased upon increasing the soft-bake temperature. This phenomenon can be explained in terms of the solvent concentration in the SU-8 film at different annealing temperatures employed in the soft-bake process [49]. The solvent, which is contained in the SU-8 film, not only provides the diffusion pathway but also aids the generation of the photo-acid [47]. During the soft-bake process, the solvent evaporates and the spin-coated SU-8 solution is solidified on the substrate. Accordingly, the evaporation rate and solvent concentration in the SU-8 film strongly depend on the annealing temperature in the soft-bake process. Thus, a higher solvent concentration (annealing at lower soft-bake temperature) increase the effective concentration and mobility of the photo-acid, and consequently, increase the cross-linking density. However, the solvent concentration reaches a constant level at temperatures of 95 °C and above, implying saturation of the cross-linking density [49]. The crack nanopatterns follow a trend similar to that shown by the cross-linking density. In the soft-bake process, the width and depth of crack nanopatterns gradually increase up to temperatures of 95 °C due to a decrease in the cross-linking density, which implies that the tensile stress is increased by the swelling. However, the width and depth of the crack nanopatterns are almost saturated and remain constant at temperatures higher than 95 °C.

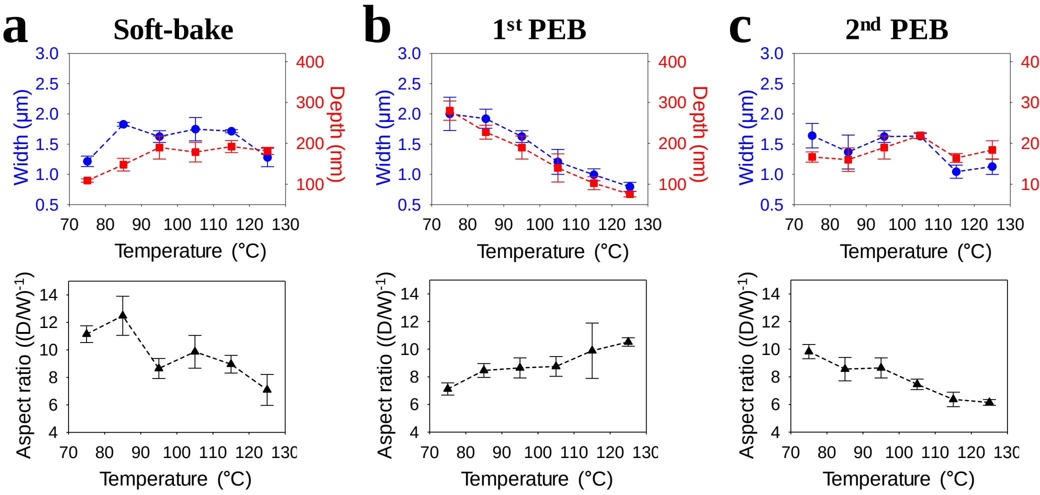

Figure 2-4. Geometrical dimension and resulted aspect ratio of crack patterns on SU-8 affected by six different annealing temperature with respect to (a) soft-bake, (b) 1st PEB, (c) 2nd PEB, respectively.

After exposure to UV light, the PEB process is performed for selectively accelerating the cross-linking of the exposed area. Upon increasing the PEB annealing temperature, the cross-linking density is increased since the diffusion of the photo-acid is promoted and the mobility of the SU-8 monomers is increased [48]. For crack-photolithography, the PEB process is performed twice. The 1st PEB process leads to cross-linking of all the micro-patterns (Fig. 2-4(b) and Fig. 2-5(b)), while the 2nd PEB process results in cross-linking the double-exposed area (Fig. 2-4(c) and Fig. 2-5(c)), thus preventing unwanted cracks on the SU-8 film. By increasing the annealing temperature of the 1st PEB process, the entire micropatterned area, including crack propagation area, is increased; therefore, the width and depth of the crack nanopatterns gradually decrease. However, the 2nd PEB process can only contribute to the cross-linking density of the double-exposed area. Therefore, the geometrical dimensions of the crack nanopatterns are not significantly different. Then, we conducted annealing under the optimal conditions by choosing the deepest crack nanopattern of each process for generating the crack nanopattern with the highest and lowest aspect ratio. From these evaluations, the optimum annealing temperatures for the soft-bake, 1st PEB, and 2nd PEB were selected as 95, 75, and 105 °C, respectively.

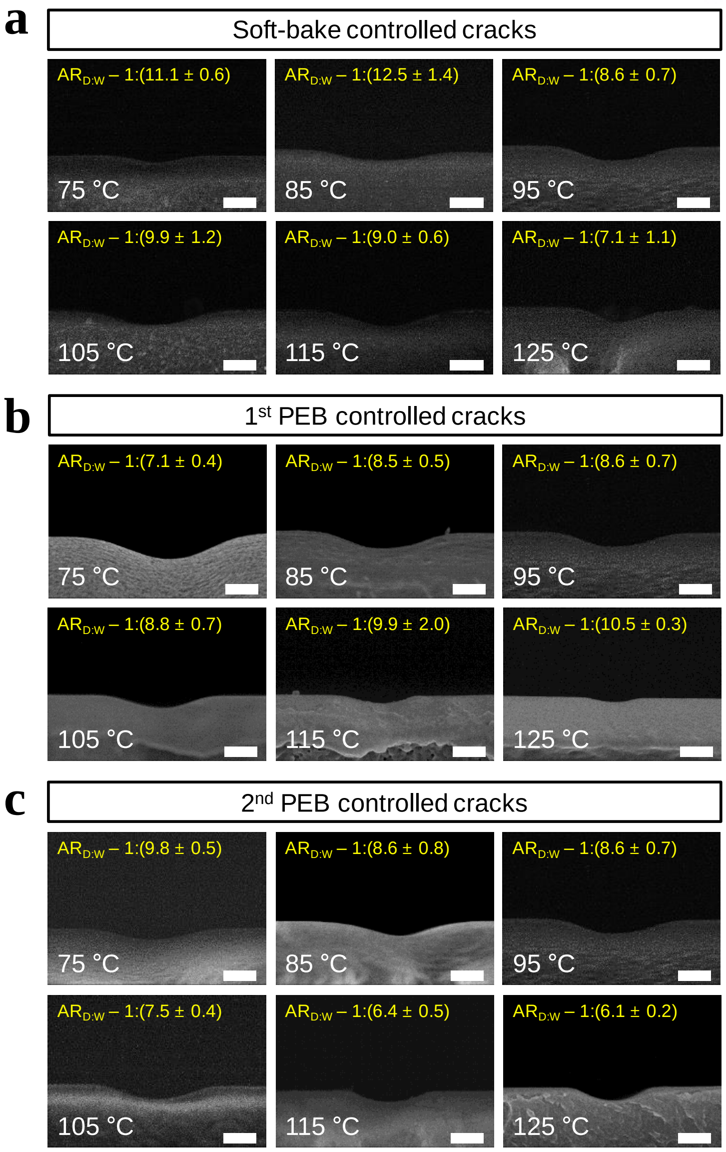

Figure 2-5. Cross-sectional FE-SEM images of crack nanopatterns on the SU-8 films under different annealing conditions: (a) soft-bake, (b) 1st PEB, and (c) 2nd PEB.

2.5 Fabrication of collapse-free PDMS nanochannel

Although modulation of annealing condition in crack-photolithography helps to increase the aspect ratio of crack pattern, geometrical dimension is still susceptible to be collapsed below 300 nm in depth due to the low elastic modulus of PDMS. Typically, hard PDMS (h-PDMS) is often used to increase elastic modulus of PDMS, but this has a drawback of brittle property inducing fracture during the demolding process. Therefore, this approach has poor reproducibility because the residue of broken h-PDMS sticks to the surface of the mold. Thus, we develop the modified soft lithography to fabricate collapse-free PDMS nanochannel with high reproducibility.

Fig. 2-6(a) describes the fabrication process of the modified soft lithography produced by inserting x-PDMS layer as a supporting layer between regular PDMS layers. Because soft surface should be used for clean demolding, the regular PDMS is introduced as a first layer of the device by spin coating at 3000 RPM on the PUA replica mold. Then, the regular PDMS is cured in a hot oven at 65 °C within 20 min, because the nanochannel of fully cured regular PDMS is eventually collapsed due to the low elastic modulus. Next, partially cured regular PDMS is coated by degassed x-PDMS solution followed by curing in a hot oven at 65 °C for 15 min, which forms a supporting layer for the regular PDMS. Because reactive molecules remain at the interface between the regular PDMS and x-PDMS layers, the additional curing causes an irreversible bond of the two layers [51]. Lastly, another regular PDMS was poured onto the bi-layer PDMS and cured at 65 °C for 4 h. Resulted PDMS composite shows the feature of monolithic layers sharing same dimethylsiloxane that makes it avoid adhesion failure and the problem induced by thermal stress after demolding, as shown in Fig. 2-6(b). Fig. 2-6(c) shows that crack nanopatterns have the relatively high aspect ratio (AR ~ 1:7) with 2 μm in width and 280 nm in depth, respectively. In addition, cross-sectional FE-SEM image further confirms that the tri-layer PDMS composite forms stable and collapse-free nanochannel below 300 nm in depth, as shown in Fig. 2-6(d).

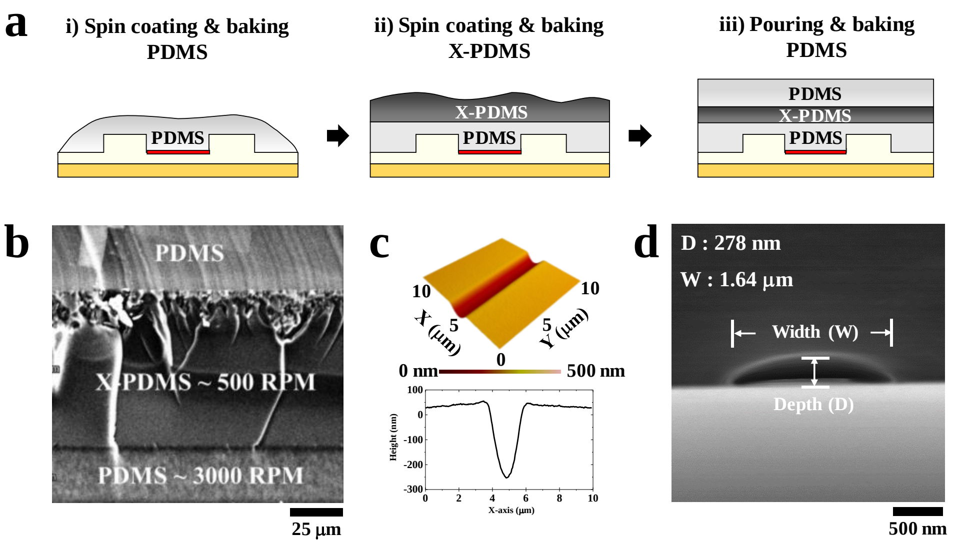

Figure 2-6. Fabrication of tri-layer PDMS composite to avoid roof-collapse problem of nanochannel. (a) Schematic shows the fabrication process of PDMS composite by stacking regular PDMS and x-PDMS sequentially. (b) Cross-sectional FE-SEM image of PDMS composite. (c) AFM image of PDMS nanochannel. (d) Cross-sectional FE-SEM image of nanochannel after bonding to glass substrate.

To compare the quality of nanochannel with conventional approach, we additionally prepare two types of the conventional PDMS device using regular PDMS and h-PDMS. The regular PDMS device is prepared by mixing Sylgard 184 base and Sylgard 184 curing agent with 5:1 ratio and curing in a hot oven at 75 °C for 4 h. The h-PDMS, which consists of VDT-731 (3.4 g, JSI Silicone, Seongnam, Korea), a platinum catalyst (18 µL, JSI silicone), and 2,4,6,8-tetramethyltetravinylcyclotetrasiloxane (4 µL, Sigma-Aldrich)7, was spin-coated at 1,000 rpm on the PUA mold and cured in a hot oven at 75 °C for 30 min. Then, the PDMS mortar was poured onto the h-PDMS-coated PUA mold, followed by curing in a hot oven again at 75 °C for 4 h. We used oxygen plasma treatment to attach the device to the glass substrate for all cases.

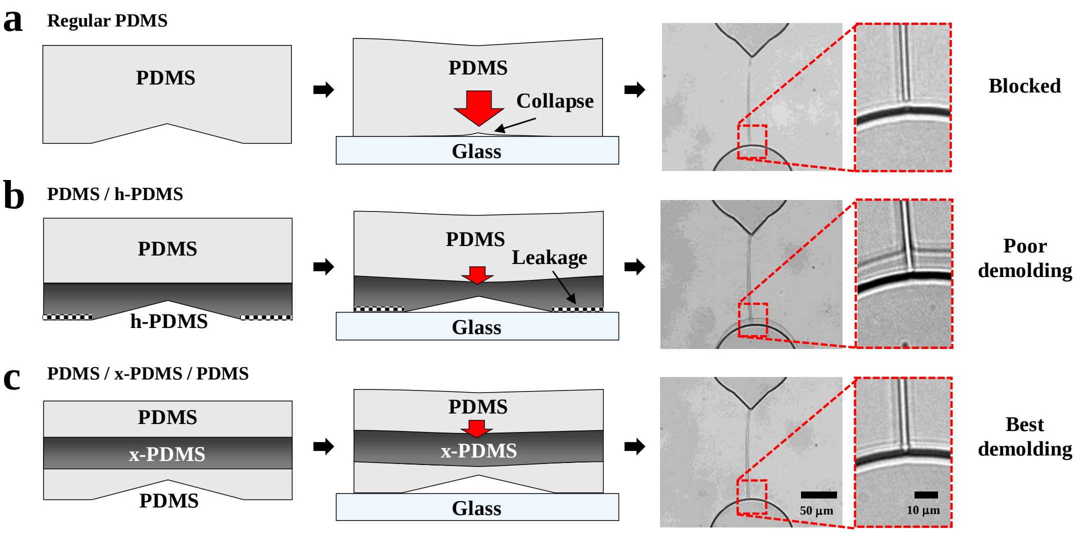

Figure 2-7. Schematic illustration and microscopic image for soft lithography showing (a) blocked nanochannel in the regular PDMS device, (b) alive nanochannel but poor demolding in bi-layer PDMS composite using h-PDMS and regular PDMS device, (c) best demolding in tri-layer PDMS composite using x-PDMS as the supporting layer between the regular PDMS layers.

Fig 2-7 shows the comparison the quality of nanochannels between three different types of PDMS. Fig 2-7(a) shows the nanochannel produced by regular PDMS. Although crack nanopatterns of regular PDMS surface is partially alive due to the increased aspect ratio modulated by annealing condition in crack-photolithography, this is still vulnerable to be collapsed because of low elastic modulus of PDMS. Fig 2-7(b) shows the nanochannel produced by bi-layer PDMS composite as the conventional method to avoid roof-collapse using h-PDMS surface. The nanochannel is not collapsed in all regions due to the high elastic modulus. However, h-PDMS surface is easily broken near the corner of micropatterns due to the relatively high adhesion force at the interface of PUA replica mold and h-PDMS during the demolding process. This defect induces not only leakage of the fluid in the device but also failure of the replica mold due to the sticky residue of h-PDMS. On the other hand, tri-layer PDMS composite shows non-collapsed nanochannel from the inlet to the outlet without any damage to the surface. Obviously, the replica mold has no damage either, so that this fabrication method facilitates continuous production from the same mold that guarantees collapse-free nanochannel with the high reproducibility.

It was followed by soft lithography using multilayers of polydimethylsiloxane (PDMS). In general, PDMS has a low elastic modulus that makes PDMS microchannels deformed well and PDMS nanochannels collapsed easily. We developed a novel demolding process by placing x-PDMS, which shows a high elastic modulus, directly above the thin, normal PDMS layer, avoiding roof-collapse of the nanochannels (> 100 nm in depth). The dimension of nanochannel can be controlled easily by changing the annealing condition in either soft bake or post exposure bake processes during crack-photolithography. In this platform, we adopted the nanochannel of which depth is larger than 100 nm to avoid roof collapse problem and overlapping electrical double layer simultaneously.

2.6 Conclusion and future perspectives

We developed a modified process of crack-photolithography and soft lithography to simply produce the collapse-free PDMS-based nanochannel in the laboratory level. We optimized annealing conditions of crack-photolithography to produce crack nanopatterns with high aspect ratio by controlling temperature and time in the process of soft-bake, 1st PEB, and 2nd PEB. We also demonstrated that the modified soft lithography to achieve not only the collapse-free nanochannel but also the damage-free master mold after demolding. In particular, the same mechanism can be used for the not only crack-photolithography-based master mold but also various nanoscale master mold such as wrinkle-, pyrolysis-, micromachining-based methods mentioned in chapter 1. The suggested fabrication technique enables to easily produce PDMS-based nanofluidic devices in inexpensive, rapid, and high-throughput manners, thereby not only facilitating the production of micro-/nanofluidic devices but also further expanding the use of such devices to a variety of unexplored applications.

Chapter 3. Micro/Nanofluidic Diffusiophoresis Platform for On-Demand Concentration and Extraction of Colloidal Particles

3.1 Introduction

Most bio-samples must be preconcentrated [52-56], separated [57-66], and extracted [67-69] in accordance with their features for specific purposes. Therefore, the mechanisms of transport of colloidal particles, which can be used as bio-sample models, have been intensively studied in miniaturized systems called micro-total-analysis systems (μTASs) [70-72]. Versatile phoresis mechanisms have been studied and introduced to the manipulation of colloidal particles on a chip, including electrophoresis,[73-75] dielectrophoresis [71, 76-78], acoustophoresis [57, 79-81], optophoresis [82, 83], and thermophoresis [84, 85]. These mechanisms are named for the applied power source or energy which they utilize, as they depend on external equipment or energy/power sources. Therefore, the aforementioned manipulation techniques inevitably increase the complexity, size, and cost of the overall system, deteriorating its portability despite the sufficient miniaturization of the essential manipulation part through the merits of μTAS. More recently, diffusiophoresis has attracted significant attention as a hopeful particle manipulation means because it enables the spontaneous migration of colloidal particles using an induced solute gradient [86-88]. Diffusiophoresis can be applied to most colloidal particles, including nanoparticles [87], DNA [89, 90], and cells [91, 92], with electrical charge of their surfaces (*i.e.*, inducing a zeta potential ζ_p) [86, 87]. This phenomenon is determined by solute gradients formed around the particle surfaces [93-95].

However, it is still necessary to address the several limitations in existing diffusiophoresis-based particle manipulation approaches and corresponding devices. First, diffusiophoresis lasts only for some minutes, because the solute gradient in the dead-end channel gradually disappears over time [86, 87]. Therefore, a long-term and stable gradient of solutes must be generated and maintained for diffusiophoresis-based applications. Second, membranes can facilitate the long-term diffusive mass transport of solutes while minimizing advection flow to the particles, but a sophisticated technique for diffusion control has not yet been realized on a chip. This is attributed to the difficulty of integrating a membrane structure with sufficiently high diffusion controllability with a microfluidic channel network. Many membrane-structure fabrication methods have been reported to date, but their low mechanical stabilities, slow response times (*e.g.*, low diffusivities), and low throughputs and yield rates must be resolved in fabricating microfluidic devices [91, 96]. Third, miniaturization has not been realized for the integration of equipment as active alternatives to passive membrane structures. External power sources such as fluid controllers or pressure regulators must be utilized to generate and manipulate solute gradients on a chip without a membrane structure; however, these would increase operation complexity, system size, and the net cost of the µTAS [89, 90, 97]. Hence, further effort is required to develop an innovative diffusiophoresis platform *via* a simple and robust batch-fabrication technique that can generate and manipulate diffusiophoresis with applied directionality and repeatability.

Here, we demonstrate an active particle manipulation technique using a micro/nanofluidic diffusiophoresis platform (MNDP) that can rapidly generate, stably maintain, and dynamically switch solute gradients. We develop a batch microfabrication by employing cracking-assisted photolithography (crack-photolithography) and modified soft-lithography for fabricating a polydimethylsiloxane (PDMS)-based devices where a crack-nanochannel successfully suppresses advection flow but allows diffusive mass transport towards the target chamber. The robust MNDP facilitates the rapid switching of physicochemical environments without significant hydrodynamic effects on the colloidal particles, allowing the versatile manipulation of target samples. We further demonstrate the concentration and on-demand extraction of target samples by the MNDP by simply switching the physicochemical environments in the opposite direction (*i.e.*, reverse diffusiophoresis). In addition, we characterize the effects of surfactants and solute concentrations on the diffusiophoretic mobilities of the target samples, with theoretical support *via* numerical simulations. Also, we demonstrated the potential application for genetic induction assay from the preconcentration to the extraction of raw samples on a single chip. The proposed microfabrication processes for the MNDP and the manipulation technique for colloidal particles may broaden the utilization of µTAS.

3.2 Experimental setup

Materials and reagents: A negative photoresist of SU-8 (SU-8 2010, MicroChem, Newton, MA) was adopted to fabricate the master mold. Negative micro/nanopatterns were replicated using polyurethane acrylate (PUA, MINS-311RM) and polyethylene terephthalate (PET) film (Minuta Tech, Osan, Gyeonggi, Korea). The surface of the replicated positive PUA mold was silanized with chlorotrimethylsilane (Sigma-Aldrich, Yongin, Gyeonggi, Korea). A micro/nanofluidic chip was produced using regular PDMS (Sylgard 184 silicone elastomer kit, Dow Corning, Midland, MI, USA) and an hard PDMS (x-PDMS). All chemicals used to prepare x-PDMS were obtained from JSI Silicone (Seongnam, Korea); vinyl Q-siloxane (VQX-221), linear vinyl siloxane (VDT-731), platinum catalyst (SIP 6831.2LC), moderator (SIT 7900.0), and linear hydride siloxane (HMS-501). To visualize and quantify the rate of mass transport, fluorescein isothiocyanate (FITC, Sigma-Aldrich, Yongin, Gyeonggi, Korea) was prepared by dissolving it in phosphate-buffered saline (PBS, Sigma-Aldrich, Yongin, Gyeonggi, Korea). Potassium chloride (KCl), sodium chloride (NaCl), potassium acetate (K-acetate), and Pluronic F-127 were obtained from Sigma-Aldrich. Fluorescent polystyrene latex particles, including red fluorescent 1-µm carboxylated polystyrene was purchased from Thermo Fisher.

Fabrication of micro-/nanofluidic devices: We adopted crack-photolithography using the same process described in our previous work to obtain a hybrid-scale micro-/nanofluidic device mold.[11, 38] Micropatterns, including a pair of sharp notches and blunt structures, generated cracks induced by tensile stress during the development on the SU-8 film. Negative patterns were replicated using PET film and PUA solution. A custom-made nitrogen chamber was used to minimize the effects of oxygen inhibition on the photocuring of the PUA solution. To resolve the roof-collapse problem and improve the reusability of the mold, we introduced modified-soft-lithography using a PDMS composite comprising stacked triple layers of PDMS and x-PDMS. Regular PDMS was first spin-coated at 3,000 rpm onto the replicated PUA mold and cured in a hot oven at 65 °C for 20 min. This was followed by the fabrication protocol of the bi-layer structure with PDMS and x-PDMS.[98] The prepared x-PDMS solution was used to spin-coat the PDMS−PUA mold at 1,000 rpm, followed by heating at 65 °C for 15 min in the oven. Lastly, regular PDMS was poured onto the x-PDMS layer and cured at 65 °C for at least 4 h. The produced PDMS nanochannel was additionally annealed in a furnace at 160 °C for at least 1 h to increase its Young's modulus. Subsequently, the PDMS surface and a glass substrate were treated with oxygen plasma (20 sccm, 50 W for 30 s) to yield hydrophilic surfaces with strong and irreversible bonding.

Sample preparation and handling: Carboxylated polystyrene particles measuring 1 μm were dispersed in various ionic solutions such as NaCl and KCl with the final concentration of 0.05 w/v% to demonstrate the accumulation of negatively charged particles. For colloidal particle accumulation, the concentration gradient of NaCl or KCl was produced by injecting a high solute concentration into the source channel and a low solute concentration into the target chamber for 5 min. Subsequently, the low solute concentration in the target chamber was changed to the particle solution. After sample enrichment, the particle solution was changed to pure distilled water. Subsequently, the high solute concentration in the source channel was changed to high-concentration K-acetate to extract the preconcentrated particles, unless otherwise noted.

Preparation of bacterial cells: We used recombinant *Escherichia coli* (*E. coli)* DH10B transformed with synthetically engineered genetic circuits to express green fluorescent signal induced by acyl-homoserine lactone (AHL). To culture *E. coli* DH10B, a single colony grown on a Luria Broth (LB) agar plate was inoculated in 5 mL of LB medium with 100 μg/ml ampicillin. Then, the colony was incubated for 10 h in a rotary shaker (200 rpm, 36 °C), resulting in the OD_{600} value marked 1.0. Cells were centrifuged at 5000 rpm for 3 min, and the pellet was resuspended to fresh M9 minimal media. All chemicals used to prepare bacterial cells were purchased from Sigma-Aldrich.

Experimental setup and data analysis: Optical and fluorescent images were obtained by using an inverted fluorescence microscope (IX-71, Olympus, Japan) equipped with a charge-coupled device (CCD) camera (Clara, Andor, Belfast, Northern Ireland). The fluorescence intensities FI of the images were quantitatively analyzed using Image J (National Institutes of Health, Bethesda, MD, USA) and

OriginPro 2015 software (OriginLab Corp., Northampton, MA, USA). The background signal of FI was subtracted for all quantitative analyses. The dimension of nanoscale cracks was imaged and quantified using atomic force microscopy (AFM; D3100, Veeco, USA). Oxygen plasma treatment equipment (Cute-MP, Femto Science, Hwaseong, Korea) was introduced to bond the glass substrate and the PDMS. A syringe pump (Harvard Apparatus, Holliston, MA, USA) was employed to characterize the inhibition effect of the convection flow through the nanochannel. Zetasizer (Nano-ZS, Malvern Panalytical) was used to measure the zeta potentials of the polystyrene particles.

3.3 Results and discussion

Fig 3-1(a) illustrates a hybrid-scale MNDP that can produce and maintain a stable solute gradient for long-term diffusiophoresis assays on a chip. We introduced the crack-photolithography fabrication method demonstrated in our previous work to produce PDMS-based micro/nanofluidic networks [38], as described in the Methods. The MNDP is composed of two main channels connected with a target chamber and a cracking-assisted nanochannel. The top main channel is for loading a plain solution containing colloidal particles with a low solute concentration (c_L); the bottom main channel as a source channel is for loading a salty solution with a high solute concentration (c_H) for the manipulation of colloidal samples. The target chamber and the bottom main channel are connected with a single nanochannel ($L = 5$ μm). Fig. 3-1(b) shows the fabricated MNDP, where the channel network including the nanochannel is visualized using a fluorescein isothiocyanate (FITC) solution. This demonstrates that the nanochannel is robust and stable without deformation , collapse, and fluid leakage. Fig. 3-1(c) describes an atomic force microscope (AFM) image of a fabricated nanochannel, which is 2 μm wide and 190 nm deep near the junction with the bottom main channel. Fig. 3-1(d) shows the power-free and on-demand manipulation of colloidal particles using the MNDP. Negatively charged colloidal particles in the top main channel are concentrated in the presence of the NaCl concentration gradient *via* inward diffusiophoresis. Then, the concentrated colloidal particles are extracted by generating a K-acetate concentration gradient by simply switching the solution in the bottom main channel. Notably, the buffer change between these two processes is performed easily because the nanochannel exerts no pressure-driven hydrodynamic effect on the colloidal particles.

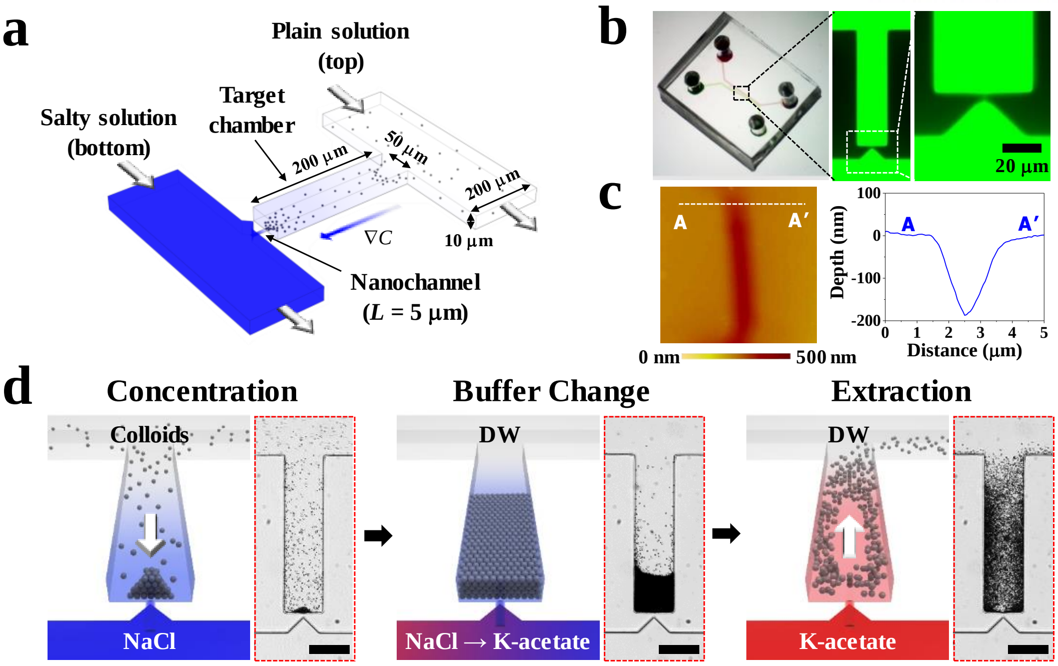

Figure 3-1. Concept, fabrication, and working principle of the hybrid-scale micro/nanofluidic diffusiophoresis platform (MNDP). (a) Schematic of the MNDP to produce a stable solute concentration gradient in the target chamber through a single nanochannel. (b) Photographs of the MNDP filled with 1 mM of fluorescent dye. (c) Atomic force microscopic (AFM) image that shows the morphology of the nanochannel. (d) Schematic of the working process of the MNDP for the on-demand concentration and extraction of colloidal particles using two solutions of NaCl and K-acetate, which are easily and conveniently switched by simple pipetting. Insets show the bright-field images of the 1-μm carboxylated polystyrene particles. Scale bars are 50 μm.

Because such nanochannels have high hydraulic resistances, the advection flow induced by the pressure difference between the two neighboring microchannels is negligible. As shown in Fig. 3-2(a) and (b), even under a high applied pressure difference between the channels, no colloidal particles are observed to enter the target chamber. However, the nanochannels are deep enough (~200 nm) to transport all ions in a diffusive manner without exclusion by the overlapped electrical double layer (EDL, κ^{-1} = ~3 nm, C = 10 mM) [86, 99]. These nanochannel features facilitate the active regulation of a physicochemical environment in the target chamber by simply loading ionic solutions with a pipette [11]. Fig. 3-2(c) shows that characterization result of the concentration and its gradient in the target chamber by quantifying the fluorescence intensities and demonstrated the rapid manipulation of the physicochemical environment of the target chamber without external power sources or fluid controllers. We introduced 1-mM FITC molecules dissolved in a 1-mM phosphate-buffered saline (PBS) solution to the bottom source channel and a pure 1-mM PBS solution to the top main channel. After measuring the fluorescence intensities (FI) along the A–A′ line for 5 min, we changed the FITC solution in the bottom source channel to pure PBS to confirm the time required to change the physicochemical environment in the target channel by measuring the FI at the same position. We normalized the measured FI relative to the maximum value. Approximately five minutes were necessary to completely refresh the chemical environment of the target chamber using a FITC solution. Fig. 3-2(d) shows the level of concentration gradient of FITC diffused through the nanochannel. We introduced FITC solution to the source channel with the concentration from 100 μM to 1 mM. Then, we compared the fluorescence intensity of the source channel and the target chamber in which the concentration gradient is produced. The maximum fluorescence intensity near the nanochannel is diluted by a factor of 40 compared to that of the source channel for all cases.

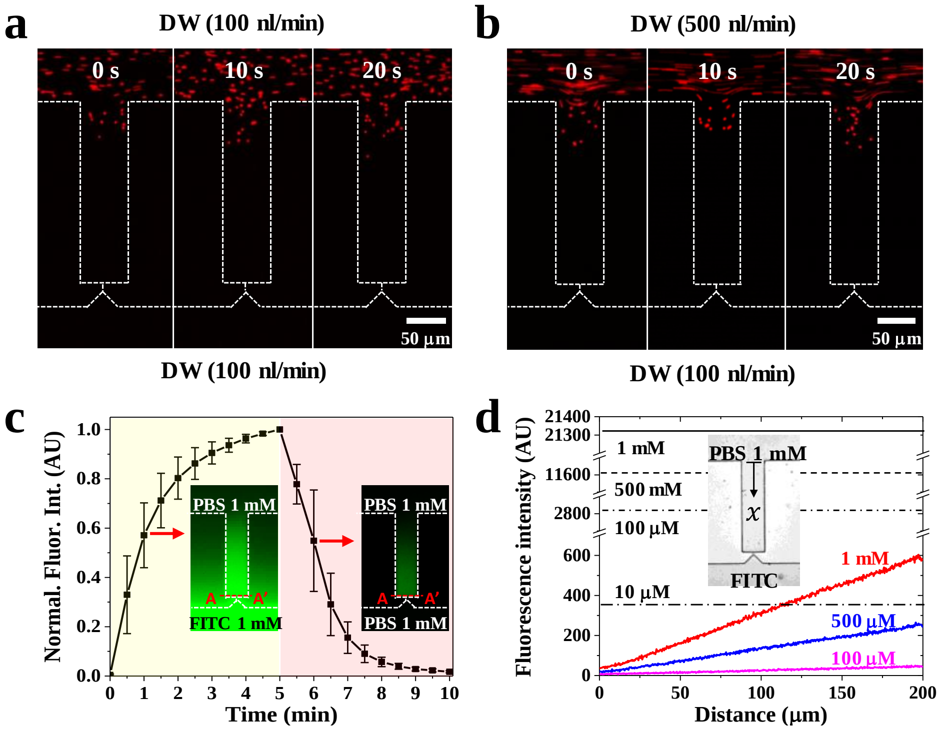

Figure 3-2. Characterization of mass transport through the nanochannel. Transport of 1-μm carboxylated polystyrene under the pressure difference formed with (a) Q_m = 100 nL/min, Q_s = 100 nL/min, (b) Q_m = 500 nL/min, Q_s = 100 nL/min. (c) Graph shows the normalized fluorescence signal across the A–A' dashed line indicating the junction between the target channel and the nanochannel. Insets show fluorescence images of the formation of the FITC concentration gradient and its subsequent washing in the target channel. (d) Graphs shows the diffused molecules are diluted by a factor of 40 due to the difference of cross-sectional area between the target chamber and nanochannel.

Fig. 3-3(a) describes the working mechanism of the MNDP as a concentrator that accumulates colloidal particles on a chip. A low-concentration ionic solution with colloidal particles is loaded into the top main channel, while another high-concentration ionic solution is loaded into the bottom main channel. This experimental condition produces a solute gradient, which spontaneously induce the motion of colloidal particles and fluid flow across the target chamber. In deatil, the velocity of colloidal particles is defined as $\mathbf{v}_p = \mathbf{v}_f + \mathbf{v}_{DP},$ where $\mathbf{v}_f$ is the velocity of fluid flow and $\mathbf{v}_{DP}$ is the diffusiophoretic velocity of the particles. The fluid flow is produced by *Poiseuille* and diffusioosmotic flows induced by the solute concentration gradients in the target chamber.[86, 87] To solve the *Poiseuille* flow, we introduced the NSE and continuity equations describing the motion of incompressible flow. The diffusioosmotic flow is derived from a wall slip velocity, which is induced by the solute concentration gradient at the charged plane of the wall. The wall slip velocity is defined as $\boldsymbol{v}_{f,w} = -\Gamma_w \nabla \ln C$, where Γ_w is the diffusioosmotic mobility and C is the solute concentration. Because the electrical double layer (EDL) of the wall is very thin (κ^{-1} ~ 3 nm) in a 10-mM monovalent solution, the size-independent diffusioosmotic mobility takes the form[87]

$$\Gamma_w = \frac{\varepsilon}{\eta}\left(\frac{k_B T}{ze}\right)^2 \left[\beta\left(\frac{ze\zeta_w}{k_B T}\right) + 4\ln\left(\cosh\frac{ze\zeta_w}{4k_b T}\right)\right] \tag{11}$$

where ε is the permittivity of the medium, ζ_w is the particle zeta potential, η is the viscosity of the medium, k_B is the Boltzmann constant, T is the temperature of the system, z is the valence of the solute, and e is the elementary electric charge. $\beta = (D_+ - D_-)/(D_+ + D_-)$, where D_+ and D_- are the diffusivities of cations and anions, respectively [87]. The first and second terms of Eq. (3) represent electroosmosis and chemiosmosis, respectively. Similarly, the contribution of diffusiophoresis of the particle can be obtained from the flow near the charged particle surface induced by the solute concentration gradient, which drives the particle in the direction opposing fluid flow. The diffusiophoretic velocity is expressed as $\boldsymbol{v}_{DP} = \Gamma_p \nabla \ln C$, where Γ_p is the diffusiophoretic mobility. In the simplest case of a size-independent value with a thin EDL approximation ($\kappa a \to \infty$), Γ_p has similar terms to those of diffusioosmotic mobility with the zeta potential of the particle and takes the form[87]:

$$\Gamma_p = \frac{\varepsilon}{\eta}\left(\frac{k_B T}{ze}\right)^2 \left[\beta\left(\frac{ze\zeta_p}{k_B T}\right) + 4\ln\left(\cosh\frac{ze\zeta_p}{4k_b T}\right)\right] \tag{12}$$

where ζ_p is the zeta potential of the wall. Typically, the motion of colloidal particles in solute gradient is dominated by diffusiophoresis, because the effect of diffusioosmotic flow is negligible if the particles are away from the wall. Therefore, the local solute gradient drives the spontaneous motion of the colloidal particles *via* diffusiophoresis, consisting of an osmotic pressure gradient near the particle surfaces (chemiphoresis, CP) and an imposed electric field from the diffusivity differences of the ions (electrophoresis, EP), as shown in Fig 3-3(b) [93]. For this platform, CP acts inward, toward the target chamber, because it always acts toward the higher solute concentration. However, the EP direction is determined by the sign of the zeta potential of the particles and the diffusivity difference of the used ions. In the present setup, NaCl is used to induce an outward electric field because the chloride ion (D_{Cl^-} = 2.032 × 10^{-9} $\mathrm{m^2/s}$) is higher in diffusivity than the sodium ion (D_{Na+} = 1.334 × 10^{-9} $\mathrm{m^2/s}$), *i.e.*, $\beta_{NaCl} = -0.207$. For the negatively charged particles, both CP and EP act toward the target chamber, which results in an accumulation of particles.

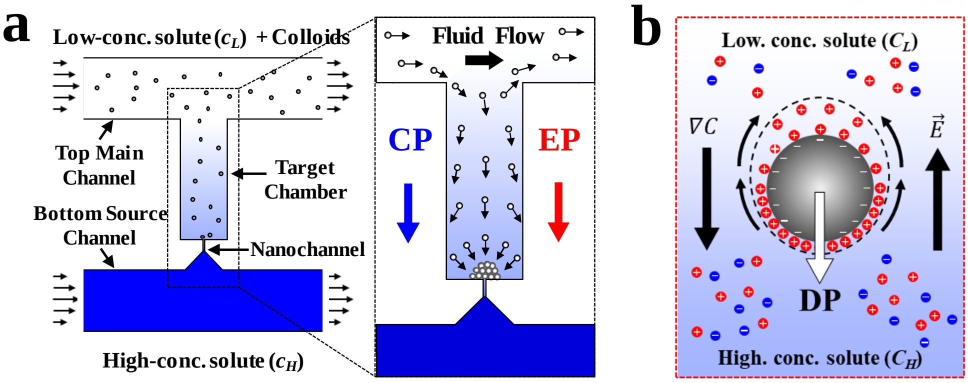

Figure 3-3. Schematic of the diffusiophoresis-based motion of negatively charged particles (1-μm carboxylated polystyrene) in the presence of the concentration gradient of NaCl in the target chamber. (a) Configuration of the MNDP for accumulation of negatively charged particles in the presence of NaCl gradient. (b) The motion of the negatively charged particles induced by osmotic pressure inside of the EDL due to the asymmetric adsorption of counter ions (CP: chemiphoresis) and the imposed electric field due to the diffusivity difference between cations and anions (EP: electrophoresis).

Fig. 3-4(a) demonstrates the diffusiophoretic transport of negatively charged particles (carboxylated polystyrene with particle diameter d_p = 1 μm and zeta potential ζ_p = −50 mV) and their enrichment at the nanochannel entrance in the presence of the NaCl concentration gradient. The particle accumulation process continues for 2 h, and the migration speed of the particles appears to remain nearly constant over time. Even for shorter chambers, the colloidal particles continuously build up outside the chamber defeating shear stress induced by the PDF in the main channel. Using the same MNDP, the accumulation rate of the particles can be controlled by employing a different solution, such as KCl. Fig. 3-4(b) shows the migration of the colloidal particles in the presence of the KCl gradient (*i.e.*, C_L = 10 μM and C_H = 1 M).

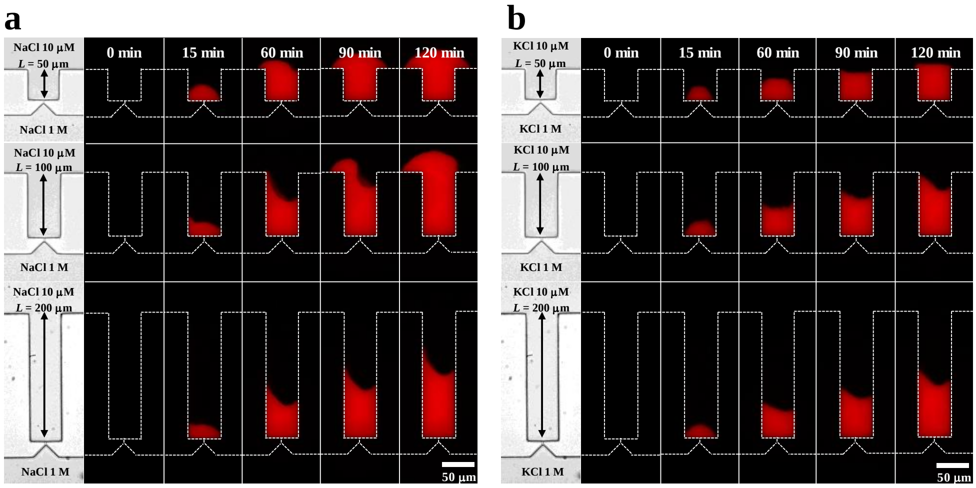

Figure 3-4. Sequential fluorescence images of diffusiophoresis-based concentrations of colloidal particles with various length of target chamber (e.g., 50, 100, 200 μm) for 2 h in the presence of (a) NaCl concentration gradient (C_L = 10 μM and C_H = 1 M) and (b) KCl concentration gradient (C_L = 10 μM and C_H = 1 M), respectively.

Because the diffusivity of potassium ions (D_{K+} = 1.957 × 10^{-9} m^2/s) is similar to that of chloride ions (D_{Cl^-} = 2.032 × 10^{-9} m^2/s), the concentration gradient of KCl produces a relatively weak electric field compared to that of NaCl (*i.e.*, $\beta_{KCl} = -0.019$ vs. $\beta_{NaCl} = -0.207$), which results in the relatively low diffusiophoretic mobility, as shown in Fig. 3-5(a). Therefore, fewer particles are accumulated because the EP contribution is weaker than that when using the NaCl concentration gradient. In addition, the diffusiophoretic force in the KCL concentration gradient is not strong enough to defeat the shear stress induced by the PDF, so that the colloidal particles are no longer accumulated outside the chamber. Fig. 3-5(b) shows that the number density of the particles in the target chamber increases linearly over time in the presence of concentration gradients of both NaCl and KCl. We analyzed the concentration factors of the particles by measuring their fluorescence intensities in the target chamber; the intensities were assumed to be proportional to the particle number densities. Because we introduced a low volume fraction of colloids (0.05%, d_p = 1 μm) in the experiment, 50 particles were left initially in the target chamber, and the focusing rate was approximately 5 particles/s. This yielded concentration factors of 400-fold in NaCl and 330-fold in KCl after 2 h, as calculated from the volume fraction, *i.e.*, the total volume filled with the particles relative to the target chamber volume (~10^5 μm^3) was converted to the number density of the particles. Although the nanopores among the accumulated particles, through which ions pass, become longer and narrower over time, the MNDP maintains the concentration factors, indicating that the MNDP facilitates the maintenance of the steady-state solute concentration gradient by simply flushing the fresh solutions into the two main channels. Therefore, the present mechanism can be exploited as a promising bio-sample concentrator for operation in a steady-state and long-term manner.

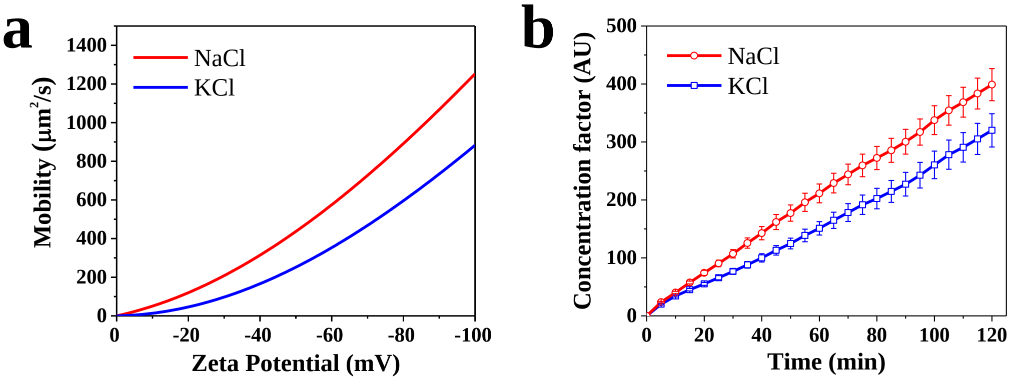

Figure 3-5. Diffusiophoretic mobility and factor for the concentration of the 1-μm carboxylated polystyrene in the MNDP. (a) Theoretical prediction of the size-independent diffusiophoretic mobility in the presence of concentration gradient of NaCl and KCl. (b) The concentration factors of the colloidal particles in the 200 μm of target chamber are quantified using the fluorescence intensities from the NaCl and KCl experiments, respectively.

We also conducted numerical simulations by employing theoretical models from the literature [87, 100] to acquire insight about the accumulation and extraction mechanisms of particles in the MNDP. Fig. 3-6(a) shows the domain for 3D and time-dependent numerical simulations for particle tracing. The particle trace under the fluid advection and solute gradient is solved with the calculated mobility of diffusioosmosis (Γ_w) and diffusiophoresis (Γ_p). The continuity between the diffusioosmotic flow and the pressure-driven flow in the target chamber causes circulating flows that push the particles towards the side wall, as observed in previous studies [87, 100]. This is because the target chamber functions as a dead end because of the high hydraulic resistance of the nanochannel. As the particles approach the side wall, they are forced to migrate back to the top main channel by the diffusioosmotic flow near the wall. However, most particles are drawn toward the nanochannel because diffusiophoresis dominates the other phenomena, as is repeatedly confirmed in the cross-sectional view of the simulation result, as shown in Fig. 3-6(b).

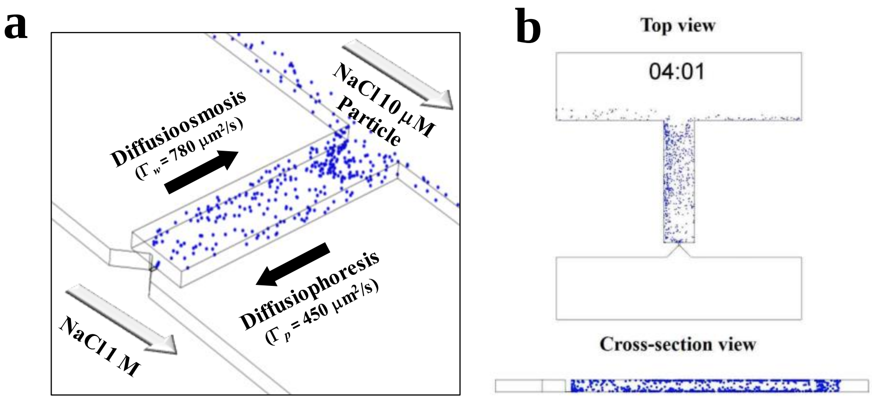

Figure 3-6. Theoretical modeling and numerical simulation results of the diffusiophoresis in the NaCl gradient (C_L = 10 μM and C_H = 1 M). (a) Nnumerical simulation results with calculated mobility of diffusiophoresis and diffusioosmosis show good agreement with the experimental ones. (b) Top view and cross-section view of simulation results show the colloidal particles going outside due to the diffusioosmosis.

Fig. 3-7(a) shows the mechanism of the extraction of the preconcentrated colloidal particles with negative charges. The preconcentrated particles are simply extracted by controlling the direction of the diffusiophoresis, which is conducted by changing the physicochemical environment in the target chamber. At first, pure water is loaded into the top main channel to make channel clean by washing away redundant particles. Then, K-acetate is loaded into the bottom main channel to produce diffusiophoresis in opposite direction. This occurs because potassium ions (D_{K+} = 1.957 × 10^{-9} m²/s) are faster than acetate ions ($D_{Acetate-}$ = 1.089 × 10^{-9} m²/s). This ionic condition produces an inward electric field ($\beta_{K\text{-}acetate}$ = 0.285), thereby causing negatively charged particles to move outward by strong EP. Although the CP direction remains inward because the solute concentration remains similar, EP is dominant to change the net direction of diffusiophoresis during the transient state due to ionic interdiffusion between NaCl and K-acetate, thus reinforcing the imposed electric field.[87] However, the influence of ionic interdiffusion vanishes soon, and the new concentration gradient is generated, the competition between EP and CP decides the net direction of diffusiophoresis in the steady state. Here, the diffusioosmotic flow affects the net direction of the colloidal particles by producing circulation near the corner of the target chamber.

Fig. 3-7(b) shows results of the extraction of the preconcentrated colloidal particles by changing NaCl solution with K-acetate solution in the bottom main channel. We previously accumulated 1-μm carboxylated polystyrene for 2 h in the presence of the NaCl concentration gradient. Then, we changed the NaCl solution with a K-acetate solution (C_L = 0 M and C_H = 1 M) to reverse the net direction of the diffusiophoresis. Most colloidal particles are extracted within 5 min due to the EP-dominated environment during the transient state. In the steady state, however, the particles that escaped collection return to the target chamber and become trapped in the corners, because diffusiophoresis is comparable to the advection flow induced by diffusioosmosis near the wall. Thus, the colloidal particles become entrapped, forming circulating flows near the corners, as mentioned above. To extract particles completely, the net diffusiophoretic mobility should be larger than the diffusioosmotic mobility in the steady state; these mobilities can be controlled by supplement of a surfactant. Fig. 3-7(c) shows the extraction of preconcentrated colloidal particles under the same electrolytes with the addition of Pluronic F-127 (0.02 w/v%). In this case, during the first 5 min, many of the preconcentrated particles are extracted, similar to previous results without surfactant. However, particles are constantly extracted even in the steady-state concentration gradient. This is because EP remains dominant in the steady state compared to CP and diffusioosmosis.

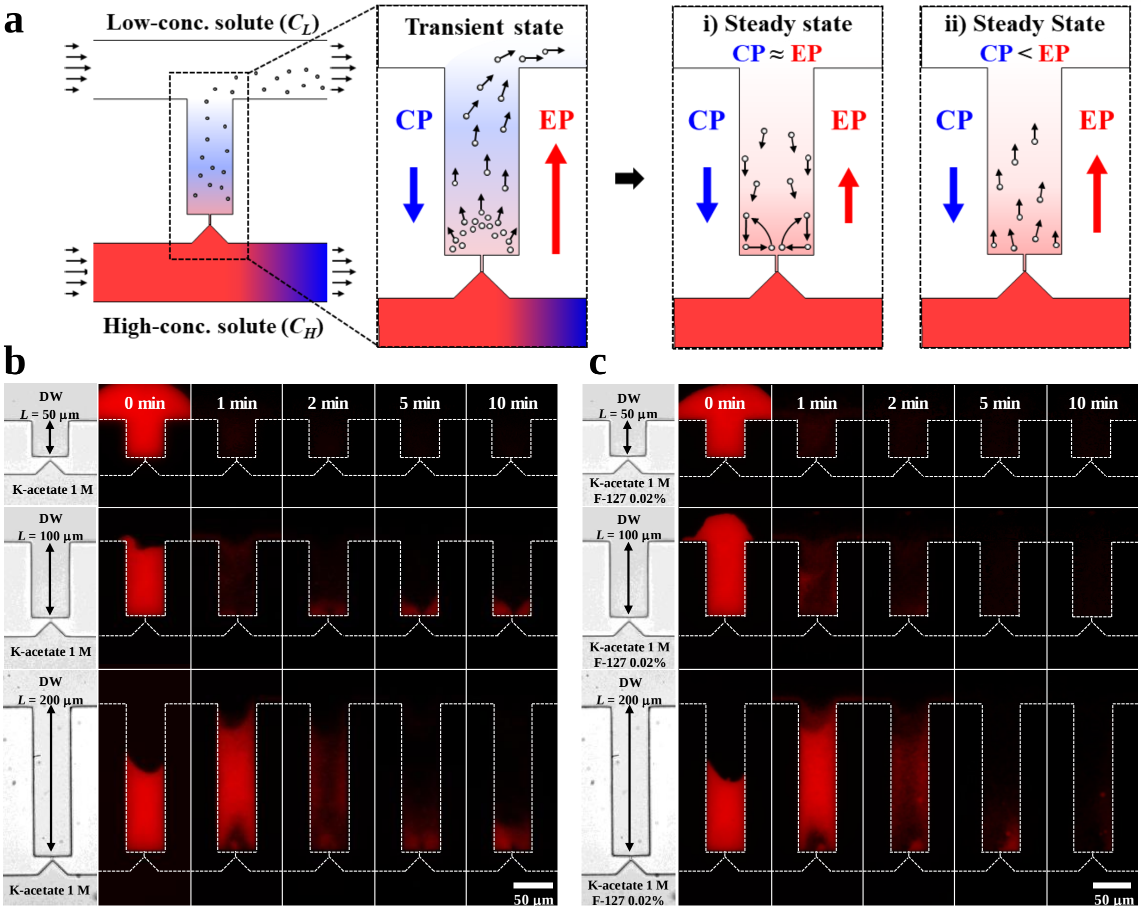

Figure 3-7. Simple and on-demand extraction of the preconcentrated colloidal particles. (a) Schematic of two different aspects of extraction between the transient state and steady state of buffer change (CP: chemiphoresis; EP: electrophoresis). (b)-(c) Time-lapse images of the diffusiophoresis-based extraction of the preconcentrated colloidal particles for 10 min in the presence of the concentration gradient of pure K-acetate solution (C_L = 0 M and C_H = 1 M) and K-acetate solution (C_L = 0 M and C_H = 1 M) containing 0.02% Pluronic F-127, respectively.

Fig. 3-8(a) shows a comparison of the extraction performance *via* the fluorescence intensities of the preconcentrated particles in the 200 μm of target chamber over time. We measure the net fluorescence intensities (FI) after preconcentration is completed (*i.e.*, $\mathrm{FI_{net}}$) and then quantify the FI of the remaining particles ($\mathrm{FI_R}$) in the target chamber; the extraction ratio is calculated as $1 - \mathrm{FI_R}/\mathrm{FI_{net}}$. For pure K-acetate solution, the extraction ratio maintains after 4 min. However, for K-acetate solution with the surfactant, the extraction ratio is increased from 85% to 95% and continues to increase until 15 min elapse. As characterized by Fig. 3-2(c), the transient state persists for approximately 4 min, during which the surfactant does not affect the extraction ratio. However, after the transient state, the extraction ratio is improved only for the case with surfactant in the solution. This is because the net diffusiophoretic mobility is changed by surfactant addition.

Fig. 3-8(b) shows the analytical result of the diffusiophoretic mobility, which depends on the zeta potential of the particles and can be affected by surfactant addition. Typically, non-ionic surfactants can reduce the zeta potential of colloidal particles by adsorption, which shifts the shear plane away from the colloidal particle surfaces [101, 102] and thereby changes their diffusiophoretic mobility. As the zeta potential varies, the electrophoretic mobility changes linearly (red line), while the chemiphoretic mobility changes nonlinearly (blue line). Therefore, the net diffusiophoretic mobility changes from −40 μm^2/s to −70 μm^2/s as the zeta potential decreases from −53.5 mV (*i.e.*, for the pure K-acetate solution) to −17.3 mV (*i.e.*, for the K-acetate solution with 0.02% Pluronic F-127), as shown in Table 3-1.

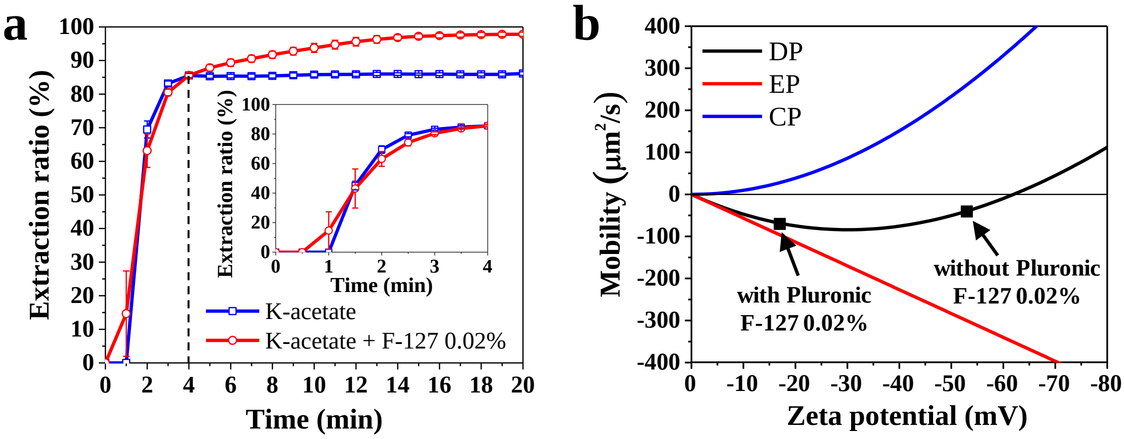

Figure 3-8. Diffusiophoretic mobility and ratio for the extraction of the 1-μm carboxylated polystyrene in the MNDP. (a) The extraction ratio of the preconcentrated colloidal particles using the pure K-acetate equilibrates at 85% efficiency after 4 min. However, for the K-acetate mixed with Pluronic F-127, the efficiency exceeds 95% after 10 min. (b) Analytical results show that the individual contributions of EP and CP to the diffusiophoretic mobility of the colloidal particles in the presence of the concentration gradient of K-acetate solution can significantly change with the addition of Pluronic F-127 because of the decrease of the zeta potential from $\zeta_p = -53.5$ mV to $\zeta_p = -17.3$ mV.

Table 3-1. Zeta potentials of colloidal particles with various solution conditions, as measured by electrophoretic light scattering in this work.

Particle	ζ_p (mV)	Solution conditions[1]
Carboxylated polystyrene	−50.5 ± 8.6	NaCl
	−51.2 ± 10.0	KCl
	−53.5 ± 8.4	K-acetate
	−17.3 ± 5.5	K-acetate, 0.02% Pluronic F-127

[1] The solution concentration is 10 mM and pH is approximately 7.0.

Because the motion of the particles near the wall is determined by the diffusiophoresis and diffusioosmosis, we can predict the direction of the particles near the corners depending on the diffusioosmotic mobility of the PDMS wall. However, the zeta potential of the PDMS wall and the resulting diffusioosmotic mobility in the presence of the non-ionic surfactant are not yet well known because of the poor repeatability of experimental measurements. Thus, we conducted time-dependent 3D numerical simulations to confirm the extraction mechanism depending on the mobility difference between diffusiophoresis and diffusioosmosis by varying the zeta potential of the PDMS wall, as shown in Fig. 3-9. As expected, compared to the diffusiophoretic mobility, a relatively strong diffusioosmotic flow entraps preconcentrated particles near the corners of the target chamber (Fig. 3-9(a)), while a relatively weak diffusioosmotic flow does not influence the extraction (Fig. 3-9(b)).

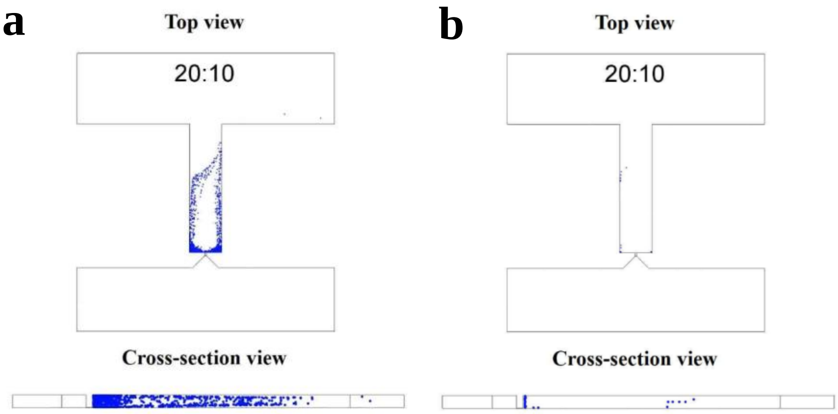

Figure 3-9. Top view and cross-section view of numerical simulation results of the diffusiophoresis in the presence of (a) pure K-acetate gradient (C_L = 0 M and C_H = 1 M) and (b) K-acetate (C_L = 0 M and C_H = 1 M) mixed with 0.02% Pluronic F-127, respectively.

The addition of surfactant facilitates not only the complete extraction of the preconcentrated particles but also the repeatable use of the MNDP. The reusability test of the MNDP is shown in Fig. 3-10. We utilized the same conditions for the preconcentration of the colloidal particles using the concentration gradient of NaCl for 1 h. After preconcentration, we changed the physicochemical environment to the same condition used for the full extraction of the preconcentrated colloidal particles using the concentration gradient of K-acetate containing 0.02% Pluronic F-127 for 15 min, as shown in Fig. 3-10(a). The above steps for concentration and extraction were performed in a single cycle that was repeated three times consecutively. Fig. 3-10(b) shows the extraction process in each cycle enables evacuation of the target chamber, leaving only a few colloidal particles that are non-specifically bound to the PDMS surface. From this result, we further confirmed that the MNDP can avoid clogging problems with the assistance of the surfactant.

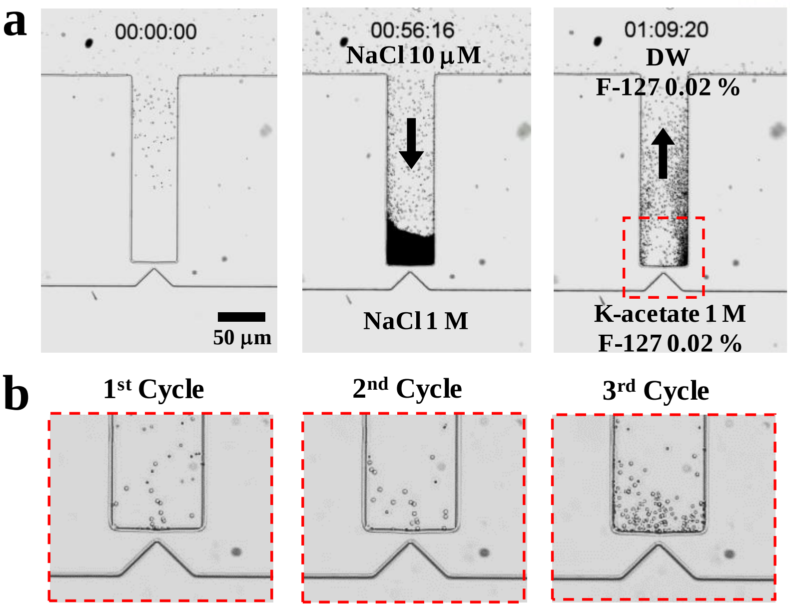

Figure 3-10. Reusability test of the MNDP for active transport control of colloidal particles. (a) Microscopic images show that the on-demand concentration and extraction of colloidal particles in the MNDP. (c) A few of non-specifically bound particles remained in the MNDP while repeating three cycles of concentration and extraction of the colloidal particles.

As a potential application, we demonstrated diffusiophoresis-based genetic induction assay to obtain genetically induced samples from the raw samples of synthetically engineered *E. coli* DH10B strain. First, we prepared bacteria (OD_{600} = 1) resuspended to the M9 minimal medium without any carbon source to prohibit the growth-based population. Then we produce the concentration gradient of NaCl by flushing the bacteria suspension into the top main channel and the M9 minmial medium including high concentration of NaCl (c_H = 2 M) into the bottom source channel continuously as shown in Fig. 3-11(a). Fluorescent intensities (GFP) from the bacteria in the target chamber was measured every 5 min and observed to increase gradually over time meaning the increase of population due to the concentration. Fig. 3-11(b) shows that the slope of fluorescent intensities was constant, indicating that the concentration factor is not affected by the preconcentrated bacteria in the target chamber. After the preconcentration of bacteria, we replaced the solution with fresh M9 medium including glucose and acyl-homoserine lactone (AHL) inducing genetic circuit to express fluorescence signal as shown in Fig. 3-11(c). As expected, the fluorescence intensities gradually increase over time after the adaptation period (~ 20 min) as shown in Fig. 3-11(d). This result demonstrate that the high concentration of NaCl for the preconcentration step is biocompatible so that the genetic circuit is well maintained. Fig. 3-11(e) shows that the genetically induced bacteria in the target chamber can be extracted by replacing the solution with M9 minimal medium producing the concentration gradient of K-acetate (c_H = 100 mM). Fig. 3-11(f) shows that the 95 % of genetically induced bacteria were completely extracted within 10 min inferred from the fluorescence intensities. This genetic induction assay demonstrates the advantage of the MNDP to facilitate biological assay obtaining genetically induced samples from the raw sample on a single chip only with electrolyte solution.

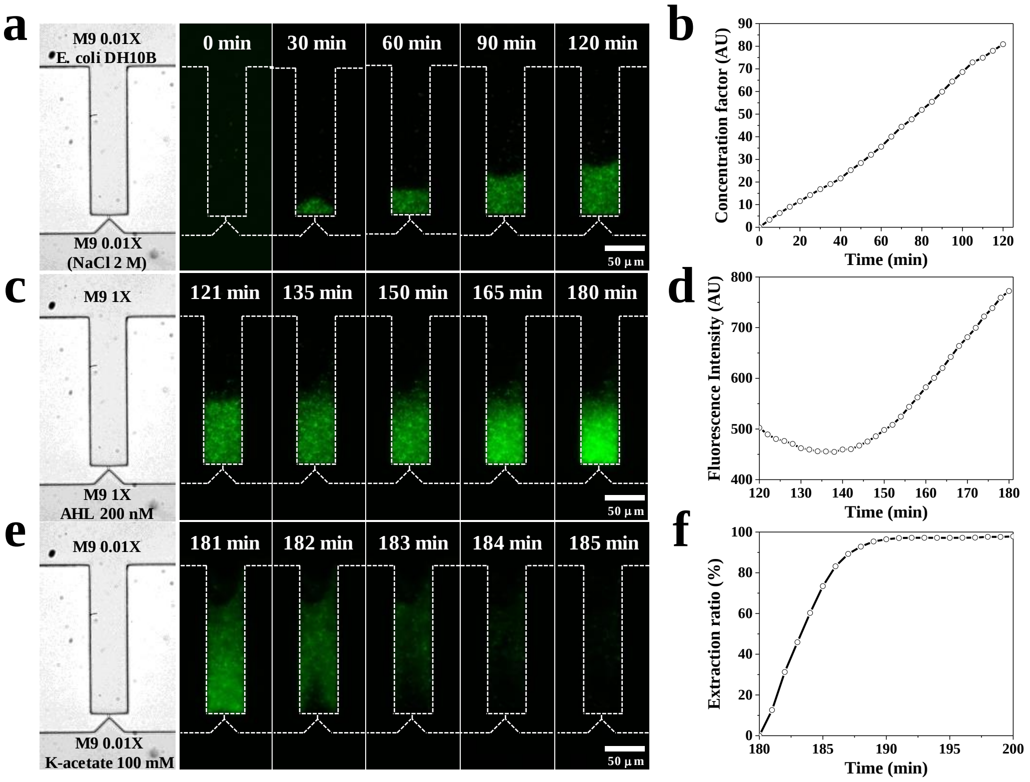

Figure 3-11. Diffusiophoresis-based genetic induction assay with raw sample of synthetically engineered *Escherichia coli* DH10B from the preconcentration to the extraction on a single chip. (a) Preconcentration of raw samples in the presence of concentration gradient of NaCl. (b) Quantification results of the fluorescence intensity shows the concentration factor over 2 h. (c) Genetic induction of the preconcentrated samples by signaling molecules, AHL, transported by nanochannel. (d) Quantification results of the fluorescence intensity shows quantitative gene expression over 1 h. (e) Extraction of the samples in the presence of concentration gradient of K-acetate. (f) Quantification results of the fluorescence intensity shows extraction ratio over 5 min.

3.4 Conclusion

We have demonstrated that the proposed MNDP allows simple manipulation of physiochemical environments and facilitates stable and long-term diffusiophoresis-based manipulation of colloidal particles on a chip. We optimized both cracking-assisted photolithography and modified-soft-lithography to easily fabricate a nanochannel-integrated PDMS-based micro/nanofluidic platform in which the nanochannel functions as a porous membrane for the delicate diffusion control of solutes. This membrane-free device allows long-term control of the solute gradient without requiring pressure control. Moreover, we demonstrated the loading and flushing of solutions to dynamically generate and modify the physicochemical environment in the target chamber, which causes the active manipulation of the diffusiophoresis-based transport of various colloidal particles. We also demonstrated that the MNDP can be used as a multi-functional device for colloidal particles, showing remarkable potential for processing bio-samples in a reusable manner. The same mechanism and platform can be used for the concentration, and extraction of various bio-samples based on sample features such as particle size and electrical charge density. Hence, the presented MNDP can be exploited as a portable, self-containable on-site μTAS that relies only on the chemical energies of solutions loaded into and flushed from the platform using a pipette. We therefore anticipate that the demonstrated microfabrication process for the MNDP and the manipulation technique for colloidal particles may broaden the applicability of μTASs, including in labs-on-a-chip, bio-chips, and other microfluidic systems.

Chapter 4. Micro/Nanofluidic Diffusiophoresis Platform for Nanoparticle Separation

4.1 Introduction

In previous chapter, we demonstrated that transport control of colloidal particles using solute gradient. This technique facilitates on-demand concentration and extraction of the colloidal particles including bacteria that shows potential application of versatile µTASs on a single chip with minimal resources such as electrolytes and pipette. However, it is still necessary to explore the DP mechanism for transport control of nanoparticles, which is one of the most interesting research area due to versatile size-dependent properties of it. The DP-based transport shows a strong size effect when their size is comparable to the electrical double layer (EDL) thickness.[87, 94] In particular, the size effect can determine not only the magnitude but also the direction of mobility with individual control of CP and EP of colloidal particles due to the nonlinear relationship between CP and EP. Therefore, DP has a big potential to facilitate the separation of colloidal particles by size, which is the most challenging issues to control the nanoparticles.

Recall that the DP is composed of EP and CP induced by the concentration gradient of solutes near the surface of colloidal particles. The first and second terms in equation (12) refer to electrophoretic mobility (Γ_{EP}) and chemiphoretic mobility (Γ_{CP}), respectively. Here, CP always migrates the particles toward the higher concentration while the resulting direction of EP is determined by the signs of ζ_p and β.[87] In addition, the size effect cannot be neglected any longer as particle radius a approaches the magnitude of EDL thickness (i.e., $\kappa^{-1} = \sqrt{\varepsilon k_B T/2N_a e^2 c}$, where N_a is the Avogadro number).[99] In fact, Prieve et al. reported that EDL thickness (i.e., $\kappa a \sim 1$) affects both the EP and CP of particles when it is not negligible. They also suggested that the size-dependent Γ_{EP} and Γ_{CP} could be theoretically expressed as a regular power-series expansion of the nondimensionalized parameter $\lambda = (\kappa a)^{-1}$, and they are respectively given as[94]

$$\Gamma_{EP} = \frac{\varepsilon}{\eta}\left(\frac{k_B T}{ze}\right)^2 \left\{\beta\bar{\zeta}_p + \lambda\left[F_1 + Pe(\beta F_4 + F_5)\right] + O(\lambda^2)\right\} \tag{13}$$

$$\Gamma_{CP} = 4\frac{\varepsilon}{\eta}\left(\frac{k_B T}{ze}\right)^2 \left\{\ln\cosh\bar{\zeta}_p + \lambda\left[F_0 + Pe(F_2 + \beta F_3)\right] + O(\lambda^2)\right\}, \tag{14}$$

where $\bar{\zeta}_p = ze\zeta_p/4k_BT$ and F_n is the coefficient numerically calculated in previous studies.[94] The Péclet number (Pe) of solutes is estimated to be $v_p a/D_s \approx 0.1$, where D_s is the solute diffusivity. The

$O(\lambda^2)$ terms in equations (2) and (3) can be neglected with a low-order Padé approximant; thus, the final forms of the size-dependent Γ_{EP} and Γ_{CP} are expressed as

$$\Gamma_{EP} = \frac{\varepsilon}{\eta}\left(\frac{k_B T}{ze}\right)^2 \beta\bar{\zeta}_p \left[1-\lambda\left\{\frac{F_1 + Pe(\beta F_4 + F_5)}{2\bar{\zeta}_p}\right\}\right]^{-1} \tag{15}$$

$$\Gamma_{CP} = 4\frac{\varepsilon}{\eta}\left(\frac{k_B T}{ze}\right)^2 \ln\cosh\bar{\zeta}_p \left[1-\lambda\left\{\frac{F_0 + Pe(F_2 + \beta F_3)}{8\ln\cosh\bar{\zeta}_p}\right\}\right]^{-1}. \tag{16}$$

Again, for microparticles, given that the second terms in equations (15) and (16) are considered negligible (i.e., λ tends to zero as κa tends to ∞), Γ_{EP} and Γ_{CP} take on the same forms as the first and second terms, respectively, in the size-independent Γ_p, as shown in equation (12). However, for nanoparticles, the size of which is comparable to EDL thickness, these terms become influential so that the net $\Gamma_p = \Gamma_{EP} + \Gamma_{CP}$ can significantly change with the size of particles (i.e., κa is finite). In this work, we supported the theory through experiments employing the MNDP and showed a repeatable, reversible, and active transport control for submicron particles on a chip. In particular, we demonstrated not only separation but also fractionation of particle mixture using an individual control of CP and EP when the direction of CP and EP is reversed.

4.2 Experimental setup

Sample preparation and handling: Polystyrene particles with diameters of 200-nm and 620-nm were mixed with a 1:1 ratio to form the final concentration of 0.05 w/v% to demonstrate the separation of nanoparticle mixure. First of all, nanoparticle mixture is accumulated in the concentration gradient of NaCl for 30 min. After sample enrichment, the particle solution was changed to pure distilled water. Subsequently, the high-concentration of NaCl in the source channel was changed to high-concentration of K-acetate and Na-acetate for separation and fractionation, respectively. Particles were treated with sonication for 30 min before use. All solutions were handled with a pipette to maintain flow rates during the desired working time.

4.3 Results and discussion

To demonstrate size-dependent separation of colloidal particles, we exploited same design of the MNDP introduced in the previous chapter. Then, we prepared a submicron particle mixture with same material, polystyrene, which is composed of 200 and 620-nm particles and fluorescently labeled using Rhodamine-B (red) and DAPI (blue), respectively, to minimize the effect of difference in zeta potential on the separation. We obtained zeta potential of particles from the measured electrophoretic mobility considering the Henry's function dealing with the retardation effect, when the particle radius a is comparable to EDL thickness κ^{-1} ($\kappa a \gg 10$) described in the previous study.[100] The difference in zeta potential between 200-nm ($\zeta_p \approx -70$ mV) and 620-nm ($\zeta_p \approx -73$ mV) particles considering size effect is less than 3 mV as shown in Table 4-1. The submicron particle mixture was highly concentrated near the nanochannel entrance for 30 min by using a concentration gradient of NaCl (c_L = 10 μM and c_H = 1 M) in the MNDP as shown in Fig. 4-1.

Table 4-1. Zeta potentials of colloidal particles adjusted by Henry's function for various-solution conditions measured through electrophoretic light scattering.

Particle	*ELS*, ζ_p (mV)	f^1	ζ_p (mV)	Solution Condition^2
200 nm, Polystyrene	−60.2 ± 7.8	0.828	−72.7 ± 6.3	NaCl
	−58.8 ± 7.9	0.836	−70.3 ± 6.6	K-acetate
	−58.4 ± 7.2	0.837	−69.8 ± 6.0	Na-acetate
620 nm, Polystyrene	−68.6 ± 5.9	0.926	−74.1 ± 5.4	NaCl
	−67.8 ± 5.2	0.928	−73.1 ± 4.9	K-acetate
	−67.0 ± 5.4	0.929	−72.2 ± 5.0	Na-acetate

[1] Henry's function is negligible (f =1) for 1 μm particles.

[2] The concentration and pH of the solution are 10 mM and 7.0, respectively.

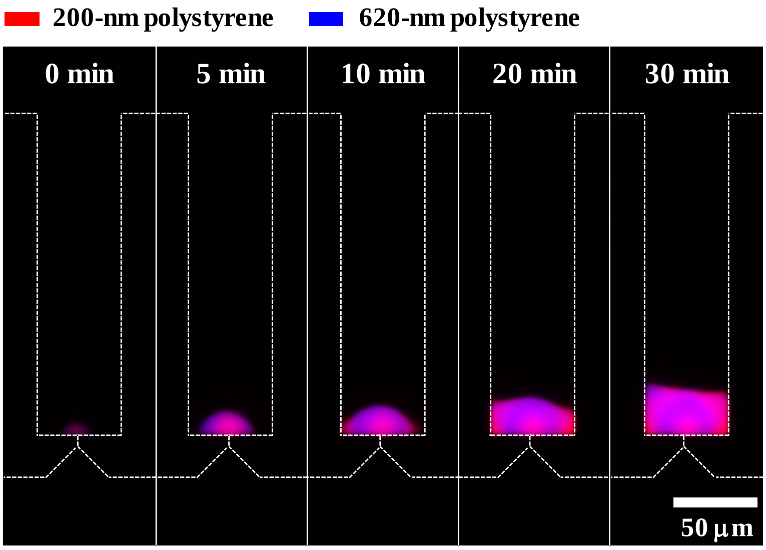

Figure 4-1. Sequential fluorescence images of the DP-based concentration of a nanoparticle mixture composed of red fluorescent 200-nm and blue fluorescent polystyrene particles in the presence of the NaCl concentration gradient (c_L = 10 μM and c_H = 1 M) for 30 min.

Prior to buffer change for the separation, we confirmed that self-diffusion induced by Brownian motion allows for both particles to migrate toward lower concentration in the absence of concentration gradient of solutes (NaCl, c_L = c_H = 10 mM), but the particles are not separated as shown in Fig. 4-2. The particle band widens and fades over time. Because there is little difference in diffusion coefficient according to Stokes-Einstein relation ($D_p = k_BT/6\pi\eta a$) between two particles (i.e., D_p = 2.45 μm^2/s for 200-nm and D_p = 0.79 μm^2/s for 620-nm).

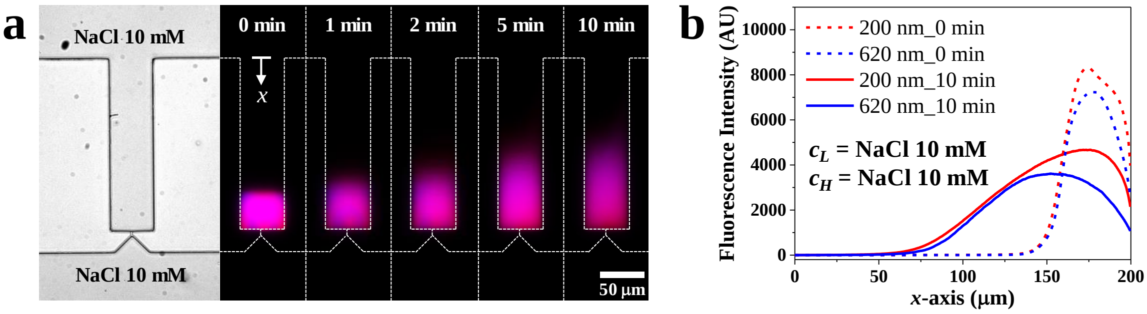

Figure 4-2. The effect of Brownian motion on the particle transport. (a) Sequential fluorescence images of the self-diffusion of the preconcentrated particles for 10 min in the absence of concentration gradient (NaCl, c_L = c_H = 10 mM). (b) Distribution of particles at 0 min (dotted line) and 10 min (solid line) along the microchamber.

Then, we tested three extraction conditions by using K-acetate, Na-acetate, and a mixture of these two solutions sequentially. First, we employed a concentration gradient of K-acetate (c_L = 0 M and c_H = 1 M), as shown in Fig. 4-3(a). Both particle types preconcentrated in advance are extracted mostly for the transient state (*i.e.*, <5 min), in which an interdiffusional phenomenon is induced and dominant, and the 200-nm particles move faster and farther than the 620-nm particles. However, for the steady state (*i.e.*, >5 min) in which the other concentration gradient is newly established, some of the 620-nm particles that have migrated away from the nanochannel junction return to the target chamber and become entrapped again. This is because the diffusioosmotic flow, which is fully developed for the transient state and becomes dominant during the steady state, affects the net mobility of the particles. In other words, the diffusioosmotic flow causes the remaining particles in the target chamber to flow toward the nanochannel junction again, thus inducing the circulating motion of some particles in the target chamber. As a result, the 200-nm particles are completely extracted while most of the 620-nm particles are entrapped in the target chamber, demonstrating the partial separation of submicron particles according to size.

Second, Fig. 4-3(b) shows the fractionation of particles with the concentration gradient of Na-acetate (c_L = 0 M and c_H = 1 M), which generates a relatively weak electric field compared to that of K-acetate because of the low diffusivity difference between ions (i.e., $\beta_{Na\text{-}acetate}$ = 0.101). For the transient state (*i.e.*, <5 min), both particle types are extracted from the nanochannel junction in a similar manner to that shown in Fig. 4-3(a). However, the separation span seems narrower than that in the previous experiment (Fig. 4-3(a)) approximately 2 min after the solution is switched. For the steady state (*i.e.*,

>5 min), the 200-nm particles, which have migrated farther during the transient state, are forced to slowly return to the nanochannel junction. As the 620-nm particles form a close-packed structure, which have a theoretical pore size of 93 nm (*i.e.*, approximately 15% of the particle diameter),[103] they may prevent small particles from penetrating through the pores, thereby resulting in size-based particle fractionation.

Third, we demonstrate a more successful size-dependent extraction and separation of a particle mixture using a mixed solution comprising Na-acetate (c_L = 0 M and c_H = 800 mM) and K-acetate (c_L = 0 M and c_H = 200 mM). The imposed electric field of K-acetate is too strong and that of Na-acetate is too weak to separate the particle mixture. Therefore, we can easily estimate that the mixed solution of K- and Na-acetates is appropriate for the selective separation of smaller particles from the particle mixture. As shown in Fig. 4-3(c), all the 200-nm particles are completely extracted, while almost all the 620-nm particles are left in the target chamber by actively switching the concentration gradient, thereby demonstrating a dynamic transport control of colloidal particles on a chip.

In addition, we calculated separation efficiency with removal rate and recovery rate using remained particles in the target chamber for all cases of environmental change as shown in Fig. 4-3(d-f). For 200-nm particles, most particles were removed from the target chamber with removal rates of 96% and 92% for K-acetate and a mixture of K-acetate and Na-acetate, respectively. On the other hand, 620-nm particles were recovered in the target chamber with recovery rates of 57% and 94% for K-acetate and the mixture of K-acetate and Na-acetate, respectively. In the presence of concentration gradient of Na-acetate, both particles were fractionated without leaving the target chamber.

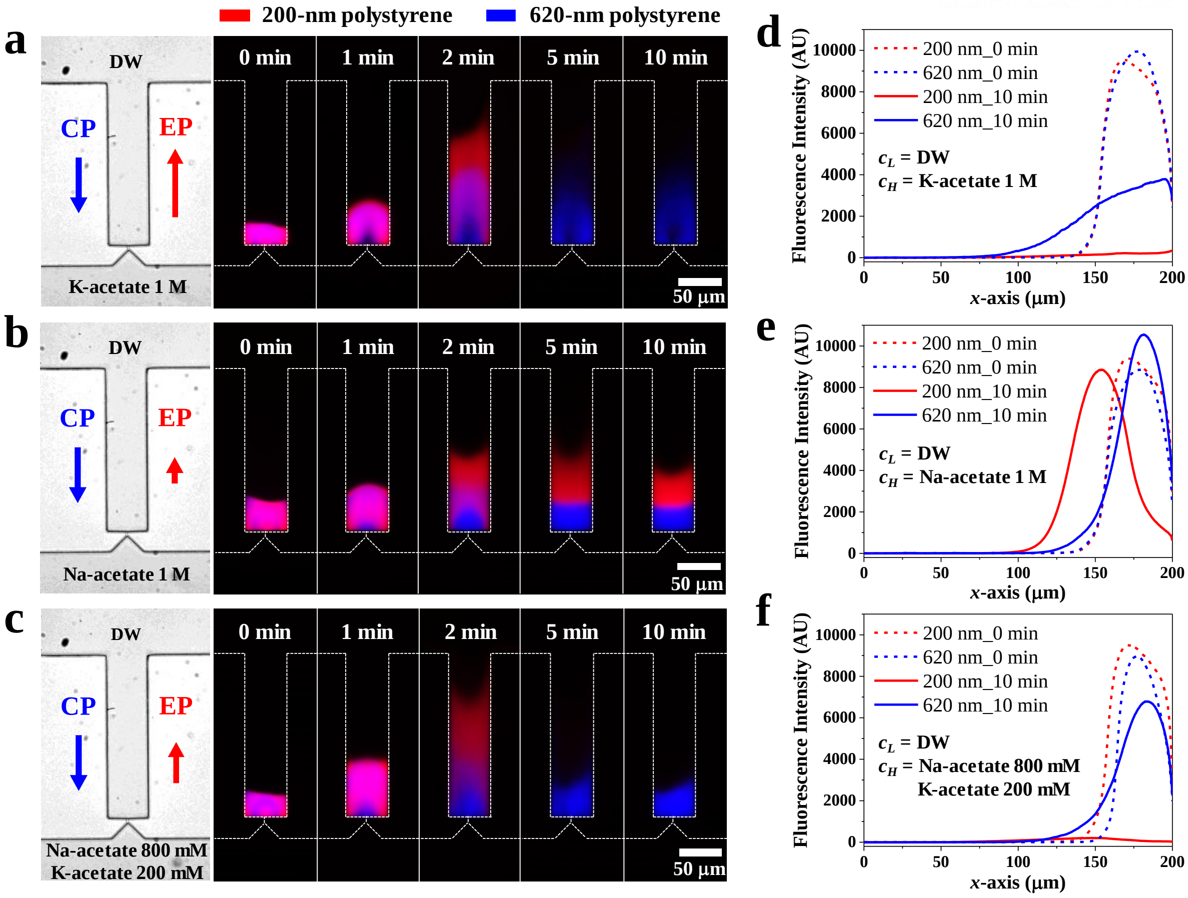

Figure 4-3. Control of a submicron particle mixture composed of red fluorescent 200-nm and blue fluorescent 620-nm polystyrene particles. (**a**) The preconcentrated particle mixture is separated in the presence of a K-acetate concentration gradient (c_L = 0 M and c_H = 1 M) that produces relatively strong EP compared to CP. (**b**) The preconcentrated particle mixture is fractionated by size in the presence of the Na-acetate concentration gradient (c_L = 0 M and c_H = 1 M) that produces relatively weak electrophoresis. (**c**) A mixture of Na-acetate (c_L = 0 M and c_H = 800 mM) and K-acetate (c_L = 0 M and c_H = 200 mM) is employed for the separation by selectively extracting only the 200-nm particles for the transient state and then trapping the 620-nm particles in the target chamber during the steady state. (d-f) Distribution of particles at 0 min (dotted line) and 10 min (solid line) in each results of (a-c), respectively.

It is still interesting that the smaller particles (i.e., 200-nm) always move faster and farther than the larger particles (i.e., 620-nm) for all the transient periods (i.e., $t < 5$ min). These transient extraction processes seem to be contradictory to the tendency of other phoresis mechanisms in which the migration speed (i.e., phoretic mobility) decreases with the particle size because of the scaling law.[57, 71, 84, 104] As mentioned earlier, the classical theory of size-independent DP can be explained only with the ζ_p of particles and the β of solutions, as plotted in Fig. 4-4(a). However, for the particles with similar zeta potential, the theory in turn fails in explaining the fast migration of the smaller particles compared to that of the larger ones. For this reason, we utilized the size-dependent Γ_{EP} and Γ_{CP} of particles to consider the size effect. Subsequently, the Γ_{EP} and Γ_{CP} of the particles could be calculated using equations (4) and (5), and then compared with the experimental results in the same sequential order, as shown in Fig 4-3. However, the significant modification of the net Γ_p of particles by the manipulation of the β and ζ_p values is of great importance. We note that various β values can easily be obtained by mixing two solutions with a fixed β value in different mixing ratios as formulated in Fig. 4-4(a) (inset), and the ζ_p of colloidal particles, potentially including bio-samples, can be manipulated by using specific molecules, such as surfactants, as demonstrated earlier.

Fig. 4-4(b) shows the size-dependent Γ_p with respect to λ for various ζ_p values in the steady state. In the presence of the concentration gradient of K-acetate ($\beta_{K\text{-}acetate}$ = 0.285), by assuming κ^{-1} = 3 nm for c = 10 mM and considering the size effect, we determined that the net Γ_p has negative values for the 200-nm particles (e.g., for $\kappa a \approx 33$) while the net Γ_p has positive values for the 620-nm particles (e.g., for $\kappa a \approx 103$). This result indicates that the 200-nm particles migrate toward the low concentration and the 620-nm particles circulate due to the diffusioosmotic flow in the steady state. This is attributed to the fact that the relative contribution of EP is more significant than that of CP as the particle size decreases (i.e., when $(\kappa a)^{-1} < 0.1$). In other words, the magnitude of the Γ_p of the 200-nm particles toward the low concentration is greater than that of the 620-nm particles owing to the relatively large contribution of the EP; the suppression of CP is larger than that of EP. This theoretical model and description show a good agreement with the experimental results shown in Fig. 4-3(a).

Fig. 4-4(c) shows the net Γ_p of the particles, calculated in the same manner, in the presence of the concentration gradient of Na-acetate ($\beta_{Na\text{-}acetate}$ = 0.101). In this case, the magnitude of the Γ_{CP} is much greater than that of the Γ_{EP} for both the 200- and 620-nm particles, resulting in their migration toward high concentration. As a result, the 620-nm particles return faster to the nanochannel than the 200-nm particles in the steady state. This also shows an excellent agreement with the experimental results shown in Fig. 4-3(b). The experimental result in Fig. 4-3(c) can also be explained in the same manner. As we optimized the strength of an induced electric field by mixing two solutions with different β values (i.e., the resulting β = 0.145), we could demonstrate that only the 200-nm particles are completely extracted while the 620-nm particles are left in the target chamber. To the best of our knowledge, this study is the first to report the empirical validation of the theoretical model to predict the size-dependent DP for particles in which the direction of CP and EP is reversed. Again, our experimental demonstration seems to be especially remarkable because intensive research efforts are being made for developing nanoparticle separation and fractionation techniques. This is attributed to the fact that the individual control of the magnitude and direction of CP and EP facilitates isolation of certain type of particles from the mixture depending on the size or zeta potential. Since it is possible to delicately adjust the magnitude and direction of net Γ_p by mixing two common electrolyte solutions, this suggested mechanism would be valid for most of submicron particles. Therefore, the MNDP obviously facilitates the selection of the separation and fractionation modes of various submicron particles according to the simple formulation of buffer solutions.

Fig. 4-4(d) comprehensively shows the theoretical prediction of the β-dependent Γ_P of submicron particles for various ζ_p values in the steady state, thereby providing a well-established and powerful guideline for submicron particle separation and fractionation. As the Γ_p is affected by the zeta potential, we can see that our technique is applicable to the separation of not only same-material particles with the same ζ_p but also same-sized particles with different ζ_p for submicron particles.

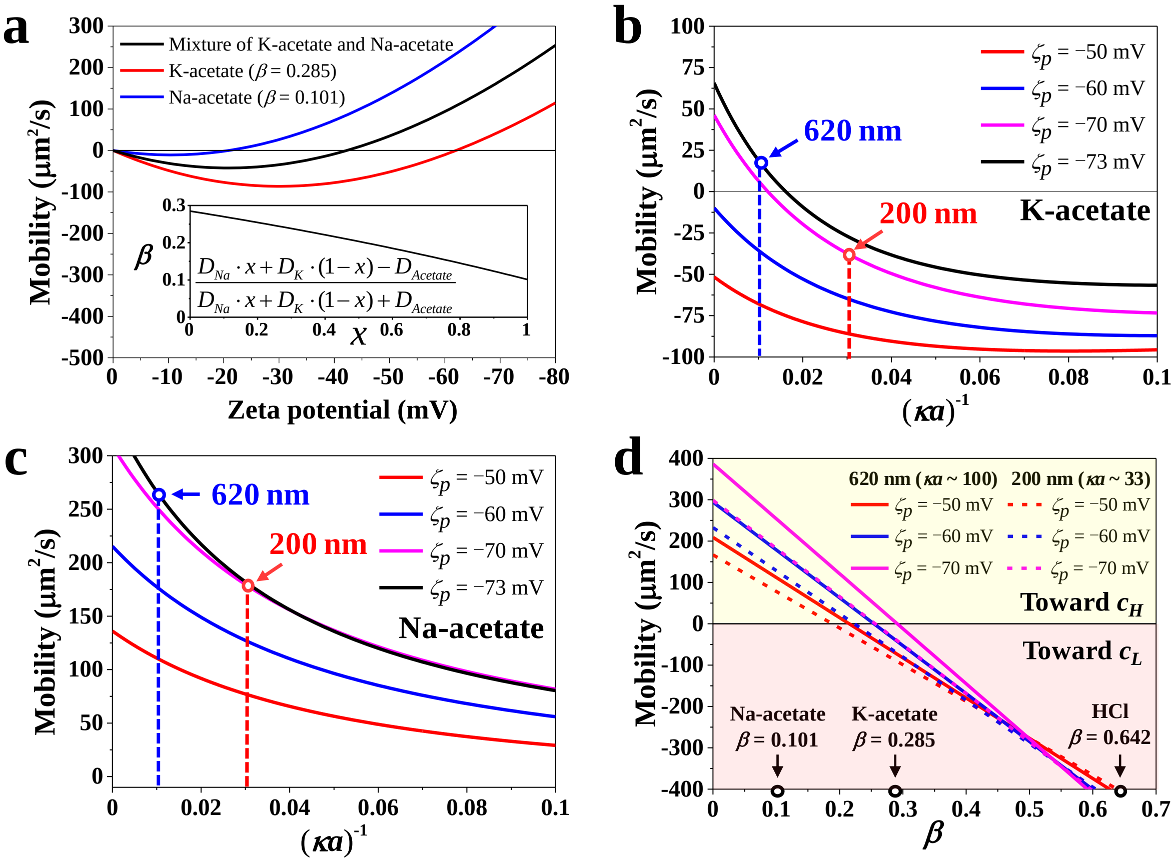

Figure 4-4. Theoretical analysis of the size-dependent fractionation and separation of the particle mixture. (**a**) Analytical results of the size-independent Γ_p of the submicron particles with a thin EDL ($\kappa a \rightarrow \infty$) in the presence of K-acetate, Na-acetate, and a mixture of K-acetate and Na-acetate solution, respectively. The inset indicates the β values that can be gained by mixing two solutions such Na-acetate and K-acetate in a different mixing ratio defined as $x = c_{Na\text{-}acetate}/(c_{Na\text{-}acetate} + c_{K\text{-}acetate})$. The size-dependent Γ_p of the particles in (**b**) K-acetate solution and (**c**) Na-acetate solution, respectively. (**d**) The Γ_p is calculated with the particle size, β of solutions, and ζ_p of particles.

To expand this separation mechanism to sub-100 nm particles, particle-particle interactions such as stability issue and self-diffusion of nanoparticles should be considered. First, the stability issue such as irreversible aggregation of colloidal particles is explained by DLVO theory dealing with the combined effect of van der Waals (vdW) interaction and electrostatic interaction.[105] van der Waals interaction energy (V_A) between unequal particles in water is introduced by H.C.Hamaker.

$$V_A = -\frac{A_{12}}{12}\left[\frac{y}{x^2+xy+x}+\frac{y}{x^2+xy+x+y}+2\ln\left(\frac{x^2+xy+x}{x^2+xy+x+y}\right)\right], \tag{17}$$

where A_{12} is Hamaker constant, $x = h/d_1$, $y = d_2/d_1$, h is the distance between two particles and d_1, d_2 are the diameters of two particles each. Hamaker constant of polystyrene sphere in water is suggested as $A_{12} = 0.95$.[105] For very short distance ($x \ll 1$), equation (17) reduces to

$$V_A = -\frac{A_{12}}{12h}\frac{d_1 d_2}{d_1+d_2} \tag{18}$$

For unequal two spheres, the EDL interaction energy (V_R) was introduced by Derjaguin method.

$$V_R = 2\pi\varepsilon\zeta_1\zeta_2\frac{d_1 d_2}{d_1+d_2}\exp(-\kappa h) \tag{19}$$

where ε is the permittivity of the medium, ζ_1 and ζ_2 are the zeta potential of two particles, and κ^{-1} is the EDL thickness. Therefore, the total interaction energy is given as,

$$V_T = V_A + V_R \tag{20}$$

Here, potential barrier energy ($V_{\mathrm{T,max}}$) can be a reference of the particle stability, which should be larger than general requirement, 25 k_BT, to maintain stable state of colloidal particles.[105] Although the submicron particles used in this study are stable with high potential barrier energy as shown in Table 4-2, nanoparticles are much vulnerable to irreversible aggregation in high concentration of solutes. Therefore, it has limitation to select the concentration level of solutes to drive nanoparticles using diffusiophoretic force.

Table 4-2. Potential barrier energy for particle interactions

d_1-d_2 Concentration	200-200 (nm)	200-620 (nm)	620-620 (nm)
1 mM	468	723	1447
10 mM	420	662	1300
100 mM	337	556	1042

Unit: k_BT (≈0.411×10^{-20} J). In addition, the zeta potential is $\zeta_1 = \zeta_2 = -70$ mV for polystyrene particles (i.e., 200 nm, 620 nm).

Second, the self-diffusion induced by Brownian motion is one of the important transport phenomena dealing with nanoparticles. As we mentioned in Fig 4-2, Stokes-Einstein relation ($D_p = k_BT/6\pi\eta a$) describes that the diffusion coefficient of colloidal particles increases as the size of particles decreases. The diffusion coefficient of 200-nm (D_p = 2.45 $\mu\mathrm{m}^2$/s) and 620-nm (D_p = 0.79 $\mu\mathrm{m}^2$/s) particles are much smaller than the net Γ_p, so that the self-diffusion is negligible in this study. However, the diffusion coefficient of nanoparticles (e.g., 50-nm particles, $D_p = 9.8\ \mu m^2/s$) could be comparable to the net Γ_p, which is difficult to make DP-dominant environment to isolate certain nanoparticles in the presence of the limited concentration gradient due to the stability issue. Nevertheless, this work is still interesting approach for separating nanoparticle mixtures because it shows high separation efficiency even in the absence of external energy source. To evaluate the possibility of new technique of nanoparticle separation, we compared this work with different microfluidic approaches for nanoparticle separation, which is shown in Table 4-3. The separation is not continuous in this work due to the dead end channel that leads to the decrease of the throughput. However, solute gradient can be easily produced at any microchannels by the integration of nanochannel. Therefore, it would be possible to separate nanoparticles in a continuous flow in the absence of preconcentration step causing instability; this may require a new concept design of a micro-/nanofluidic device capable of manipulating a steady-state concentration gradient. Of course, the same approach could be applied to various bio-samples requiring separation and/or fractionation on a chip; this is a topic for a future work.

Table 4-3. Comparison of microfluidic approaches for nanoparticle separation

Techniques	Separation marker	Source	Target size	Efficiency	Throughput	Advantage	Disadvantage	Ref.
Deterministic lateral displacement	Size	Laminar flow	190 nm, 2 μm and 600 nm	~ 100 %	0.01 μL min^{-1}	Simple, high efficiency	Low throughput, clogging	62
Hydrodynamic filtration	Size	Hydrodynamic sieving	100 nm and 1 μm	~ 100 %	1 μL min^{-1}	Simple, high efficiency	Membrane clogging	63
Centrifugation	Size, density	Centrifugal force	50 nm, 100 nm, and 200 nm	~ 90 %	7.5 μL min^{-1}	High throughput	External equipment, Not continuous separation	64
Electrostatic sieving	Size	Electrical double layer force	20 nm and 40 nm	~ 97 %	0.5 μL min^{-1}	High efficiency	Low ionic condition, throughput	65
Ion Concentration polarization	Size, electrophoretic mobility	Electrical repulsion	100 nm and 500 nm	~ 95 %	0.5 μL min^{-1}	High efficiency, size selectivity	High voltage source, low throughput	66
Dielectrophoresis	Size	Electric field	51 nm, 140 nm, and 500 nm	~ 100 %	0.01 μL min^{-1}	High efficiency	High voltage source, low throughput	71
Acoustophoresis	Size, density	Ultrasonic sound wave	< 200 nm	~ 90 %	0.5 μL min^{-1}	High efficiency	Fabrication, limitation of material selection	81
Diffusiophoresis	Size, zeta potential	Solute gradient	200 nm, and 620nm	~ 95 %	0.1 nL min^{-1}	High efficiency, power free,	Not continuous separation, low throughput	This work

It is worthwhile to discuss the other critical factors affecting the transport control of colloidal particles because the time-dependent competition of CP, EP, and DO is complex. First, the zeta potentials of the wall and particles clearly determine the diffusioosmotic and diffusiophoretic mobilities, respectively. The zeta potential of polymers is known to change significantly with ionic strength; therefore, the competition between CP and EP can be locally reversed along the target chamber, in which a very steep concentration gradient is formed. Second, the interdiffusion of multispecies ions may be useful for the transport control of colloidal particles; however, such a phenomenon has so far only been used to achieve constant osmolarity.[87] However, the target chamber of the MNDP is a semi-open channel with a two-way passage, comprising both the top main channel and nanochannel, which produces a two-sided nonlinear concentration gradient for existing solutes during buffer changes. Accordingly, the newly introduced solutes can enhance the electric field compared to that produced by the single solute gradient. As a result, the interdiffusion between ionic species may contribute to the acceleration of the preconcentrated particle transport, especially early in the transient stage of the buffer change near the nanochannel. Currently, no study has provided an exact theory to explain the aforementioned factors, and thus more research is required to unveil the unknown dynamics of particles, such as sub-100 nm nanoparticles, in a complex physicochemical environment.

4.4 Conclusion

In summary, we demonstrated that the MNDP, in which nanochannel functions as a porous membrane for the delicate diffusion control of solutes, made it possible to decouple the effect of EP and CP on the resulting DP of colloidal particles by generating stable and long-term concentration gradients in a transient or steady-state manner, facilitating the DP-based dynamic transport control of colloidal particles in the target chamber by only using a pipette. We further demonstrated that the MNDP allows to actively switch the spatiotemporal concentration gradients in the middle of device operation, resulting in the separation and fractionation of submicron particles according to their size or zeta potential by individually manipulating the relative strength of EP and CP, respectively. Furthermore, to the best of our knowledge, this is the first study using the MNDP in conjunction with experimental results to validate the theoretical model that predicts the size-dependent DP of particles in which the direction of CP and EP is reversed. We even showed the remarkable potential of the MNDP for submicron particles separation and fractionation on a chip by varying several engineering factors, such as buffer conditions comprising the diffusivity difference between anions and cations, zeta potential of particles and channel walls that can be engineered by using specific molecules/chemicals, and an interdiffusion phenomenon that requires additional research. It is expected that the DP-based MNDP can be further used for the active transport control of various bio-samples including selective concentration and exclusive separation based on sample features such as physical size and electrical charge density.

Chapter 5. Humidity-Gated Transport System using Polydimethylsiloxane-Based Nanochannels for Mass Transport Control

5.1 Introduction

Controlling transport of water in nanochannel have attracted a great interest due to a variety of practical applications such as drug delivery system [106], biosensing [107-109], energy conversion [110-112], and water desalination [113]. So far, nanofluidic investigations have mainly focused on voltage-gated system to control liquid/vapor interface in hydrophobic solid-state nanopore [114-119]. This mechanism affects not only ion transport but also water flow through the nanopore. Alternatively, the gating system was also facilitated by the introduction of functional material which are in response to physiochemical stimuli such as pH [120], light [121], and temperature [122]. More recently, liquid-gating systems employing functional liquid that is immiscible with water have been demonstrated [123-125]. Although aforementioned techniques with various gating systems provided a functional nanoporous membrane for wide range of applications, they have not shown capability versatile applications of lab-on-a-chip (LOC) due to the limited options of functional material.

In this work, we developed a humidity-gated transport system (HGTS) to control the mass transport by employing a cracking-assisted nanochannel with polydimethylsilxoane (PDMS) which has the gas permeable properties. Since the PDMS is gas permeable, even very small amounts of water continue to evaporate at the wall of micro-/nanofluidic channel. We demonstrated that the water evaporation in the nanochannel significantly affects the water transport through the nanochannel, which is enough for use as a gate of mass transport depending on the relative humidity of the surrounding environment. In addition, we demonstrated that the integration of control channel adjacent to the nanochannel allows for the HGTS to operate individually by supplying nitrogen at desired time. Furthermore, we confirmed that the water evaporation through the PDMS wall induces preconcentration of solutes which can be used for the ion pump. Finally, we also demonstrated the HGTS for both valve and pump can be operated in a stable and repeatable manner for the long-term use due to the functionality that enables not only reversible switching of the relative humidity but also controlling the rate of evaporation.

5.2 Experimental setup

Materials and reagents: A negative photoresist of SU-8 (SU-8 2010, MicroChem, Newton, MA) was used to produce the master mold. Polyurethane acrylate (PUA, MINS-311RM) and polyethylene terephthalate (PET) film (Minuta Tech, Osan, Gyeonggi, Korea) were adopted to replicate negative micro/nanopatterns of the master mold. The replicated positive PUA mold was silanized with chlorotrimethylsilane (Sigma-Aldrich, Yongin, Gyeonggi, Korea). Regular PDMS (Sylgard 184 silicone elastomer kit, Dow Corning, Midland, MI, USA) and an extra-hard PDMS (x-PDMS) were adopted to produce micro-/nanofluidic device. All chemicals used to prepare x-PDMS were purchased from JSI Silicone (Seongnam, Korea), including linear vinyl siloxane (VDT-731), vinyl Q-siloxane (VQX-221), moderator (SIT 7900.0), platinum catalyst (SIP 6831.2LC), and linear hydride siloxane (HMS-501). fluorescein sodium salt (Sigma-Aldrich, Yongin, Gyeonggi, Korea) dissolved in phosphate-buffered saline (PBS, Sigma-Aldrich, Yongin, Gyeonggi, Korea) was prepared to quantify the rate of mass transport.

Fabrication of micro-/nanofluidic devices: A hybrid-scale micro-/nanofluidic device mold was produced by crack-photolithography.[11, 38] Negative patterns produced by cracks were replicated using PET film and PUA solution. Oxygen inhibition on the photocuring of the PUA solution was minimized by adopting a custom-made nitrogen chamber. We introduced a PDMS composite comprising bi-layer structure of x-PDMS and PDMS to resolve the roof-collapse problem.[98] The prepared x-PDMS solution was used to spin-coat the PUA mold at 2,000 rpm, followed by heating at 65 °C for 15 min in the oven. And thus, regular PDMS was poured onto the x-PDMS layer and cured at 65 °C for at least 4 h. Subsequently, oxygen plasma (20 sccm, 50 W for 30 s) was introduced to treat the x-PDMS surface and a glass substrate for producing hydrophilic surfaces with strong and irreversible bonding.

Sample preparation and handling: We prepared two kinds of micro-/nanofluidic device to compare the effect of initial humidity condition on the mass transport. To prepare initially dehydrated device, the fabricated micro-/nanofluidic device was stored in the oven at 65 for 30 min before experiment. To prepare initially hydrated device, the fabricated device was soaked in the water at least 4 hours. All solutions were handled with a pipette to maintain flow rates with hydrostatic pressure during the desired working time.

Experimental setup and data analysis: Optical and fluorescent images were obtained by using an inverted fluorescence microscope (IX-71, Olympus, Japan) equipped with a charge-coupled device (CCD) camera (Clara, Andor, Belfast, Northern Ireland). Image J (National Institutes of Health, Bethesda, MD, USA) and OriginPro 2015 software (OriginLab Corp., Northampton, MA, USA) were used to quantitatively analyze the fluorescence intensities FI of the images. The background noise of FI was subtracted for all quantitative analyses. Atomic force microscopy (AFM; D3100, Veeco, USA) was introduced to quantify the dimension of nanoscale cracks. The PDMS and glass substrate were bonded by using oxygen plasma treatment equipment (Cute-MP, Femto Science, Hwaseong, Korea). A cell incubator (Chamlide TC, Live Cell Instrument, Seoul, Korea) was equipped on the microscope stage to maintain the desired humidity and temperature (37 °C) of the microfluidic device. To measure the temperature and relative humidity in the chamber accurately, a temperature-humidity sensor (SHT15, SENSIRION, Anyang, Gyeonggi, Korea) was integrated with a custom-made electric circuit and a commercial data acquisition system (Arduino Uno R3, Adafruit Industries, USA).

5.3 Results and discussion

Fig. 5-1(a) illustrates a mixed-scale HGTS that can manipulate the mass transport through the nanochannel. We employed a cracking-assisted photolithography[38] (*i.e.*, crack-photolithography) to fabricate a polydimethylsiloxane (PDMS)-based micro/nanofluidic chip. The detailed fabrication process is demonstrated in the methods section. A crack-nanochannel promotes diffusive mass transport but suppresses advection flow toward the connected microchannel due to the high hydraulic resistance. The nanochannel plays a role of gate to control the mass transport between top source channel and bottom drain channel in accordance with the relative humidity near the nanochannel. Since the PDMS is gas permeable material, water can be continuously evaporated through the PDMS wall depending on the relative humidity. In addition, high surface to volume ratio of the nanochannel promotes the evaporation rate that induces liquid/vapor interface in the nanochannel. Because the water supply from both microchannels is limited due to the high hydraulic resistance, liquid connection can be easily broken by the evaporation in long nanochannels.

To understand this behavior, we introduced the thin film flow with the lubrication approximation in nanochannel and permeation driven flow by the evaporation through the PDMS wall [126]. First, the velocity profile $\mathbf{v}(x, z)$ is assumed by simplifying *Navier-Stokes* equation (NSE) and neglecting y-dependence due to the small width w compared to the channel length L ($L \gg w$), which is given as,

$$\frac{\partial^2 v_x}{\partial z^2} = -\frac{1}{\eta}\frac{\partial P}{\partial z} \tag{21}$$

This is valid when the channel length L is much larger than the channel height h ($L \gg h$) with low *Reynolds* number ($\mathrm{Re} \ll 1$), where $\mathrm{Re} = \rho v_x h/\eta$, ρ is the fluid density, and dynamic viscosity of fluid. With the no-slip wall boundary conditions $v_x = 0$ at $z = h$ and $z = 0$, we find

$$v_x = \frac{1}{2\eta}\frac{dP}{dx}(z^2 - hz) \tag{22}$$

Second, the permeation driven flow is assumed from continuity, which is given as,

$$\langle v_x(x) \rangle = -\frac{Jx}{\rho h} \tag{23}$$

where $\langle v_x(x) \rangle$ is averaged flow velocity over the channel height and J is a net flux of water molecules passing through the PDMS wall. To obtain the profile of the pressure in the nanochannel, we assume $P = P_{\mathrm{atm}}$ at $x = L$, because a pressure drop along the channel is much larger than hydrostatic pressure in the reservoir. Since the contribution of pressure drop from x-direction is much larger than z-direction ($L \gg h$), the pressure profile $P = P(\mathrm{x})$ which is given as,

$$P = \frac{6\eta}{\rho}\frac{J}{h^3}(x^2 - L^2) + P_{atm} \tag{24}$$

Here, we define the limit pressure P_{limit} which leads to disconnection due to the evaporation. From the limit pressure, we can specify the critical length L_{critical} to facilitate liquid gating system in the nanochannel.

$$L_{critical} = \sqrt{\frac{\rho h^3}{6\eta J}(P_{atm} - P_{limit})} \tag{25}$$

Therefore, we can predict the channel size for the disconnection and apply it to liquid gating system in response to the relative humidity.

Fig. 5-1(b) shows the working mechanism of the HGTS that facilitates close state in dry condition. At first, the solution is easily filled in the nanochannel by the capillary flow because oxygen plasma treatment for bonding the device to substrate makes hydrophilic surface. However, water evaporation produces vapor phase from the center where the pressure drop is the largest in the nanochannel. As the only water escapes through the PDMS wall, the solutes in the solution are concentrated during the evaporation. To allow for transport of solution through the nanochannel, the evaporation should be inhibited, as shown in Fig. 5-1(c). Fully hydrated PDMS can serve as a barrier to prohibit dehydration of solution in the channel. Although PDMS is well-known hydrophobic material, it can absorb a certain amount of water by directly soaking in water or putting in humid environment for a long time [126]. In this evaporation-inhibited environment, the water in the nanochannel is preserved and thus the preconcentrated solutes can be transported by diffusion from the source to drain channel.

Fig. 5-1(d) shows the microscopy and atomic force microscopy (AFM) images of a typical HGTS with a single nanochannel which is about 3 μm wide and 200 nm deep. Fig. 5-1(e) shows typical examples of HGTS including nanochannel with length at 800 μm to demonstrate open state of hydrated PDMS and close state of dehydrated PDMS. At first, we soaked the PDMS in water for a day to make it fully hydrated by absorbing water molecules. Since the pure water without solutes is difficult to see the difference in nanochannel shape depending on the hydration, fluorescent dye solution was prepared by dissolving 500 μM of fluorescein sodium salt into 1 mM of PBS to distinguish before and after dehydration of the device. While the hydrated PDMS shows a clean shape of nanochannel filled with the solution, the dehydrated PDMS shows a blurry shape around the center of the nanochannel. This indicates that solutes are adsorbed to the dehydrated PDMS wall during the water evaporation. We also demonstrate a reversible switching of HGTS for on/off control of the gate by obtaining sequential fluorescence images from the dehydration to the rehydration of the PDMS, as shown in Fig. 5-1(f). We used previously hydrated device described in Fig. 5-1(e). To manipulate the environment, we employed a pressure regulator connected with nitrogen gas for dehydration and a paper soaked in water for rehydration, respectively. In addition, we conducted experiments in live cell chamber integrated with microscopy to maintain the relative humidity during the desired working time. The solution was continuously flushed into both source and drain channel to produce stable concentration gradient along the nanochannel. During the dehydration, the fluorescence signal darkens in the middle of nanochannel and brightens the side-to-side of nanochannel indicating the concentration of solutes. This preconcentrated fluorescence sodium salt migrated into the drain channel during the hydration and recover the initial concentration in the steady state.

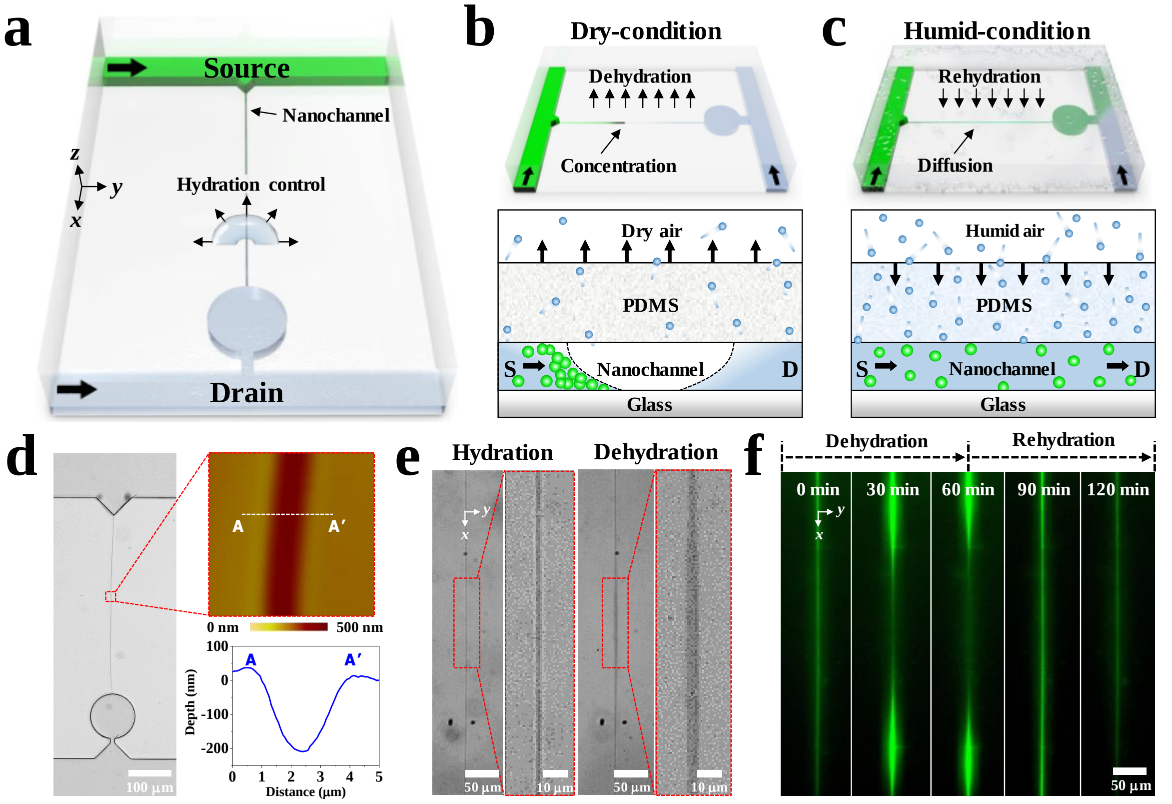

Figure 5-1. Concept of the humidity-gated transport system (HGTS) using the gas permeable nanochannel (a) Schematic illustration of the hydration-based liquid-gating for mass transport control. (b, c) Schematic illustrations of the mechanism of the mass transport control for (b) close state in dry condition and (c) open state in humid condition. (d) Microscopy and atomic force microscopy (AFM) images show the morphology of the device. (e) Microscopic images of the nanochannel in the humid condition and the dry condition, respectively. (f) Sequential images show that the concentration of the fluorescein sodium salt in the dry condition and the diffusion of it in the humid condition. The relative

humidity is periodically switched from 20% to 95% at 1 h intervals.

Liquid gating in the long nanochannel results in the transport of solutes in the connected drain channel. Fig. 5-2 shows the visualization and characterization of the effect of liquid gating on the drain channel depending on various humidity conditions of the device. Since the drain channel is continuously washed by the pure PBS solution, fluorescence intensities are kept constant depending on the amount of transferred fluorescent dye solution. First, the adsorbed water in PDMS is not evaporated in high relative humidity (RH = 95 %), so that the hydrated device continuously expresses the saturated fluorescence signal, as shown in Fig. 5-2(a). Second, the dehydrated device in low relative humidity (RH = 30 %) prevents solution from passing through the nanochannel that leads to no fluorescence signal in the drain channel all the time, as shown in Fig. 5-2(b). Third, the dehydrated device in high relative humidity (RH = 95 %) shows that the fluorescence signal increases gradually with time and then decreases to similar intensity of the hydrated device, as shown in Fig. 5-2(c). As mentioned earlier, solutes that fail to pass the PDMS wall during the water evaporation are concentrated in the nanochannel. Thus, the highly preconcentrated fluorescein sodium salt diffused into the drain channel due to the rehydration of the device. After a certain time (2 h), all concentrated solutes are transferred and equilibrates, resulting in a fluorescence signal that matches the original concentration gradient between the source and drain channels.

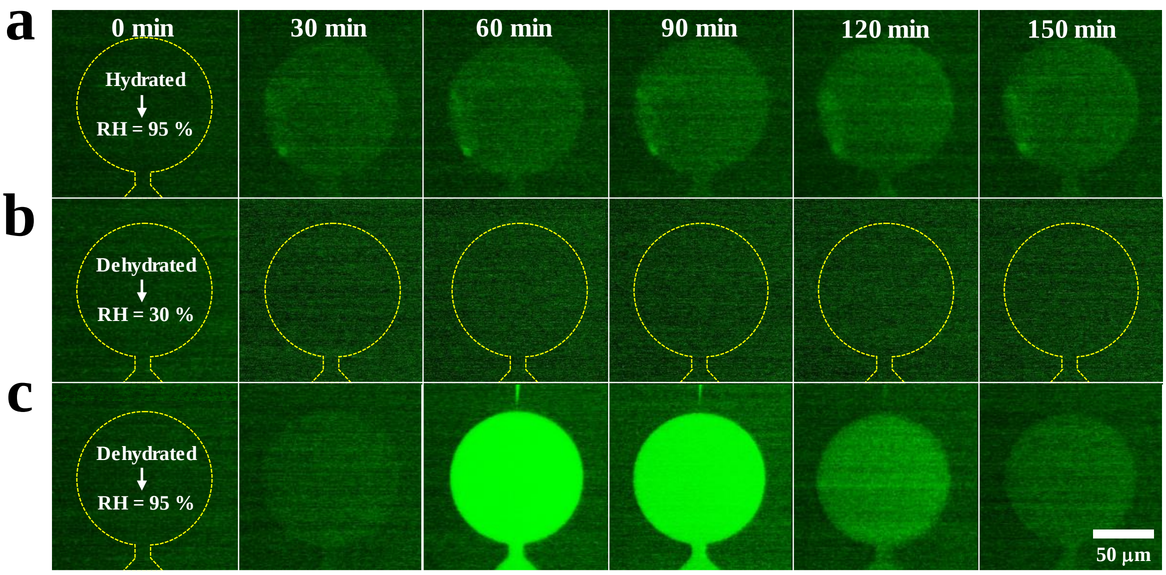

Figure 5-2. Visualization of mass transport control through the manipulation of humidity. Time-lapse fluorescence images show the transported fluorescent dye solution in various humidity conditions: (a) hydrated device with RH = 95 %, (b) dehydrated device with RH = 30 %, and (c) dehydrated device with RH = 95%.

Fig. 5-3 shows the effect of the nanochannel length on the diffusion rate. The nanochannel length is the most important factor to operate HGTS. Because the evaporation rate is proportional to the surface area of the nanochannel wall and the hydraulic resistance is inversely proportional to the nanochannel length. Thus, the device is much vulnerable to be dehydrated in long nanochannels, which induces liquid gating. To characterize it, we prepared different lengths of nanochannels from 50 μm to 800 μm for both hydrated and dehydrated devices and adjusted high relative humidity (RH = 95 %). Fig. 5-3(a) shows that the quantified results for diffusion rate of fluorescein sodium salt depending on the nanochannel length in the hydrated device. As expected, the fluorescence intensities became stronger as the length of nanochannels decreased due to the diffusive mass transport. Fig. 5-3(b) shows that the fluorescence intensities in the case of the dehydrated device. We found that fluorescence intensities in 400 μm and 800 μm length of nanochannels gradually increases and then decreases until saturation after 2 h. This indicates that short nanochannels such as 50 μm, 100 μm, and 200 μm are not much affected by the evaporation, while relatively long nanochannels including 400 μm and 800 μm facilitates liquid gating system.

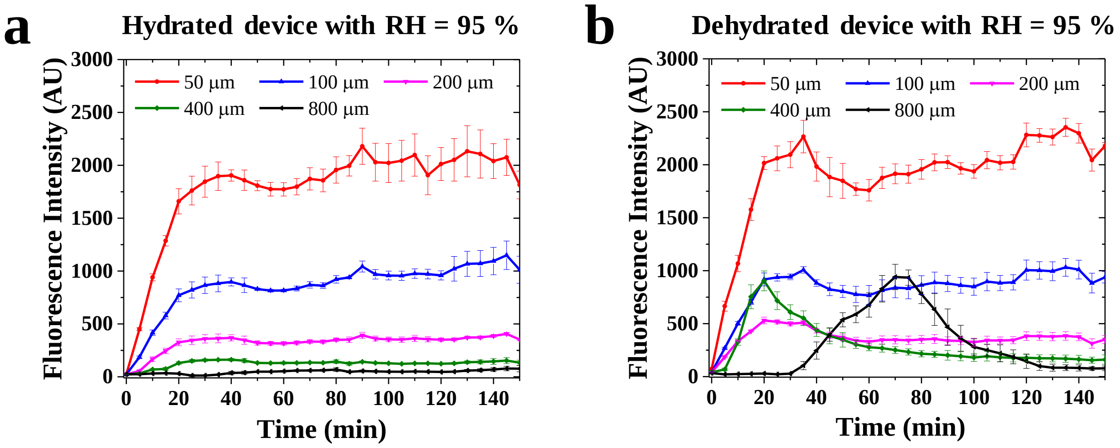

Figure 5-3. Quantification results of the fluorescence intensities in the high relative humidity (RH = 95 %) (a) The diffused fluorescein sodium salt in the hydrated device shows a saturated fluorescence intensities in the order of the length of nanochannel. (b) The fluorescence intensities increases initially and then gradually decreases for 400 μm and 800 μm length of nanochannels, respectively.

To confirm that liquid gating system can be realized by the long nanochannel including 400 μm and 800 μm, we also measured the current with an applied external voltage (5 V), as shown in Fig. 5-4. We loaded solution for both source and drain channels and then produced the dried environment for 30 min to concentrate solutes in the nanochannel with length at 400 μm and 800 μm. We subsequently applied external voltage to measure the current and electrokinetically transport the solutes for 30 s, as shown in Fig. 5-4(a-b). For both the nanochannels, the initially burst current rapidly decreases for 5 s and saturates, as shown in Fig. 5-4(c-d). Since the ionic current is proportional to the amount of solutes, the initial decrease of the current proves that the evaporation of solution in the nanochannel allows for solutes to be concentrated.

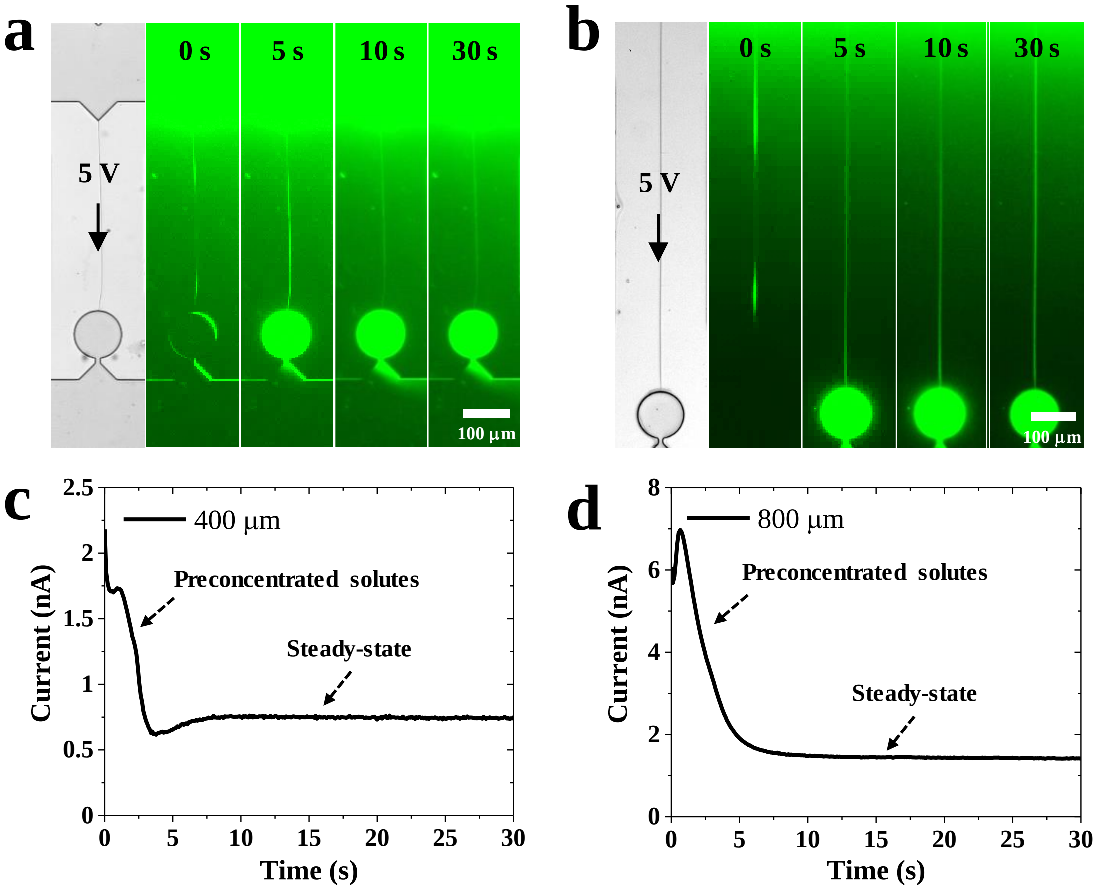

Figure 5-4. Proof of the evaporation-driven preconcentration of solutes. (a-b) Sequential images show that the external electric field (5 V) derive the convection flow to transport the fluorescein sodium salt molecules that is initially preconcentrated in nanochannels with different lengths at (a) 400 μm and (b) 800 μm, respectively. (c-d) Graphs show that the initially burst current gradually decreases and saturates after 5 s for both nanochannels with lengths at (c) 400 μm and (d) 800 μm, respectively. The difference in reduced current indicates that the longer nanochannel, the more solutes are concentrated.

To demonstrate the reversibility of the HGTS between open and close states, we measured fluorescence intensities of the drain channel, while the relative humidity was switched between RH = 20 % when the close state and RH = 95 % when the open state, as shown in Fig. 5-5. Since the preconcentrated solutes during the close state needs enough time to reach a steady state concentration gradient, we switched relative humidity at 2 h intervals. Fig. 5-5(a) demonstrates the reversible control of liquid gating system using the nanochannel with length at 800 μm. Fig. 5-5(b) demonstrates periodical change of fluorescence intensities in nanochannel and connected drain channel depending on the relative humidity. The longer the nanochannel, the larger the evaporation flux, allowing more solutes to be concentrated simultaneously. Therefore, the nanochannel with length at 800 μm transports larger amounts of fluorescein sodium salt during the open state.

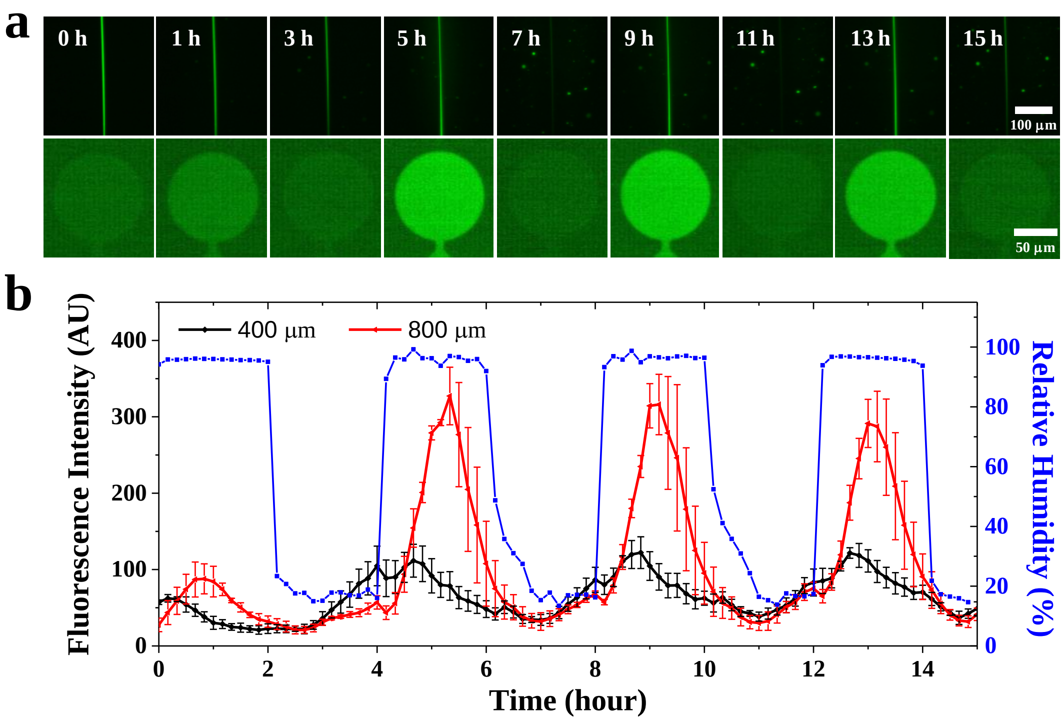

Figure 5-5. Reversible switching of the humidity to control the mass transport. (a) Time-lapse fluorescence images show the fluorescein sodium salt in the nanochannel with length at 800 μm and the connected drain channel, respectively. (b) Quantification results of the fluorescence intensities in the drain channel connected with various nanochannels with length at 400 μm and 800 μm. The relative humidity is periodically switched from 20% to 95% at 2 h intervals.

The design of HGTS can be extended to an individual liquid gating system for a single nanochannel by integrating a control channel connected with a pressure regulator to supply fresh nitrogen for local control of the relative humidity, as shown in Fig. 5-6. The process of the individual liquid gating in the single nanochannel is described in Fig. 5-6(a). Compared to drying the whole container, the local drying with the control channel allows for water in nanochannel to rapidly evaporate due to the relatively large amount of the nitrogen and short distance to the nanochannel. Since the direct supply of nitrogen gas can cause too much evaporation to rehydrate the device, we prepared another neighboring microchannel to provides water molecules constantly. The water supply not only acts as a buffer to alleviate difficult manipulation but also assists rehydration of the device. When the control channel is closed to rehydrate the device, water condensation occurs in the control channel due to the water saturated environment. We demonstrate that the dehydration and rehydration of nanochannel according to the presence of the nitrogen, as shown in Fig. 5-6(b). As mentioned earlier, dehydration of nanochannel is followed by the preconcentration of solutes that is visualized by the fluorescent dye solution. We also observed the water condensation in the control channel during the rehydration. Fig. 5-6(c-d) show the quantified results of hydration control by measuring the fluorescence intensities along the *x*-direction of the nanochannel indicated in Fig. 5-6(b). Interestingly, fluorescence intensities increase simultaneously on both sides of channel, as shown in Fig. 5-6(c). Since the evaporation is strong enough to drives a convection flow ignoring diffusion of solutes, even the solutes that passed through the center of the nanochannel are returned by dragging. In addition, the increase of fluorescence intensities by time demonstrates that a constant supply of nitrogen allows for more solutes concentration. Fig. 5-6(d) shows the migration by diffusion of preconcentrated solutes during the rehydration. The fluorescence intensity demonstrates that nonlinear concentration gradient of solutes induced by the evaporation approaches equilibrium in 30 min.

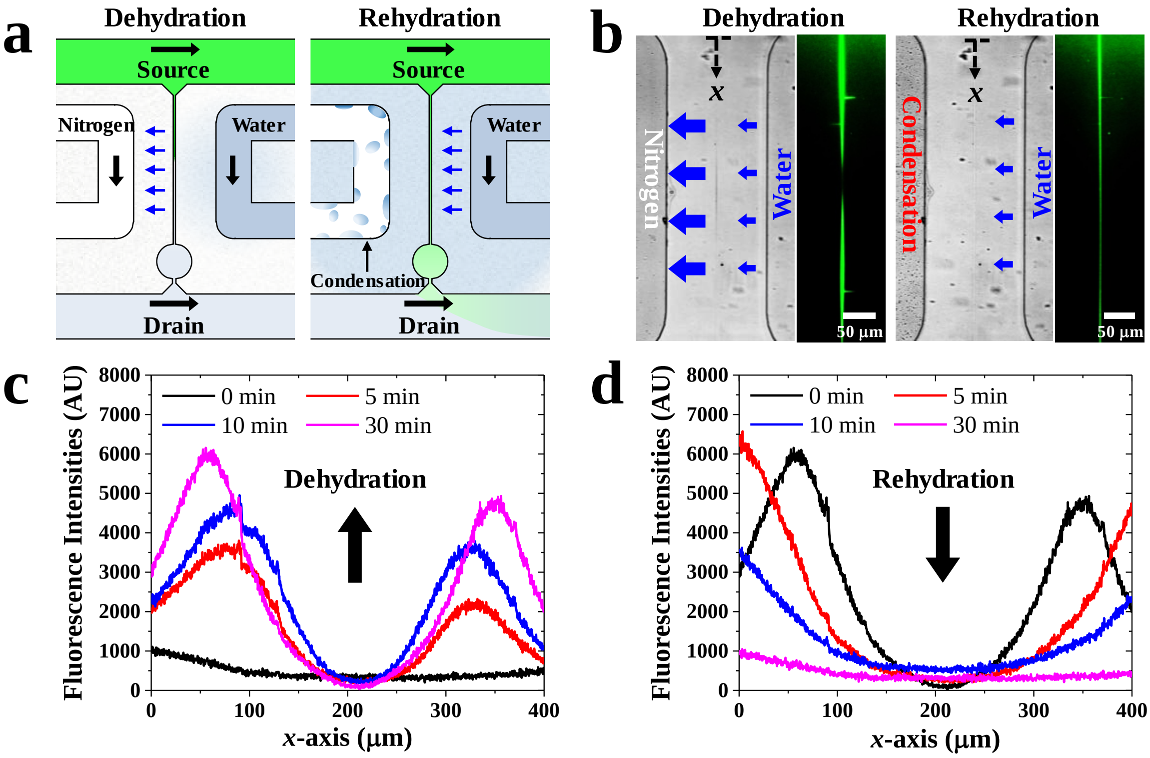

Figure 5-6. Individual liquid gating system enabled by integration of control channel. (a) Schematic illustration of working principle of the individual liquid gating system by the integration of the control channel to supply the nitrogen near the nanochannel. Blue arrows near the nanochannel imply the direction of the water transport. (b) Microscopic images of the individual liquid gating system depending on the supply of nitrogen. Blue arrows near the nanochannel imply the direction and the scale of the water transport. Fluorescence intensities along the *x*-direction described in (b) shows (c) the preconcentration of fluorescent dye during the dehydration and (d) the diffusion of the solution during the rehydration, respectively.

The individual control of HGTS offers active and various forms of mass transport control due to the fast and strong regulation of the pressure. As long as dehydration continues, solutes are continuously dragged and concentrated in the center of the nanochannel so that the HGTS can prohibit from solutes transferring to the drain channel during the dehydration. To demonstrate practical advantages as a mass transport controller, we characterize the response time to evacuate the drain channel and the amount of transported solutes, as shown in Fig. 5-7(a-c). We measured fluorescence intensities of the drain channel to compare the time for evacuation of the drain channel according to the applied pressure at 5, 10, and 20 kPa, respectively, as shown in Fig. 5-7(a). We confirmed that the low pressure (5 kPa) is still enough to operate the individual liquid gating system to evacuate the drain channel within 5 min. We also characterized the amount of transported solutes preconcentrated in nanochannel during the dehydration according to the applied pressure to the control channel, as shown in Fig. 5-7(b). For each pressure, we fixed the time to supply the nitrogen to the control channel at 10 min. The quantification results shows that the amount of transported solutes is linearly proportional to the increase in pressure. In addition, the time to reach the maximum value of fluorescence intensity increases as the pressure increases. Because the higher pressure induces the larger water evaporation, which requires more time to rehydrate the device to make a diffusion environment. Although it is obvious that a high pressure facilitates more solutes concentration and fast response to evacuate the drain channel during the dehydration, pressures higher than 20 kPa are not recommended due to the soft material properties of the PDMS. Since the microchannel also has the high hydraulic resistance, the PDMS wall is highly pressurized resulting in detachment of the device from the substrate or leakage of solution. Fig. 5-7(c) shows the amount of transported solutes preconcentrated in nanochannel depending on the dehydration time for 10, 30, 60 min, respectively. To compare the contribution of the dehydration time, we fixed applied pressure at 10 kPa to the control channel. Similar to the control by the applied pressure, the amount of transported solutes is almost linearly proportional to the increase in time for dehydration. Furthermore, the time to reach the maximum value of fluorescence intensity follows a similar tendency of which of the pressure control. From this experiment, we confirmed that the HGTS facilitates not only the valve at the molecular level to the pump in femtolitre scale by controlling the applied pressure to the control channel and the dehydration time.

We also demonstrated a programmable mass transport control by changing the switching time for hydration, as shown in Fig. 5-7(d). We fixed the applied pressure at 10 kPa to the control channel to maintain a uniform concentration rate. In addition, rehydration time was fixed at 30 min to demonstrate a uniform transport rate during the working time. To demonstrate dynamic control of mass transport in terms of time and the amount of transported molecules, the dehydration time was varied at 10, 30, 60 min, respectively. The dehydration and rehydration time is indicated by the reddish and yellowish color, respectively. We found that fluorescence intensity rapidly decreases at the end of each rehydration, which is attributed to the fast transition to the dehydration. This means that the drain channel can be evacuated in minutes regardless of the amount remaining. In addition, the diffusion-controlled nanochannel conveniently provided not only on/off control as a conventional liquid gating system using nanochannel but also precise pump in femtolitre scale for long-term use in a stable manner. Therefore, we demonstrated that the HGTS may have applications in mass transport control at molecular level for a long time without external voltage.

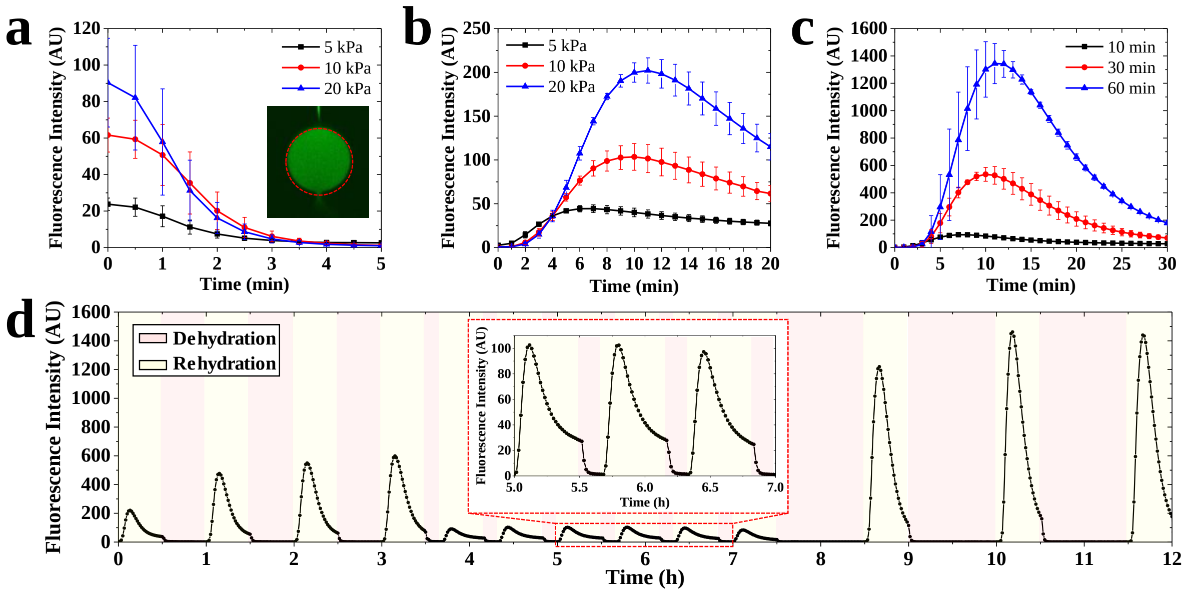

Figure 5-7. Mass transport control by individual liquid gating system. (a) Quantification of the time to wash the remained solutes in the drain channel during the dehydration with various applied pressure to the control channel. (b-c) Control of the amount of preconcentrated solutes according to (b) various pressures applied to the control channel for 10 min and (c) the dehydration time under the pressure applied to the control channel at 10 kPa, respectively. (d) Reversible switching for programmable mass transport control with different amounts of solutes by changing the time of dehydration and rehydration.

Finally, we demonstrated that the HGTS facilitates an addressable control of the multiplexed gate by using a nanochannel array incorporated with an array of control channels, as shown in Fig. 5-8. We produced a single microchamber integrated with three nanochannels, which are connected with different source channels (S1, S2, and S3). Fig. 5-8(a) shows that each nanochannel consists of an aforementioned individual gating system connected to a pair of control channels. To demonstrate the transport of fluorescence dye from each nanochannel, we continuously cleaned the target chamber by flushing with pure PBS solution in the bottom channel. Fig. 5-8(b) and (c) show various combination of the control for gates from the single nanochannel and pairs of nanochannels, respectively. Since the control channel only affects neighboring nanochannel, each nanochannel can be individually controlled. Therefore, such micro-/nanofluidic structures allow for the HGTS to operate the addressable control of mass transport which has potential in a variety of applications assisted by multiplexed source on a single chip in a reversible and repeatable manner.

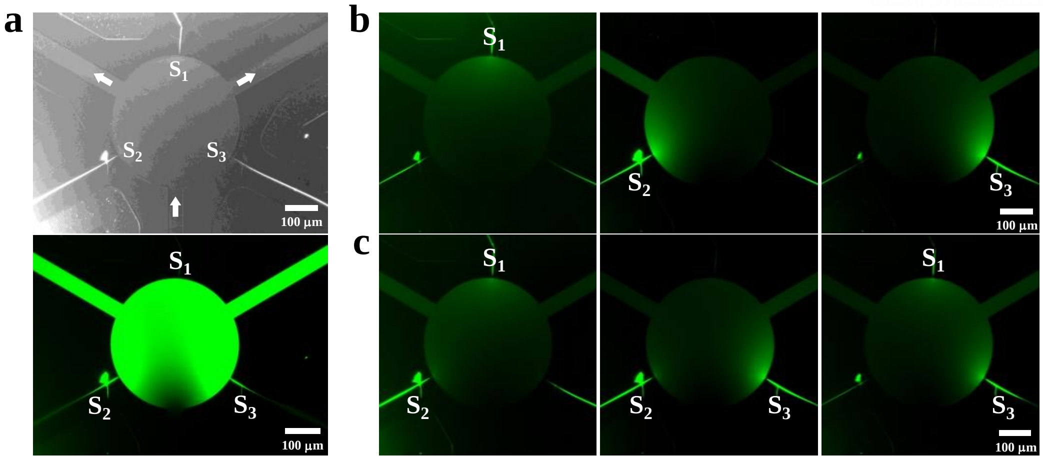

Figure 5-8. Addressable control of mass transport facilitated by the integration of gate array in single chamber. (a) Microscopic images show the HGTS with the gate array composed of three different source channels filled with fluorescence dye solution. (b) Control of mass transport from each single source channel. (c) Control of mass transport from a pair of source channel.

5.4 Conclusion

In summary, we developed the HGTS to allow the manipulation of the mass transport by controlling hydration rate through the wall of gas permeable nanochannel. We adopted cracking-assisted photolithograph to produce PDMS-based micro/nanofluidic device in which the nanochannel functions as a gate that reacts to the relative humidity. We demonstrated that the water in gas permeable nanochannel is vulnerable to evaporate as the length of nanochannel increases due to the high hydraulic resistance and surface to volume ratio. In addition, we demonstrated that the HGTS can be further applied for an individual liquid gating system to control the mass transport through the nanochannel individually by locally integrating the control channel for nitrogen supply. We even showed that the HGTS acts as a not only valve at molecular level but also pump in femtolitre scale by adjusting the applied pressure to the control channel and the dehydration time. Furthermore this device shows a enough stability and reversibility to switch on/off state of gate as well as transport a specific amount of solutes for a long time in a programmable manner.

It is expected that the HGTS can be further used for the precise and active transport control of ions in aqueous solution that is widely used for various bio/chemical assay. Since external voltage is not required to transport target molecules through the nanochannel, this shows a remarkable potential to replace the voltage-gated system for a wide range of applications including electrically vulnerable samples in a cost-effective manner as well. Therefore, the aforementioned transport control systems and techniques may broaden the applicability of µTASs by providing extremely small scale of pump and valve at molecular level for long-term use in a stable and cost-effective manner.

Chapter 6. Conclusions and future outlook

In this dissertation, nanochannel-assisted microfluidic device was developed to facilitate active control of mass transport in hybrid-scale micro-/nanofluidic channel networks. The integration of nanochannel allows diffusion-based transport of ions and molecules but prevents convective flows, which makes it easy to change the physiochemical environment in the connected microchannel. To make the nanochannel as a nanoporous memebrane to deliver molecules to various shape of microchannel, we employed the crack-photolithography that can produce the microchannel and integrated-nanochannel simultaneously in any desired position by using a standard photolithography equipment. In addition, the modified soft lithography provides a stable and cost-effective manner to produce the PDMS-based nanochannel which have been hindered due to the roof-collapse problem of soft material. Thus, the combination of crack-photolithography and modified soft lithography can provide hybrid-scale of micro-/nanofluidic devices with various designs of nanochannel from short channel for rapid environmental switching and long channel for direct mass transport control (Chapter 2).

First, the hybrid-scale micro-/nanofluidic device with the short nanochannel was applied to rapid switching of the physiochemical environment for manipulation of colloidal particles. Although the rate of mass transport depends on diffusion coefficient in nature, a short diffusion distance allows rapid change of physiochemical environment without assistance of convection flow requiring high pressure source. We applied it to diffusiophoresis that needs a solute gradient to control the motion of charged species including colloidal particles. Since the solute gradient can be easily changed during the operation of the device with only pipette, dynamic transport control for colloidal particles is possible according to various purposes such as concentration and extraction of target samples (Chapter 3). In addition, this hybrid-scale micro-/nanofluidic device facilitates not only separation but also fractionation of nanoparticles by size using the same manner (Chapter 4). It means that the proposed technique can be extended to portable and self-containable manipulator for pretreatment of raw samples, which is essential to realize the μTAS for least source environment.

Second, a gas permeable nanochannel with a long length was fabricated to produce a small space that is vulnerable to evaporation of water. The high hydraulic resistance of the nanochannel induces a disconnection of liquid phase at the middle of nanochannel due to the significant evaporation compared to the water supply from the reservoir in the dry environment. Such phenomenon can be exploited as a liquid gating system which respond to the relative humidity near the nanochannel. Since the convection flow induced by the water evaporation is strong enough to concentrate solutes ignoring the diffusion, the nanochannel can be used to ion pump in femtolitre scale as well as the valve at molecular level. In addition, an addressable control of mass transport in a single nanochannel is possible in a programmable manner due to the integration of control channel supplying nitrogen for manipulation of evaporation rate. Consequently, the suggested humidity-based liquid gating system provides functions to successfully prevent mass transfer or to repeatedly pass the desired amount of solutes in a long-term manner (Chapter 5).

In the future, the hybrid-scale nanochannel-integrated microfluidic devices can be further extended to a variety of diffusion-based bio/chemical assays such as detection of biomolecules, pretreatment of raw samples, genetic induction, and nanoparticle separation, which need precise manipulation of ionic species and colloidal particles. First of all, the crack-photolithography and modified soft lithography induces a reduction in the cost of fabrication of hybrid-scale micro-/nanofluidic devices with high reproducibility compared to the conventional nanofabrication methods. In addition, limitation of conventional fabrication methods for PDMS-based nanochannel have been overcome, making PDMS properties such as gas permeability, bio-compatibility, transparency, and low cost applicable to nanoscale bio/chemical analysis. The fabricated hybrid-scale micro-/nanofluidic devices also employ simple and inexpensive methods such as diffusion-based concentration gradient formation and humidity-based liquid gating for the induction of spontaneous motion of colloidal particles and the operation of pump and valve, respectively. In this context, the nanochannel-assisted fluidic system for active control of mass transport introduced in this dissertation would be a contribution to go one step further for the realization of portable and miniaturized total analysis systems dealing with bio/chemical applications.

References

1. Pierce, C.G., P. Uppuluri, A.R. Tristan, F.L. Wormley, E. Mowat, G. Ramage and J.L. Lopez-Ribot, A simple and reproducible 96-well plate-based method for the formation of fungal biofilms and its application to antifungal susceptibility testing. *Nat. Protoc.*, **2008**. 3(9), 1494-1500.
2. Sia, S.K. and G.M. Whitesides, Microfluidic devices fabricated in poly(dimethylsiloxane) for biological studies. *Electrophoresis*, **2003**. 24(21), 3563-3576.
3. Abate, A.R., T. Hung, R.A. Sperling, P. Mary, A. Rotem, J.J. Agresti, M.A. Weiner and D.A. Weitz, DNA sequence analysis with droplet-based microfluidics. *Lab Chip*, **2013**. 13(24), 4864-4869.
4. Malhotra, R., V. Patel, B.V. Chikkaveeraiah, B.S. Munge, S.C. Cheong, R.B. Zain, M.T. Abraham, D.K. Dey, J.S. Gutkind and J.F. Rusling, Ultrasensitive Detection of Cancer Biomarkers in the Clinic by Use of a Nanostructured Microfluidic Array. *Anal. Chem.*, **2012**. 84(14), 6249-6255.
5. Sun, B., J. Lembong, V. Normand, M. Rogers and H.A. Stone, Spatial-temporal dynamics of collective chemosensing. *Proc. Natl. Acad. Sci. U. S. A.*, **2012**. 109(20), 7753-7758.
6. Kim, Y., K.S. Kim, K.L. Kounovsky, R. Chang, G.Y. Jung, J.J. dePablo, K. Jo and D.C. Schwartz, Nanochannel confinement: DNA stretch approaching full contour length. *Lab Chip*, **2011**. 11(10), 1721-1729.
7. Pu, Q., J. Yun, H. Temkin and S. Liu, Ion-Enrichment and Ion-Depletion Effect of Nanochannel Structures. *Nano Lett.*, **2004**. 4(6), 1099-1103.
8. Zhao, X., X.M. Huang, X.M. Wang, Y. Wu, A.K. Eisfeld, S. Schwind, D. Gallego-Perez, P.E. Boukany, G.I. Marcucci and L.J. Lee, Nanochannel Electroporation as a Platform for Living Cell Interrogation in Acute Myeloid Leukemia. *Adv. Sci.*, **2015**. 2(12).
9. Kim, B., J. Heo, H.J. Kwon, S.J. Cho, J. Han, S.J. Kim and G. Lim, Tunable Ionic Transport for a Triangular Nanochannel in a Polymeric Nanofluidic System. *ACS Nano*, **2013**. 7(1), 740-747.
10. Karnik, R., C.H. Duan, K. Castelino, H. Daiguji and A. Majumdar, Rectification of ionic current in a nanofluidic diode. *Nano Lett.*, **2007**. 7(3), 547-551.
11. Kim, M. and T. Kim, Crack-Photolithography for Membrane-Free Diffusion-Based Micro/Nanofluidic Devices. *Anal. Chem.*, **2015**. 87(22), 11215-11223.
12. Ha, D., J. Hong, H. Shin and T. Kim, Unconventional micro-/nanofabrication technologies for hybrid-scale lab-on-a-chip. *Lab Chip*, **2016**. 16(22), 4296-4312.
13. Abgrall, P. and N.T. Nguyen, Nanofluidic Devices and Their Applications. *Anal. Chem.*, **2008**. 80(7), 2326-2341.
14. Haywood, D.G., A. Saha-Shah, L.A. Baker and S.C. Jacobson, Fundamental Studies of Nanofluidics: Nanopores, Nanochannels, and Nanopipets. *Anal. Chem.*, **2015**. 87(1), 172-187.
15. Aizel, K., V. Agache, C. Pudda, F. Bottausci, C. Fraisseix, J. Bruniaux, F. Navarro and Y. Fouillet, Enrichment of nanoparticles and bacteria using electroless and manual actuation modes of a bypass nanofluidic device. *Lab Chip*, **2013**. 13(22), 4476-4485.
16. He, Q.H., S. Chen, Y. Su, Q. Fang and H.W. Chen, Fabrication of 1D nanofluidic channels on glass substrate by wet etching and room-temperature bonding. *Anal. Chim.*

Acta, **2008**. 628(1), 1-8.

17. Wang, C., Y. Shi, J. Wang, J. Pang and X.H. Xia, Ultrasensitive Protein Concentration Detection on a Micro/Nanofluidic Enrichment Chip Using Fluorescence Quenching. *ACS Appl. Mater. Interfaces*, **2015**. 7(12), 6835-6841.
18. Liu, J.S., H.C. Qiao, Z. Xu, C. Liu, J.Y. Wang, L.Q. Du, X. Zhang and L.D. Wang, Fabrication of planar nanofluidic channels in thermoplastic polymers by O-2 plasma etching. *MICRO NANO LETT.*, **2012**. 7(2), 159-162.
19. Yasui, T., N. Kaji, R. Ogawa, S. Hashioka, M. Tokeshi, Y. Horiike and Y. Baba, DNA Separation in Nanowall Array Chips. *Anal. Chem.*, **2011**. 83(17), 6635-6640.
20. Perry, J.M., Z.D. Harms and S.C. Jacobson, 3D Nanofluidic Channels Shaped by Electron-Beam-Induced Etching. *Small*, **2012**. 8(10), 1521-1526.
21. Bilenberg, B., S. Jacobsen, M.S. Schmidt, L.H.D. Skjolding, P. Shi, P. Bøggild, J.O. Tegenfeldt and A. Kristensen, High resolution 100kV electron beam lithography in SU-8. *Microelectron. Eng.*, **2006**. 83(4), 1609-1612.
22. Menard, L.D. and J.M. Ramsey, Electrokinetically-Driven Transport of DNA through Focused Ion Beam Milled Nanofluidic Channels. *Anal. Chem.*, **2013**. 85(2), 1146-1153.
23. Angeli, E., C. Manneschi, L. Repetto, G. Firpo and U. Valbusa, DNA manipulation with elastomeric nanostructures fabricated by soft-moulding of a FIB-patterned stamp. *Lab Chip*, **2011**. 11(15), 2625-2629.
24. Yin, Z.F., L. Sun, H.L. Zou and E. Cheng, Two dimensional PMMA nanofluidic device fabricated by hot embossing and oxygen plasma assisted thermal bonding methods. *Nanotechnology*, **2015**. 26(21), 215302.
25. Yin, Z.F., E. Cheng and H.L. Zou, A novel hybrid patterning technique for micro and nanochannel fabrication by integrating hot embossing and inverse UV photolithography. *Lab Chip*, **2014**. 14(9), 1614-1621.
26. Xia, D.Y., Z.Y. Ku, S.C. Lee and S.R.J. Brueck, Nanostructures and Functional Materials Fabricated by Interferometric Lithography. *Adv. Mater.*, **2011**. 23(2), 147-179.
27. van Rijn, C.J.M., Laser interference as a lithographic nanopatterning tool. *Journal of Microlithography Microfabrication and Microsystems*, **2006**. 5(1), 011012.
28. Li, B., Y.P. Cao, X.Q. Feng and H.J. Gao, Mechanics of morphological instabilities and surface wrinkling in soft materials: a review. *Soft Matter*, **2012**. 8(21), 5728-5745.
29. Chung, S., J.H. Lee, M.W. Moon, J. Han and R.D. Kamm, Non-lithographic wrinkle nanochannels for protein preconcentration. *Adv. Mater.*, **2008**. 20(16), 3011-3016.
30. Nagashima, S., H. Ebrahimi, K.R. Lee, A. Vaziri and M.W. Moon, Tunable Nanochannels Fabricated by Mechanical Wrinkling/Folding of a Stiff Skin on a Soft Polymer. *Adv. Mater. Interfaces*, **2015**. 2(3).
31. Kim, M., D.J. Kim, D. Ha and T. Kim, Cracking-assisted fabrication of nanoscale patterns for micro/nanotechnological applications. *Nanoscale*, **2016**. 8(18), 9461-9479.
32. Huh, D., K.L. Mills, X.Y. Zhu, M.A. Burns, M.D. Thouless and S. Takayama, Tuneable elastomeric nanochannels for nanofluidic manipulation. *Nat. Mater.*, **2007**. 6(6), 424-428.
33. Mills, K.L., D. Huh, S. Takayama and M.D. Thouless, Instantaneous fabrication of arrays of normally closed, adjustable, and reversible nanochannels by tunnel cracking. *Lab Chip*, **2010**. 10(12), 1627-1630.
34. Park, S.M., Y.S. Huh, H.G. Craighead and D. Erickson, A method for nanofluidic device prototyping using elastomeric collapse. *Proc. Natl. Acad. Sci. U. S. A.*, **2009**. 106(37), 15549-15554.
35. Heo, J., H.J. Kwon, H. Jeon, B. Kim, S.J. Kim and G. Lim, Ultra-high-aspect-orthogonal and tunable three dimensional polymeric nanochannel stack array for

BioMEMS applications. *Nanoscale*, **2014**. 6(16), 9681-9688.

36. Yu, C.J. and H.Q. Jiang, Forming wrinkled stiff films on polymeric substrates at room temperature for stretchable interconnects applications. *Thin Solid Films*, **2010**. 519(2), 818-822.
37. Huang, Y.G.Y., W.X. Zhou, K.J. Hsia, E. Menard, J.U. Park, J.A. Rogers and A.G. Alleyne, Stamp collapse in soft lithography. *Langmuir*, **2005**. 21(17), 8058-8068.
38. Kim, M., D. Ha and T. Kim, Cracking-assisted photolithography for mixed-scale patterning and nanofluidic applications. *Nat. Commun.*, **2015**. 6, 6247.
39. Lee, Y., Y. Lim and H. Shin, Mixed-scale channel networks including Kingfisher-beak-shaped 3D microfunnels for efficient single particle entrapment. *Nanoscale*, **2016**. 8(23), 11810-11817.
40. Zhou, Z., Q.A. Huang, W.H. Li, W. Lu, Z. Zhu and M. Feng, *The swelling effects during the development processes of deep UV lithography of SU-8 photoresists: Theoretical study, simulation and verification*, in *IEEE Sens. J.* 2007. p. 325-328.
41. Mawatari, K., Y. Kazoe, H. Shimizu, Y. Pihosh and T. Kitamori, Extended-Nanofluidics: Fundamental Technologies, Unique Liquid Properties, and Application in Chemical and Bio Analysis Methods and Devices. *Anal. Chem.*, **2014**. 86(9), 4068-4077.
42. Ghosal, S., Fluid mechanics of electroosmotic flow and its effect on band broadening in capillary electrophoresis. *ELECTROPHORESIS*, **2004**. 25(2), 214-228.
43. Kim, B.C., P. Weerappuli, M.D. Thouless and S. Takayama, Fracture fabrication of a multi-scale channel device that efficiently captures and linearizes DNA from dilute solutions. *Lab Chip*, **2015**. 15(5), 1329-1334.
44. Gao, K.L., L. Li, L.N. He, K. Hinkle, Y. Wu, J.Y. Ma, L.Q. Chang, X. Zhao, D.G. Perez, S. Eckardt, J. McLaughlin, B.Y. Liu, D.F. Farson and L.J. Lee, Design of a Microchannel- Nanochannel- Microchannel Array Based Nanoelectroporation System for Precise Gene Transfection. *Small*, **2014**. 10(5), 1015-1023.
45. Kim, T. and E. Meyhofer, Nanofluidic concentration of selectively extracted biomolecule anattes by microtubules. *Anal. Chem.*, **2008**. 80(14), 5383-5390.
46. Wang, Z., I. Lee, T.J. Jeon and S.M. Kim, Micro-/nanofluidic device for tunable generation of a concentration gradient: application to Caenorhabditis elegans chemotaxis. *Anal. Bioanal. Chem.*, **2014**. 406(11), 2679-2686.
47. Crivello, J.V., The discovery and development of onium salt cationic photoinitiators. *J. Polym. Sci., Part A: Polym. Chem.*, **1999**. 37(23), 4241-4254.
48. Keller, S., D. Haefliger and A. Boisen, Fabrication of thin SU-8 cantilevers: initial bending, release and time stability. *J. Micromech. Microeng.*, **2010**. 20(4), 045024.
49. Anhoj, T.A., A.M. Jorgensen, D.A. Zauner and J. Hübner, The effect of soft bake temperature on the polymerization of SU-8 photoresist. *J. Micromech. Microeng.*, **2006**. 16(9), 1819-1824.
50. Jamal, M., A.M. Zarafshar and D.H. Gracias, Differentially photo-crosslinked polymers enable self-assembling microfluidics. *Nat. Commun.*, **2011**. 2, 527.
51. Unger, M.A., H.-P. Chou, T. Thorsen, A. Scherer and S.R. Quake, Monolithic Microfabricated Valves and Pumps by Multilayer Soft Lithography. *Science*, **2000**. 288(5463), 113.
52. Wang, Y.-C., A.L. Stevens and J. Han, Million-Fold Preconcentration of Proteins and Peptides by Nanofluidic Filter. *Anal. Chem.*, **2005**. 77(14), 4293-4299.
53. Kim, S.M., M.A. Burns and E.F. Hasselbrink, Electrokinetic Protein Preconcentration Using a Simple Glass/Poly(dimethylsiloxane) Microfluidic Chip. *Anal. Chem.*, **2006**. 78(14), 4779-4785.
54. Yeh, S.-H., K.-H. Chou and R.-J. Yang, Sample pre-concentration with high enrichment

factors at a fixed location in paper-based microfluidic devices. *Lab Chip*, **2016**. 16(5), 925-931.

55. Martel, J.M., K.C. Smith, M. Dlamini, K. Pletcher, J. Yang, M. Karabacak, D.A. Haber, R. Kapur and M. Toner, Continuous Flow Microfluidic Bioparticle Concentrator. *Sci. Rep.*, **2015**. 5, 11300.
56. Escobedo, C., A.G. Brolo, R. Gordon and D. Sinton, Optofluidic Concentration: Plasmonic Nanostructure as Concentrator and Sensor. *Nano Lett.*, **2012**. 12(3), 1592-1596.
57. Petersson, F., L. Åberg, A.-M. Swärd-Nilsson and T. Laurell, Free Flow Acoustophoresis: Microfluidic-Based Mode of Particle and Cell Separation. *Anal. Chem.*, **2007**. 79(14), 5117-5123.
58. Shafiee, H., M.B. Sano, E.A. Henslee, J.L. Caldwell and R.V. Davalos, Selective isolation of live/dead cells using contactless dielectrophoresis (cDEP). *Lab Chip*, **2010**. 10(4), 438-445.
59. Wainright, A., U.T. Nguyen, T. Bjornson and T.D. Boone, Preconcentration and separation of double-stranded DNA fragments by electrophoresis in plastic microfluidic devices. *ELECTROPHORESIS*, **2003**. 24(21), 3784-3792.
60. Bhagat, A.A.S., H.W. Hou, L.D. Li, C.T. Lim and J. Han, Pinched Flow Coupled Shear-Modulated Inertial Microfluidics for High-Throughput Rare Blood Cell Separation. *Lab Chip*, **2011**. 11(11), 1870-1878.
61. Zhou, Y., Z. Ma and Y. Ai, Sheathless inertial cell focusing and sorting with serial reverse wavy channel structures. *Microsyst. Nanoeng.*, **2018**. 4(1), 5.
62. Huang, L.R., E.C. Cox, R.H. Austin and J.C. Sturm, Continuous Particle Separation Through Deterministic Lateral Displacement. *Science*, **2004**. 304(5673), 987-990.
63. Davies, R.T., J. Kim, S.C. Jang, E.-J. Choi, Y.S. Gho and J. Park, Microfluidic filtration system to isolate extracellular vesicles from blood. *Lab Chip*, **2012**. 12(24), 5202-5210.
64. Arosio, P., T. Müller, L. Mahadevan and T.P.J. Knowles, Density-Gradient-Free Microfluidic Centrifugation for Analytical and Preparative Separation of Nanoparticles. *Nano Lett.*, **2014**. 14(5), 2365-2371.
65. Zeming, K.K., N.V. Thakor, Y. Zhang and C.-H. Chen, Real-time modulated nanoparticle separation with an ultra-large dynamic range. *Lab Chip*, **2016**. 16(1), 75-85.
66. Jeon, H., H. Lee, K.H. Kang and G. Lim, Ion concentration polarization-based continuous separation device using electrical repulsion in the depletion region. *Sci. Rep.*, **2013**. 3(1), 3483.
67. Lim, J.W., K.S. Shin, J. Moon, S.K. Lee and T. Kim, A Microfluidic Platform for High-Throughput Screening of Small Mutant Libraries. *Anal. Chem.*, **2016**. 88(10), 5234-5242.
68. Kim, H.S., T.P. Devarenne and A. Han, A high-throughput microfluidic single-cell screening platform capable of selective cell extraction. *Lab Chip*, **2015**. 15(11), 2467-2475.
69. Fronczek, C.F., T.S. Park, D.K. Harshman, A.M. Nicolini and J.-Y. Yoon, Paper microfluidic extraction and direct smartphone-based identification of pathogenic nucleic acids from field and clinical samples. *RSC Advances*, **2014**. 4(22), 11103-11110.
70. Dey, K.K., S. Das, M.F. Poyton, S. Sengupta, P.J. Butler, P.S. Cremer and A. Sen, Chemotactic Separation of Enzymes. *ACS Nano*, **2014**. 8(12), 11941-11949.
71. Zhao, K., R. Peng and D. Li, Separation of nanoparticles by a nano-orifice based DC-dielectrophoresis method in a pressure-driven flow. *Nanoscale*, **2016**. 8(45), 18945-18955.

72. Park, E.S., C. Jin, Q. Guo, R.R. Ang, S.P. Duffy, K. Matthews, A. Azad, H. Abdi, T. Todenhöfer, J. Bazov, K.N. Chi, P.C. Black and H. Ma, Continuous Flow Deformability-Based Separation of Circulating Tumor Cells Using Microfluidic Ratchets. *Small*, **2016**. 12(14), 1909-1919.
73. Duval, J.F.L. and H. Ohshima, Electrophoresis of Diffuse Soft Particles. *Langmuir*, **2006**. 22(8), 3533-3546.
74. Vanhoenacker, G., L. Goris and P. Sandra, Capillary zone electrophoresis for the characterization of latex particles. *ELECTROPHORESIS*, **2001**. 22(12), 2490-2494.
75. Unni, H.N., H.J. Keh and C. Yang, Analysis of electrokinetic transport of a spherical particle in a microchannel. *ELECTROPHORESIS*, **2007**. 28(4), 658-664.
76. Vahey, M.D. and J. Voldman, An Equilibrium Method for Continuous-Flow Cell Sorting Using Dielectrophoresis. *Anal. Chem.*, **2008**. 80(9), 3135-3143.
77. Zhang, C., K. Khoshmanesh, A. Mitchell and K. Kalantar-zadeh, Dielectrophoresis for manipulation of micro/nano particles in microfluidic systems. *Anal. Bioanal. Chem.*, **2010**. 396(1), 401-420.
78. Kralj, J.G., M.T.W. Lis, M.A. Schmidt and K.F. Jensen, Continuous Dielectrophoretic Size-Based Particle Sorting. *Anal. Chem.*, **2006**. 78(14), 5019-5025.
79. Ding, X., S.-C.S. Lin, B. Kiraly, H. Yue, S. Li, I.-K. Chiang, J. Shi, S.J. Benkovic and T.J. Huang, On-chip manipulation of single microparticles, cells, and organisms using surface acoustic waves. *Proc. Natl. Acad. Sci. U. S. A.*, **2012**. 109(28), 11105-11109.
80. Augustsson, P., C. Magnusson, M. Nordin, H. Lilja and T. Laurell, Microfluidic, Label-Free Enrichment of Prostate Cancer Cells in Blood Based on Acoustophoresis. *Anal. Chem.*, **2012**. 84(18), 7954-7962.
81. Lee, K., H. Shao, R. Weissleder and H. Lee, Acoustic Purification of Extracellular Microvesicles. *ACS Nano*, **2015**. 9(3), 2321-2327.
82. Maragò, O.M., P.H. Jones, P.G. Gucciardi, G. Volpe and A.C. Ferrari, Optical trapping and manipulation of nanostructures. *Nat. Nanotechnol.*, **2013**. 8, 807.
83. Lim, J.W., D. Ha, J. Lee, S.K. Lee and T. Kim, Review of Micro/Nanotechnologies for Microbial Biosensors. *Front. Bioeng. Biotechnol.*, **2015**. 3(61).
84. He, Y., M. Tsutsui, R.H. Scheicher, F. Bai, M. Taniguchi and T. Kawai, Thermophoretic Manipulation of DNA Translocation through Nanopores. *ACS Nano*, **2013**. 7(1), 538-546.
85. Zhao, Y., C. Zhao, J. He, Y. Zhou and C. Yang, Collective effects on thermophoresis of colloids: a microfluidic study within the framework of DLVO theory. *Soft Matter*, **2013**. 9(32), 7726-7734.
86. Kar, A., T.-Y. Chiang, I. Ortiz Rivera, A. Sen and D. Velegol, Enhanced Transport into and out of Dead-End Pores. *ACS Nano*, **2015**. 9(1), 746-753.
87. Shin, S., E. Um, B. Sabass, J.T. Ault, M. Rahimi, P.B. Warren and H.A. Stone, Size-dependent control of colloid transport via solute gradients in dead-end channels. *Proc. Natl. Acad. Sci. U. S. A.*, **2016**. 113(2), 257-261.
88. Abécassis, B., C. Cottin-Bizonne, C. Ybert, A. Ajdari and L. Bocquet, Boosting migration of large particles by solute contrasts. *Nat. Mater.*, **2008**. 7, 785.
89. Friedrich, S.M., J.M. Burke, K.J. Liu, C.F. Ivory and T.-H. Wang, Molecular rheotaxis directs DNA migration and concentration against a pressure-driven flow. *Nat. Commun.*, **2017**. 8(1), 1213.
90. Shin, S., J.T. Ault, P.B. Warren and H.A. Stone, Accumulation of Colloidal Particles in Flow Junctions Induced by Fluid Flow and Diffusiophoresis. *Phys. Rev. X*, **2017**. 7(4), 041038.
91. Lee, H., J. Kim, J. Yang, S.W. Seo and S.J. Kim, Diffusiophoretic exclusion of colloidal

particles for continuous water purification. *Lab Chip*, **2018**. 18(12), 1713-1724.

92. Hong, J., B. Kim and H. Shin, Mixed-scale poly(methyl methacrylate) channel network-based single-particle manipulation via diffusiophoresis. *Nanoscale*, **2018**. 10(30), 14421-14431.
93. Keh, H.J., Diffusiophoresis of charged particles and diffusioosmosis of electrolyte solutions. *Current Opinion in Colloid & Interface Science*, **2016**. 24, 13-22.
94. Prieve, D.C., J.L. Anderson, J.P. Ebel and M.E. Lowell, Motion of a particle generated by chemical gradients. Part 2. Electrolytes. *J. Fluid Mech.*, **1984**. 148, 247-269.
95. Velegol, D., A. Garg, R. Guha, A. Kar and M. Kumar, Origins of concentration gradients for diffusiophoresis. *Soft Matter*, **2016**. 12(21), 4686-4703.
96. Paustian, J.S., C.D. Angulo, R. Nery-Azevedo, N. Shi, A.I. Abdel-Fattah and T.M. Squires, Direct Measurements of Colloidal Solvophoresis under Imposed Solvent and Solute Gradients. *Langmuir*, **2015**. 31(15), 4402-4410.
97. Shin, S., O. Shardt, P.B. Warren and H.A. Stone, Membraneless water filtration using CO2. *Nat. Commun.*, **2017**. 8, 15181.
98. Peng, R. and D. Li, Fabrication of polydimethylsiloxane (PDMS) nanofluidic chips with controllable channel size and spacing. *Lab Chip*, **2016**. 16(19), 3767-3776.
99. Smith, A.M., P. Maroni, G. Trefalt and M. Borkovec, Unexpectedly Large Decay Lengths of Double-Layer Forces in Solutions of Symmetric, Multivalent Electrolytes. *J. Phys. Chem. B*, **2019**. 123(7), 1733-1740.
100. Shin, S., J.T. Ault, J. Feng, P.B. Warren and H.A. Stone, Low-Cost Zeta Potentiometry Using Solute Gradients. *Adv. Mater.*, **2017**. 29(30), 1701516-n/a.
101. Ridaoui, H., A. Jada, L. Vidal and J.B. Donnet, Effect of cationic surfactant and block copolymer on carbon black particle surface charge and size. *Colloids Surf. Physicochem. Eng. Aspects*, **2006**. 278(1), 149-159.
102. Sis, H. and M. Birinci, Effect of nonionic and ionic surfactants on zeta potential and dispersion properties of carbon black powders. *Colloids Surf. Physicochem. Eng. Aspects*, **2009**. 341(1), 60-67.
103. Zeng, Y. and D.J. Harrison, Self-Assembled Colloidal Arrays as Three-Dimensional Nanofluidic Sieves for Separation of Biomolecules on Microchips. *Anal. Chem.*, **2007**. 79(6), 2289-2295.
104. Ohshima, H., Henry's Function for Electrophoresis of a Cylindrical Colloidal Particle. *J. Colloid Interface Sci.*, **1996**. 180(1), 299-301.
105. Gregory, J., Particles in Water: Properties and Processes. *IWA Pub Taylor & Francis Group: London*, **2005**, 63-92.
106. Zhang, Q., J. Kang, Z. Xie, X. Diao, Z. Liu and J. Zhai, Highly Efficient Gating of Electrically Actuated Nanochannels for Pulsatile Drug Delivery Stemming from a Reversible Wettability Switch. *Adv. Mater.*, **2018**. 30(4), 1703323.
107. Vlassiouk, I., T.R. Kozel and Z.S. Siwy, Biosensing with Nanofluidic Diodes. *J. Am. Chem. Soc.*, **2009**. 131(23), 8211-8220.
108. Fan, R., R. Karnik, M. Yue, D. Li, A. Majumdar and P. Yang, DNA Translocation in Inorganic Nanotubes. *Nano Lett.*, **2005**. 5(9), 1633-1637.
109. Peng, R. and D. Li, Detection and sizing of nanoparticles and DNA on PDMS nanofluidic chips based on differential resistive pulse sensing. *Nanoscale*, **2017**. 9(18), 5964-5974.
110. Siria, A., P. Poncharal, A.-L. Biance, R. Fulcrand, X. Blase, S.T. Purcell and L. Bocquet, Giant osmotic energy conversion measured in a single transmembrane boron nitride nanotube. *Nature*, **2013**. 494, 455.
111. Lin, C.-Y., C. Combs, Y.-S. Su, L.-H. Yeh and Z.S. Siwy, Rectification of Concentration

Polarization in Mesopores Leads To High Conductance Ionic Diodes and High Performance Osmotic Power. *J. Am. Chem. Soc.*, **2019**. 141(8), 3691-3698.

112. Brogioli, D., Extracting Renewable Energy from a Salinity Difference Using a Capacitor. *Phys. Rev. Lett.*, **2009**. 103(5), 058501.
113. Kim, S.J., S.H. Ko, K.H. Kang and J. Han, Direct seawater desalination by ion concentration polarization. *Nat. Nanotechnol.*, **2010**. 5, 297.
114. Powell, M.R., L. Cleary, M. Davenport, K.J. Shea and Z.S. Siwy, Electric-field-induced wetting and dewetting in single hydrophobic nanopores. *Nat. Nanotechnol.*, **2011**. 6, 798.
115. Lee, J., T. Laoui and R. Karnik, Nanofluidic transport governed by the liquid/vapour interface. *Nat. Nanotechnol.*, **2014**. 9(4), 317-323.
116. Smirnov, S.N., I.V. Vlassiouk and N.V. Lavrik, Voltage-Gated Hydrophobic Nanopores. *ACS Nano*, **2011**. 5(9), 7453-7461.
117. Lum, K., D. Chandler and J.D. Weeks, Hydrophobicity at Small and Large Length Scales. *J. Phys. Chem. B*, **1999**. 103(22), 4570-4577.
118. Smirnov, S., I. Vlassiouk, P. Takmakov and F. Rios, Water Confinement in Hydrophobic Nanopores. Pressure-Induced Wetting and Drying. *ACS Nano*, **2010**. 4(9), 5069-5075.
119. Xiao, K., Y. Zhou, X.-Y. Kong, G. Xie, P. Li, Z. Zhang, L. Wen and L. Jiang, Electrostatic-Charge- and Electric-Field-Induced Smart Gating for Water Transportation. *ACS Nano*, **2016**. 10(10), 9703-9709.
120. Yameen, B., M. Ali, R. Neumann, W. Ensinger, W. Knoll and O. Azzaroni, Single Conical Nanopores Displaying pH-Tunable Rectifying Characteristics. Manipulating Ionic Transport With Zwitterionic Polymer Brushes. *J. Am. Chem. Soc.*, **2009**. 131(6), 2070-2071.
121. Vlassiouk, I., C.-D. Park, S.A. Vail, D. Gust and S. Smirnov, Control of Nanopore Wetting by a Photochromic Spiropyran: A Light-Controlled Valve and Electrical Switch. *Nano Lett.*, **2006**. 6(5), 1013-1017.
122. Zhu, J., K. Hippalgaonkar, S. Shen, K. Wang, Y. Abate, S. Lee, J. Wu, X. Yin, A. Majumdar and X. Zhang, Temperature-Gated Thermal Rectifier for Active Heat Flow Control. *Nano Lett.*, **2014**. 14(8), 4867-4872.
123. Wang, D., S. Zheng, H. Liu, J. Tang, W. Miao, H. Wang, Y. Tian, H. Yang and L. Jiang, A Magnetic Gated Nanofluidic Based on the Integration of a Superhydrophilic Nanochannels and a Reconfigurable Ferrofluid. *Adv. Mater.*, **2019**. 31(7), 1805953.
124. Hou, X., Y. Hu, A. Grinthal, M. Khan and J. Aizenberg, Liquid-based gating mechanism with tunable multiphase selectivity and antifouling behaviour. *Nature*, **2015**. 519, 70.
125. Hou, X., J. Li, A.B. Tesler, Y. Yao, M. Wang, L. Min, Z. Sheng and J. Aizenberg, Dynamic air/liquid pockets for guiding microscale flow. *Nat. Commun.*, **2018**. 9(1), 733.
126. Randall, G.C. and P.S. Doyle, Permeation-driven flow in poly(dimethylsiloxane) microfluidic devices. *Proc. Natl. Acad. Sci. U.S.A.*, **2005**. 102(31), 10813-10818.

Acknowledgements

I would like to thank my advisor, Prof. Taesung Kim, first for his endless encouragements and valuable supports he provided during my graduate study. Whenever I failed in my study, he continued to wake me up and create a professional mindset for me to solve the problem as an engineer. Without his passion and efforts, I would not have been able to achieve this growth in not only capability but also philosophy for my future life. I would also like to express my gratitude to all committee members (Prof. Heungjoo Shin, Prof. Hoon Eui Jeong, Prof. Jungyul Park, Prof. Jungchul Lee) for their sharp and delicate advices on this dissertation. Their broad insight and valuable comments make me more professional. I also appreciate to faculty members (Prof. Taesung Kim, Prof. Heungjoo Shin, Prof. Hyungson Ki, Prof. Jaesung Jang, and Prof. Jaeseon Lee, Prof. Hoon Eui Jeong) who taught me with systematic and informative lectures in the Department of Mechanical Engineering at UNIST.

I would like to extend my gratitude to my former and current μFNM laboratory members who have been together on this journey for seven years. I received a lot of help from seniors. Prof. Minseok Kim taught me basic technique to design the solution and conduct experiment. He also showed me how a student can become a professional researcher. Ji Won Lim helped me to conduct unfamiliar experiment including microorganism and extend my knowledge in microbiological fields. Yoonkwang Nam and Mingjie Jia encouraged me when I failed as a freshman. Hyunmoon Nam helped me a lot in my additional research project (Global Ph. D. fellowship). Dong-joo Kim, Qitao Zhou, Ashish Kumar Thokchom, who had joined the μFNM laboratory as postdoc were happy to share their knowledge. Jongwan Lee who has took the longest time with me helped me in many ways dealing with research, paper, and people. I would also like to thank juniors for their generous and dedicated efforts. Jungyu Park helped me a lot without hesitation. Kyunghun Lee was always nice to me and he never hesitated to accept my request for discussion of numerical analysis about my works. Juyeol Bae helped me to remind various idea of my works. I would like to express special thanks to Sangjin Seo. He complemented my weakness to deal with complexed study in terms of mathematical and theoretical parts of multidisciplinary phenomena. I really appreciate his supports again. Janghyun Ju, Youngchul Chae, Yeonghoon Jeong were also very nice to me. And there are several names in other laboratories: Youngjin Lim, Seongkyeol Hong, Jaehoon Kim, Yoonjung Lee, Jisoo Hong, Jisoo Kim, Hangil Ko, Jongmin Lee, Hoon Yi, Changho Han, Hyun-Ha Park, Minho Seong, Beomsang Kim. Thanks all.

Lastly, I would like to thank my family. My parents and brother, Chunkeun Ha, Gyeongsuk Nam, and Hyunsu Ha have supported me for a long time and gave me constant power to continue this challenge. Finally, I would like to thank my love, Eunjin Cho. She comforted me mentally and showed infinite faith whenever I was depressed. She has been my greatest inspiration to continuously move my career. Love you and thank you.

Dogyeong Ha, Ph. D.

Department of Mechanical Engineering
Ulsan National Institute of Science and Technology (UNIST)
50, UNIST-gil, Ulsan, South Korea
E-mail: hys6038@naver.com or dogyeong@unist.ac.kr
Phone: +82-10-6368-9529

Education

- **Combined M.S. & Ph. D.,** Mechanical Engineering (Mar. 2013 – Feb. 2019)
  - Ulsan National Institute of Science and Technology (UNIST)
  - **Thesis:** Nanochannel-Assisted Active Control of Mass Transport in Polydimethylsiloxane-Based Micro-/Nanofluidic Systems
  - **Advisor:** Taesung Kim

- **B.S.,** Mechanical and Advanced Materials Engineering (Mar. 2009 – Feb. 2013)
  - Ulsan National Institute of Science and Technology (UNIST)
  - **Advisor**: Taesung Kim

Research Experience

- Project #1: Crack-Photolithography for Nanopatterning on Micropatterned Photoresists (National Research Foundation of Korea, 2014.11 – Present)
  - Development of a cracking-assisted photolithography for fabrication of nanopatterns.
  - Development of an improved soft lithography for production of collapse-free nanochannel.
  - Production of solute gradient using crack-assisted nanochannel for nanoparticle separation.

- Project #2: BRL for Modeling and Control of Neuronal Signal Transmission based on Rapid and Precise Cooling Technology
  (National Research Foundation of Korea, 2017.06 – Present)
  - Analysis of electrical characteristics of aqueous solution in nanochannel.
  - Demonstration of voltage drop by change of ion distribution in nanochannel.
  - Diffusiophoresis-based control of colloidal particles.

- Project #3: Controlling Self-assembly of Photonic Crystal Nanobeads for Colorimetric Applications
  (National Research Foundation of Korea, 2013.03 – 2018.02)
  - Production of structural color using inkjet printing.

  - Control of surface tension of droplet for production of monolayer structure.
  - Development of anti-counterfeit application using the visible light.

- Project #4: Designing Fermentation Processes for the Biofuel Production using Synthetic Microbes
  (National Research Foundation of Korea, 2012.09 – 2015.09)
  - Fabrication of microenvironment system for high-throughput screening.
  - Genetic induction assay (e.g., cell-to-cell communication)

Honors and Awards

- Scholarship
  - Global Ph.D. Fellowship (GPF), (2013-2017)
  - BK21 PLUS, (2013-2018)
  - The National Scholarship for Science and Engineering, (2009-2012)

- Awards
  - Best Paper Award : KSME spring 2107 Micro-Nano Eng. Div., KOREA (2017)
  - Travel Grant : Transducers 2015 in Alaska, USA (2015)
  - Best Paper Award : BAMN 2013 in Jeju Island, KOREA (2013)

Publications

1. **D. Ha**, S. Seo, K. Lee, and T. Kim*, “Dynamic transport control of colloidal particles by repeatable active switching of solute gradients” ***ACS Nano***, 13, 12939-12948, 2019
2. Q. Zhou, J. Park, R. Nie, A. Thockchom, **D. Ha**, J. Pan, S. Seok*, and T. Kim*, “Nanochannel-assisted perovskite nanowires: from growth mechanisms to photodetector applications” ***ACS Nano***, 12, 8406-8414, 2018
3. D.-J. Kim, **D. Ha**, Q. Zhou, A. K. Thokchom, J. W. Lim, J. Lee, J. G. Park and T. Kim*, "A cracking-assisted micro-/nanofluidic fabrication platform for silver nanobelt arrays and nanosensors." ***Nanoscale***, 9, 9622-9630, 2017
4. Ashish. K. T., Q. Zhou, D.-J. Kim, **D. Ha** and T. Kim*, "Characterizing self-assembly and deposition behavior of nanoparticles in inkjet-printed evaporating droplets." ***Sens. Actuator B-Chem.***, 190, 86-92, 2017
5. M. Kim, D.-J. Kim, **D. Ha** and T. Kim*, "Cracking-assisted fabrication of nanoscale patterns for micro/nanotechnological applications." ***Nanoscale***, 9, 9622-9630, 2017
6. H. Nam, K. Song, **D. Ha** and T. Kim*, "Inkjet printing based mono-layered photonic crystal patterning for anti-counterfeiting structural colors." ***Sci. Rep.***, 6, 30885, 2016
7. **D. Ha**†, J. Hong†, H. Shin* and T. Kim*, "Unconventional micro-/nanofabrication

technologies for hybrid-scale lab-on-a-chip." ***Lab Chip***, 16, 4296-4312, 2016

8. J. W. Lim, **D. Ha**, J. Lee, S. K. Lee and T. Kim[*], "Review of micro/nanotechnologies for microbial biosensors." ***Front. Bioeng. Biotechnol.***, 3, 2015
9. M. Kim, **D. Ha** and T. Kim[*], "Cracking-assisted photolithography for mixed-scale patterning and nanofluidic applications." ***Nat. Commun.***, 6, 6247, 2015
10. W. S. Choi, **D. Ha**, S. Park and T. Kim[*], "Synthetic multicellular cell-to-cell communication in inkjet printed bacterial cell systems." ***Biomaterials***, 32, 2500-2507, 2011

Patents

1. Nanoparticles generating device and generating method using the same
   Registration #: KR 10-1526675 (date: 2015. 06. 01)
2. Metal nano wire Apparatus for manufacturing the metal nano-wire and method for manufacturing the same
   Registration #: KR 10-1944948 (date: 2019. 01. 28)
3. Method of performing self-powered diffusiophoresis using the same
   Application #: KR 10-2019-0007611 (date: 2019. 01. 21)
4. Self-powered diffusiophoresis apparatus and method of performing self-powered diffusiophoresis using the same
   Application #: KR 10-2019-0007610 (date: 2019. 01. 21)
5. Apparatus for separating nanoparticles and methods for separating nanoparticles using the apparatus
   Application #: KR 10-2019-0132354 (date: 2019. 10. 23)
6. Apparatus for controlling the transport of materials in nanochannels by controlling humidity
   Application #: KR 10-2019-0142347 (date: 2019. 11. 08)
7. Method for extracting fine object using diffusiophoresis and identification method of the fine object using the method
   Application #: KR 10-2019-0148551 (date: 2019. 11. 19)

Conference Proceedings

1. J. Lee, K. Lee, C. Wang, **D. Ha**, J. Park, and T. Kim, “Thermal and Electrokinetic Effect on Diffusioosmosis-Driven Ionic Transport through Nanopores” **MicroTAS 2019** (Poster)
2. K. Lee, J. Lee, **D. Ha**, M. Kim, and T. Kim, “Combinational Diffusiophoretic and Electrophoretic Nanoparticle Separation”, **MicroTAS 2019** (Poster)
3. S. Seo, **D. Ha**, and T. Kim, “A Repulsive Point-Source Diffusiophoresis Device for Nanoparticle Separation”, **MicroTAS 2019** (Poster)
4. **D. Ha**, S. Seo, and T. Kim, “Micro-/Nanofluidic Diffusiophoresis Platform for Simple

Concentration and Extraction of Particles using Ionic Solutions", **IEEE MEMS 2019** (Oral)

5. **D. Ha**, S. Seo, and T. Kim, "Rapid and Dynamic Switching of Physicochemical Environments for Diffusiophoretic Particle Manipulation and Separation", **MicroTAS 2018** (Oral)
6. **D. Ha**, D.-J. Kim, Q. Zhou, and T. Kim, "Silver Nanowire Syntehsis through Nanofluidic Network using a Crack-photolithography for Bio/chemical Sensor Applications", **MicroTAS 2017** (Poster)
7. **D. Ha**, D.-J. Kim, J. Park, and T. Kim, "Crack-photolithography-assisted Collapse-free and Mass-transport-controllable Nanochannel Microfabrication", **MicroTAS 2017** (Poster)
8. A. K. Thokchom, J. Park, Q. Zhou, **D. Ha**, J. Park, K. Lee, and T. Kim, "Permanent Encapsulation of Nanoparticle Patterns formed by Inkjet Printer for Transparent and Flexible Anti-Counterfiet Applications", **Transducers 2017** (Poster)
9. H. Nam, **D. Ha**, K. Song, and T. Kim, "Inkjet-printing-based Structural Coloring for Anti-Counterfeit Applications", **Transducers 2015** (Poster)
10. M. Kim, **D. Ha**, and T. Kim, "Crack-photolithography for High-throughput Nanopatterning and Nanofluidic Applications", **Transducers 2015** (Poster)
11. **D. Ha**, J. W. Lim, and T. Kim, "Live-Cell Printing for Screening of Engineered Bacterial Strains", **Biofabrication 2014** (Poster)
12. J. Lee, **D. Ha**, M. Kim, and T. Kim, "Temporally Programmable Cell Culture Environment using a Membrane Integrated Microbioreactor", **MicroTAS 2014** (Poster)
13. S. Seo, **D. Ha**, and T. Kim, "Diffusiophoresis-Based Particle Transport Control in Micro-/Nanofluidic Channel", **KSV-Fall 2018** (Oral)
14. **D. Ha**, J. Park, and T. Kim, "Visualization of Mass Transport in Crack-photolithography-assisted Nanochannels Manipulated by Surrounding Humidity" **KSV-Fall 2017** (Oral)
15. A. K. Thokchom, Q. Zhou, J. Park, **D. Ha**, and T. Kim, "Visualization of Microfluid Flow in Evaporating Droplets for Self-Assembly Control of Nanoparticles", **KSV-Fall 2017** (Oral)
16. A. K. Thokchom, Q. Zhou, **D. Ha**, J. Park, K. Lee, J. Park, and T. Kim, "Cover and overt transformation of structural colors formed by inkjet printing of nanoparticle suspension for durable and flexible anti-counterfeit applications", **KSME-Micro/Nano div. 2017** (Poster)
17. D.-J. Kim, **D. Ha**, and T. Kim, "Crack-photolithography-assisted Nanofluidic Synthesis of Silver Nanowire Arrays", **KSME-Micro/Nano div. 2017** (Oral)
18. **D. Ha**, and T. Kim, "Microfabrication of Crack-photolithography-assisted Collapse-free and Mass-transport-controllable Nanochannels for Bio-applications" **KSME-Bio div. 2017** (Oral)
19. **D. Ha**, M. Kim, and T. Kim, "Crack-assisted Integrated Microfluidic Chip for Diffusion-controlled and High-throughput Cellular Induction Assays" **KMEMS 2017** (Poster)
20. **D. Ha**, M. Kim, and T. Kim, "Crack-photolithography based Quantitative High-throughput Cellular Assays on a Chip", **KSME-Bio div. 2016** (Poster)
21. D.-J. Kim, **D. Ha**, and T. Kim, "Fabrication of Metallic Nanowires based Device for Biosensor Applications by using Crack-Photolithography", **KSME-Bio div. 2016** (Poster)
22. D.-J. Kim, **D. Ha**, and T. Kim, "Geometrical Evaluation of Crack-lithography assisted Nanopatterns on SU-8 Film by Annealing Conditions", **KMEMS 2016** (Poster)

23. **D. Ha**, D.-J. Kim, and T. Kim, "Crack-photolithography based Nanochannel Arrays for High-throughput Bacterial Chemotaxis Assays", **KMEMS 2016** (Poster)
24. **D. Ha**, J. W. Lim, and T. Kim, "Large-area Live-cell Printing at the Single Cell Level for High Throughput Screening", **KSME-Fall 2014** (Poster)
25. J. Park, **D. Ha**, M. Kim, and T. Kim, "Microfluidic Platform with Hydrogel-Encapsulated Bioreactor Array for Long Shelf-life Microbial Biosensors", **KSME-Fall 2014** (Poster)
26. H. Nam, **D. Ha**, H. Lee, J. Lee, W. Park, Y. Kim, and T. Kim, “Inkjet Printing of Photonic Crystal Nanobeads for Structure Colors”, **BAMN 2013** (Poster)
27. W. Choi, **D. Ha**, S. Park, and T. Kim, "Inkjet Printing of Bacterial Cells for Synthetic Multicellular Cell-to-Cell Communication Study" **MMB 2011** (Poster)